Numerical Study of the Flow Around an Undersized Ball Pig in a Horizontal Pipe

M. JIANG

October, 2018

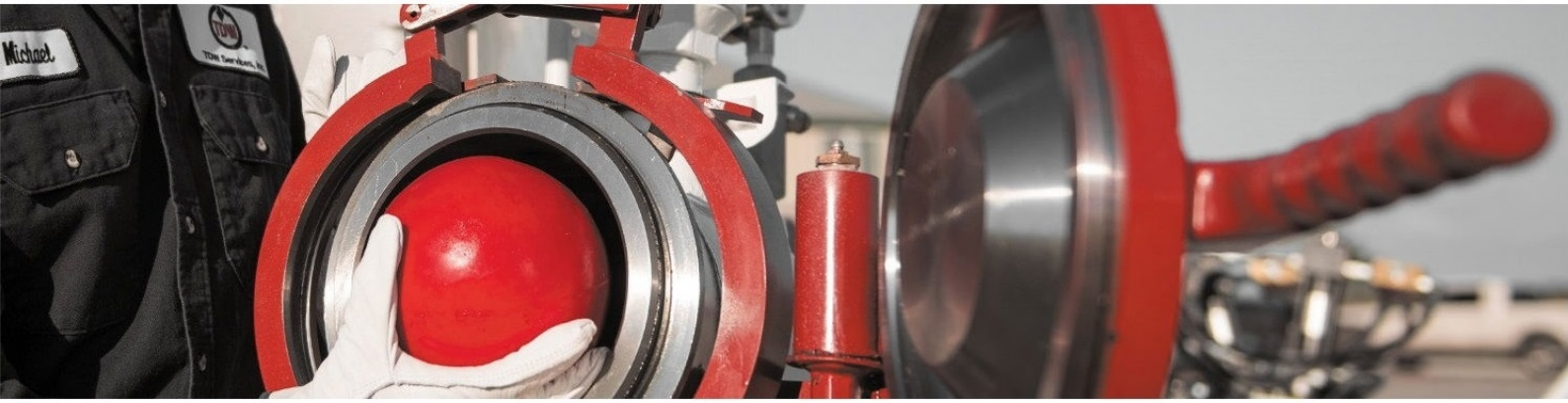

TU Delft Delft University of Technology

Challenge the future

Numerical Study of the Flow Around an Undersized Ball Pig in a Horizontal Pipe

by

M. JIANG
October, 2018

As part of the fulfillment of the requirements for the degree of master of

Mechanical Engineering
Track: Process and Energy Technology

at the Delft University of Technology

Student number: 4632745
Supervisor: Prof. dr. ir. R.A.W.M. Henkes

P&E report number: 2927

TU Delft Delft University of Technology

Preface

My graduation project has come to the final stage and I would have never able to reach this point without the help from others.

I would like to take this chance to thank my supervisor Professor Ruud Henkes for providing me with this research project, for his patient and encouraging supervision and for his valuable advices on and help with my project. It was very pleasant to work with him. I appreciate all the encouragement I received from him during the last nine months.

I would like to thank Dr. Mathieu Pourquie for his kind help with all the numerical problems I have encountered during this research. I cannot imagine how much more time I could have spent on struggling with those numerical issues without his help.

I would also like to thank Dr. Wim-Paul Breugem for the time he took for discussions with me on my project.

Also, I would like to thank Dr. Alexander van Zuijlen for agreeing to be a member in my graduation committee and for taking the time to read my thesis.

Moreover, I would like to thank my peer classmates who spent their time patiently discussing with me whenever I got stuck in my project.

Last but not least, I would love to thank my parents, my beloved Long, my sister and my dear friends, for giving me unconditional love and support. They are my preciouses in my life!

M. JIANG
October, 2018

Abstract

Pipeline networks are extensively used in the oil and gas industry to transport fluids under multiphase flow conditions from the wells to the production platforms or plants. Over time, the flow rate of the production fluid decreases as the reservoir pressure decreases. When the flow rate decreases to below a certain value, unstable flow with liquid slugs occurs and the transportation of the fluids becomes more difficult. This is because of the high amount of liquid accumulation (holdup) in the pipeline.To extend the operation life of the production system, it is important to maintain the continuous production at low flow rates. Regular pigging, which refers to transporting a "pig" (Pipeline Inspection Gauge) through the pipeline, has been a conventional way of managing the liquid holdup in the oil and gas industry. Also "by-pass" pigs have been actively used to manage the liquid holdup since they generate smaller slug volumes compared to the traditional non-bypass pigs. However, since the pipeline can be as long as a hundred (or more) kilometers, the volume of the pig-generated slug at low flow rates can be very large. Even this reduced slug volume produced by using a by-pass pig may exceed the capacity of the downstream separator or slug catcher. Moreover, by-pass pigs with a large by-pass area have a high chance to get stuck in the pipeline at low flow rates. To enable pigging operation at those conditions, the use of an undersized ball pig was proposed. Here the ball pig is transversed through the pipeline prior to the by-pass pigging operation. A few test runs with undersized ball pigs were carried out in the F14 multiphase pipeline in Sarawak. To improve its performance, it is of much interest to study the detailed flow around an undersized ball pig. Although in actual operation the ball pig will be used under multiphase conditions (i.e. gas and liquid flow), in this study, as a starting point, single-phase flow was considered.

This study investigated the detailed flow around an undersized ball pig in a horizontal pipe with the help of Ansys Fluent version 18.2. First, benchmark data from experiments are used to find the best numerical model which can be used to simulate the flow around a sphere. The comparison between experimental data and numerical results shows that the 2D laminar simulation can accurately capture the flow when Re < 300. The 2D simulation with the SST $k-\omega$ turbulence model (low-Reynolds number correction) gives an accurate prediction of the drag coefficient when 300 < Re < 5E5.

The selected numerical models are then used to study the flow around an undersized ball pig in a pipe. For each set of conditions, this requires to carry out a number of simulations at different ball pig velocities, and find the velocity that gives zero drag force on the ball pig. The undersized ball pig is first moved to the centre, and 2D simulations were performed. The force analysis around the undersized ball pig at low Reynolds number shows that at equilibrium state, the undersized ball pig experiences a positive pressure force and a negative viscous shear force. Moreover, the computed profile of the normalized terminal velocity of the pig with a diameter ratio of 0.5 at various Reynolds numbers shows that the normalized terminal pig velocity profile experiences three stages when the Reynolds number is increased. In the first stage where Re < 365, the motion of the pig is dominated by the viscous shear force and the normalized terminal velocity of the pig is constant. When Re increases, the flow enters the second stage where the inertia force starts to affect the motion of the pig and the normalized terminal velocity of the pig decreases dramatically. When Re is further increased to above 5340, the motion of the pig is completely affected by the inertia force and the normalized terminal velocity of the pig stays in a stable range when Re increases. After this detailed study of the flow around an undersized ball pig with a fixed diameter ratio, simulations of the flow around undersized ball pigs with various diameter ratios are studied to find the influence of the pig diameter on the terminal velocity of the pig. The results show that the obtained profiles of the normalized pig terminal velocity against Re at various diameter ratios have a similar shape as when the diameter ratio was 0.5; the terminal pig velocity decreases when the pig diameter increases at a given Re. A further data regression analysis shows that the normalized pig terminal velocity in the region when Re < 300 and Re > 10000 has a second-order polynomial relationship with the diameter ratio.

After the simulations for the flow around an undersized ball pig that moves along the axis of the pipe, the pig is moved to the bottom of the pipe and the influence of this position change is studied at a diameter ratio of 0.9. Due to this position change, a 3D simulation is required. First a 3D simulation for the previous configuration with the pig at the centre is performed. This simulation shows that the flow is actually unsteady and asymmetric. The terminal pig velocity at a given Reynolds number obtained from the 3D simulation is slightly higher than the one obtained from the 2D simulation. As the 2D simulation cannot capture the asymmetry of the flow, it provides less accurate results. The 3D simulation results of the flow past an undersized ball pig moving along the axis of the pipe is then compared with the one moving along the bottom of the pipe. The comparison shows that the ball pig velocity is decreased when the pig is moved from the centre to the bottom of the pipe.

Contents

List of Symbols

Greek notations:

Symbol	Description	Unit
α	Volume fraction	[-]
ϵ	Turbulence dissipation rate	$[\mathrm{m}^2 \cdot s^{-3}]$
μ	Dynamic viscosity of the fluid	$[kg \cdot m^{-1} \cdot s^{-1}]$
μ_t	Turbulent viscosity	$[m^2 \cdot s^{-1}]$
ρ	Density of the fluid	$[kg \cdot m^{-3}]$
τ_{ij}	Reynolds stress	$[kg \cdot m^{-1} \cdot s^{-2}]$
τ_w	Wall shear stress	$[kg \cdot m^{-1} \cdot s^{-2}]$
ω	Specific turbulence dissipation rate	$[s^{-1}]$

English notations:

Symbol	Description	Unit
A	Projected frontal area of the pig	$[m^2]$
b	The height between two parallel plates	$[m]$
C_d	Overall drag coefficient	[-]
C_f	Viscous shear drag coefficient	[-]
C_p	Pressure drag coefficient	[-]
D	Pipe diameter	$[m]$
d	Pig diameter	$[m]$
F_d	Drag force	$[kg \cdot m \cdot s^{-2}]$
F_f	Viscous shear force	$[kg \cdot m \cdot s^{-2}]$
F_{fric}	Fiction force between the pig and the pipe wall	$[kg \cdot m \cdot s^{-2}]$
g_i	Gravitational acceleration	$[m \cdot s^{-2}]$
F_p	Pressure force	$[kg \cdot m \cdot s^{-2}]$
H	Height of the liquid phase in the pipe	$[m]$
I	Turbulent intensity	[-]
k	Turbulent kinetic energy	$[m^2 \cdot s^{-2}]$
Lh	Entrance length	$[m]$
m	Mass of the pig	$[kg]$
p	Pressure	$[kg \cdot m^{-1} \cdot s^{-2}]$
Q_{fl}	Volumetric flow rate	$[m^3 \cdot s^{-1}]$
S_{pig}	Surface area of the pig	$[m^2]$
T	Surface force exerted on the pig	$[kg \cdot m^{-1} \cdot s^{-2}]$
t	Time	$[s]$
U	Bulk fluid velocity in the pipe	$[m \cdot s^{-1}]$
u	Fluid velocity	$[m \cdot s^{-1}]$
u^*	Wall friction velocity	$[m \cdot s^{-1}]$
u^+	Velocity in non-dimensional wall units	[-]
u_f	Bulk velocity of the film between the pig and pipe	$[m \cdot s^{-1}]$
u_{gas}	Bulk velocity of the gas phase	$[m \cdot s^{-1}]$
u_{liquid}	Bulk velocity of the liquid phase	$[m \cdot s^{-1}]$
V	Velocity of the moving plate	$[m \cdot s^{-1}]$
V_{pig}	Terminal velocity of the pig	$[m \cdot s^{-1}]$
V'_{pig}	Velocity of the pig	$[m \cdot s^{-1}]$
x	Distance in the x direction	$[m]$
y^+	Dimensionless distance from the wall	[-]

1 Introduction

1.1. Pigging Applications

In the oil and gas industry, extensive pipeline networks are used to transport fluids from the wells to production plants. Depending on the location of the wells and production plants, those pipelines can span a distance as long as a hundred kilometers, or more. Some of these pipelines are used to transport single-phase flow (gas or oil only), while others operate under multiphase flow conditions (gas with condensate or water). During the transportation of this multiphase flow, the gas phase moves with a relatively high velocity driven by the pressure drop and the liquid phase is transported by the drag of the gas phase with a velocity lower than the gas phase. At low gas flow rate, the gas is no longer able to take the liquid upward (in case of vertical or upward inclined pipeline sections) causing an accumulation (or so-called holdup increase) of the liquid in the system. This can cause the occurrence of slug flow, which may make the passage of gas more difficult. Such conditions typically occur at turndown production rates, or at the end of the field life of the reservoir.

To extend the lifespan of existing wells and unlock more reserves, the pipeline operation at low flow rates must be well maintained. As a low gas flow rate leads to a high liquid holdup, one of the major tasks of pipeline maintenance at low flow rates is to control the liquid holdup below a certain value to guarantee continuous and stable gas production. Pigging, which refers to transporting a "pig" (Pipeline Inspection Gauge) through the pipeline to perform maintenance operations, has been a conventional way of managing the liquid holdup in the oil and gas industry. The pig controls the liquid holdup by collecting the liquid in front of it, which generates a liquid slug. As the gas plant requires an uninterrupted supply of gas, the pig-generated slug has to be temporarily stored at the end of the pipelines in a slugcatcher, which can be costly and requires a significant plot space. Compared with a conventional pig, which is fully sealed and therefore travels with a velocity that is equal to the mixture velocity of the fluid, a by-pass pig can be a more attractive alternative. This is because it has an opening (typically of up to about 15% of the cross-sectional area of the pipe) as shown in Figure 1.1, which allows part of the gas to propagate through the pig. As a result, the pig velocity will decrease and the residence time of the pig in the pipeline increases. A lower pig velocity means that the volume of the pig-generated slug, and therefore the size of slugcatcher, will be reduced. It is known [1] that the slugcatcher size can be diminished by a factor of 4 to 5 if a by-pass pig is used. A typical by-pass pig is shown in Figure 1.2.

Since the pipeline can be as long as a hundred of kilometers, the volume of the slugs at low flow rate can be very high. While by-pass pigs generate much lower slug volumes than conventional pigs, even these volumes may exceed the size of the slug catcher. Moreover, by-pass pigs normally have a high by-pass ratio to reach the optimum effect. This increases the risk that the pig gets stalled in the pipeline at low gas flow rates. To enable and stabilize pigging operations under these conditions, undersized ball pigs can be transported through the pipeline prior to the by-pass pigging operation. The successful operation in the F-14 [4] pipeline in Sarawak, which has a 20" diameter and 30 km length, has also shown that the application of an undersized ball pig is both economically and technically feasible. As

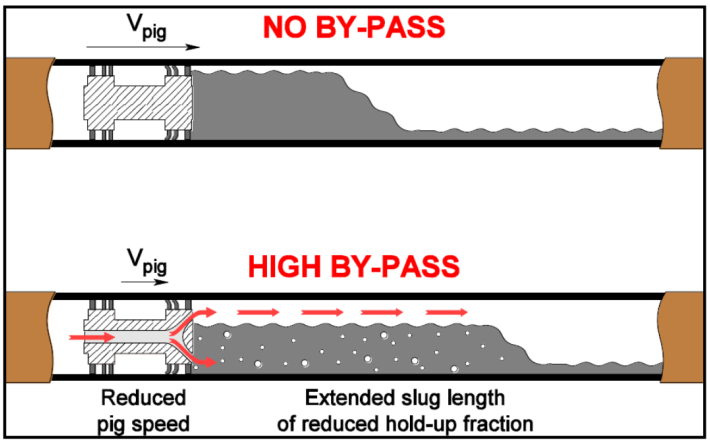

Figure 1.1: Sketch of a pig with and without a by-pass area, reproduced from [2]

Figure 1.2: Picture of a conventional by-pass pig, reproduced from [3]

there is a small space between the pipe wall and the ball pig (shown in Figure 1.3), the ball pig does not experience friction with the pipe wall. Depending on the density of the ball pig, however, the pig may touch the bottom or top of the pipe wall, which will cause some small wall friction. The absence or only a small magnitude of the wall friction makes it easier to move the ball pig along the pipeline and the pig has a smaller chance of getting stuck in the pipe. Figure 1.4 shows pictures of an undersized ball pig before and after its use in the F14 pipeline. It can be seen that except for some scratches, there is no visible damage on the undersized ball pig after its retrieval from the pipeline. This indicates that the undersized ball pig experienced only a small friction. Moreover, as the undersized ball pig gives a continuous leaking volume of liquid, it gives a smaller pig-generated slug, which reduces the required liquid surge capacity of the slug catcher.

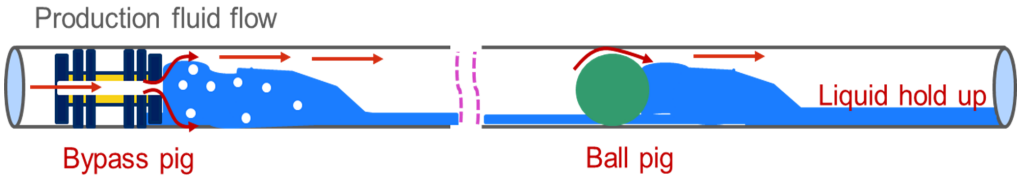

Figure 1.3: Sketch of the production fluid flow when an undersized ball pig is deployed prior to a by-pass pig

1.2. Literature Overview

Despite the technical advantage and potential economic benefit that the undersized ball pig has shown to provide in the F-14 pipeline, the detailed investigation of the flow around the undersized ball pig in a pipeline is still an area of research. Attempts have been made since 1960s to establish models which

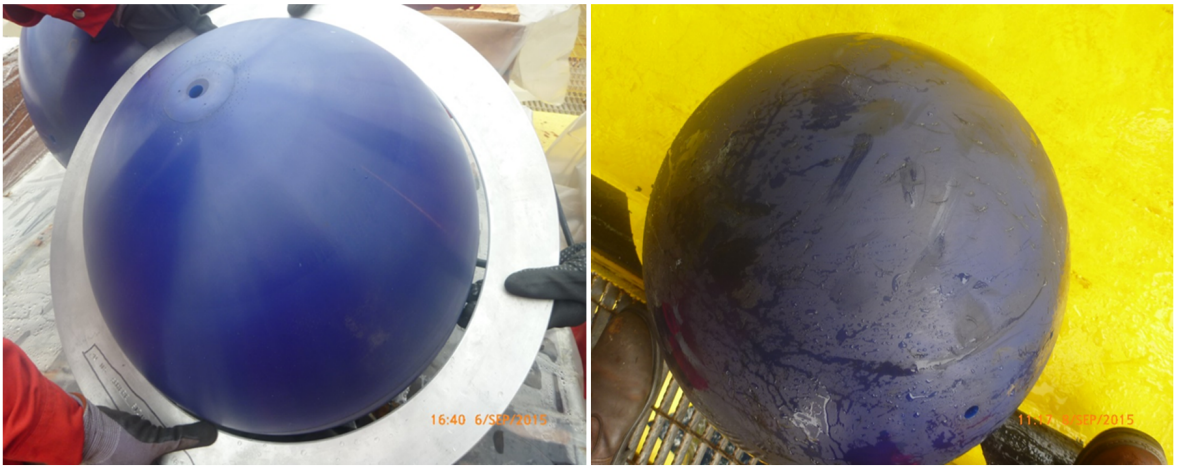

(A) (B)

Figure 1.4: Comparison of an undersized ball pig before and after used in the F14 pipeline

can be used to describe the motion of pigs both numerically [5–9] and experimentally [10, 11]. All these studies were conducted under the assumption that the pigs are fully sealed in the pipeline. As a result of this, the current models that can be used to describe the motion of pigs all contain empirical correlations for oversized pigs, i.e. pigs with a diameter that is larger than the pipe diameter. In such cases, the side of the pig is in full contact with the pipe wall, which results in a significant friction on the pig from the pipe wall. The application of such correlations for an undersized ball pig, which has no or only a small contact area with the pipe, gives a rather small wall friction.

Bhattacharjee et al. [4] developed a dynamic model to simulate the flow dynamics of the undersized ball pig in a pipeline. This dynamic model employed the OLGA transient pig model [12] to describe the wall friction force and the fluid drag force. Within the OLGA model, an empirical correlation of the pressure loss across the undersized ball is incorporated by specifying the static force between the flow and the pig. The simulation results of the dynamic model have been compared with field data for the F-14 pipeline in Sarawak. The comparison shows that this dynamic model is able to capture the liquid outflow recovery and the gas outflow rate quite well. To estimate the residence time of the undersized ball pig and the pig generated slug size, Richa [13] developed an analytical steady state 1-D model. The results of this analytical model are compared with the field data of the F-14 pipeline. This shows that the residence time is over predicted by 14% and there is a significant inaccuracy in the prediction of the slug size.

Apparently, the theory and models that can be used to describe the motion of an undersized ball pig in a pipeline are very limited and more research is therefore required to investigate this. With the motivation to look for the further optimization of the operation of undersized ball pigs, a CFD study of the flow around an undersized ball pig in a horizontal pipeline has been carried out and the results are described in this report. Ansys ICEM CFD is used for the generation of the numerical mesh and Ansys Fluent version 18.2 is used for the simulation of the flow.

1.3. Objectives

Some practical applications have shown the advantage of deploying an undersized ball pig prior to the by-pass pigging operation. But so far the research on the modelling of the flow around an undersized ball pig is very limited. This study starts from scratch and aims at achieving fundamental understanding of the detailed flow field information around the undersized ball pig with the help of CFD methods. Mainly the single-phase flow is considered.

For a numerical study, especially for the simulation of turbulent flow, it is always the first step to

find the most efficient way to simulate the flow with the required accuracy. Therefore, first simulations of the flow around a sphere in an open space will be performed to find the best numerical model for the simulation of the flow around a sphere.

For the motion of the ball pig, the force balance is essential. Therefore, the detailed force distribution around the pig needs to be obtained. The force analysis helps to obtain the terminal pig velocity and the leakage profile which are the two main parameters of interest for the industrial applications since they give an indication of the residence time of the pig and of the slug size. Therefore, the focus will be on finding these two parameters for various flow regimes.

In the oil and gas industry, one-dimensional pipeline models have been extensively used for the simulation of multiphase flows in pipelines and pigging operations. It is expected that the current numerical study will help to improve the pigging sub-models which are used to calculate the pigging operation in such 1D models.

1.4. Thesis Structure

Base on the above objectives, this thesis is organized as follows:

In Chapter 2, the theoretical background of the ball pigging problem is given. First, the governing equations of the fluid and pig are introduced. Then a dimension analysis of the problem is performed.

In Chapter 3, a model validation is performed, which is meant to test the ability of the numerical models in Ansys Fluent to accurately reproduce the single-phase flow around a sphere. Thereto the computed drag coefficient and flow field results are compared with experimental data.

In Chapter 4, the selected numerical model from Chapter 3 is applied to simulate the single-phase flow around an undersized ball pig at a given pig diameter, while the pig centre is located along the axis of the pipe. The force information around the pig is studied and the dominant factor which drives the motion of the pig is discussed for various Reynolds numbers.

In Chapter 5, the geometry of the pig is varied to study the influence of the geometry variation on the pig motion. This geometry includes the change of the pig diameter and of the location of the centre of the pig in vertical direction. Besides this, the leakage profiles at various Reynolds numbers are also obtained based on the computed terminal velocity of the pig.

In Chapter 6, the application of the results as obtained from the single-phase flow study to the simulation of multiphase flow systems will be discussed.

In Chapter 7, the conclusions of the current study are given and recommendations for further research will be provided.

2

Flow Equations

In this chapter, the relevant theoretical background information of the problem under investigation is given. First of all, a pre-analysis is conducted and based on that analysis, some simplifications and assumptions are made. Then the governing equations for both the fluid and the ball pig are described. After this, a dimension analysis is performed to figure out the dimensionless groups that affect the motion of the pig. Finally, the entrance length, which is an important parameter in the calculation, is introduced.

2.1. Problem Description

As a first approach in the CFD study of the flow around an undersized ball pig in a pipe, some simplifications and assumptions are made, due to the limitation of the available time and computational resources.

The model under investigation comprises a sphere (undersized ball pig) located at the bottom of a horizontal circular pipe. The diameter of the sphere is smaller than the pipe diameter and can be varied between zero and the pipe diameter. Although the ball pig can be deformable depending on the material and forces exerted on the ball pig, it is assumed in this research that the pig is a rigid body and impermeable, and the same assumptions are made for the pipe wall.

The flow domain is apparently 3D. However, a 3D simulation can be computationally quite expensive. To figure out the driving factors behind the pig dynamics, the pig centre is first moved to the centre of the pipe and it is initially assumed that the pig centre moves along the axis of the pipe. In such case, the simulation can be simplified to a 2D axisymmetric flow. Therefore, there is no need to consider the friction between the pig and the pipe wall in this approach. Later, based on the results obtained in the 2D simulation, the calculation will be moved to 3D to investigate the effect of the pig position in the pipe on the motion of the pig.

Given the application of the undersized ball pig, the flow is essentially stratified multiphase flow with liquid at the bottom and gas at the top of the pipe. But to figure out the detailed forces exerted on the pig, this study starts with a single-phase flow simulation. At the same time, this study will only focus on the motion in the fully developed flow regime. Therefore, only the steady state motion of the pig is simulated.

2.2. Governing Equations

In this section, the flow equations and relevant numerical models are introduced.

2.2.1. Navier-Stokes Equations

The Navier-Stokes equations are the governing equations of viscous fluid, which can be derived by applying conservation laws on the fluid flow and by implementing the constitutive equation for a New-

tonian fluid. It comprises a set of coupled non-linear partial differential equations and describes the flow-field variables of velocity and pressure. The mass and momentum conservation equation for an incompressible Newtonian fluid, using the Einstein summation convention, are:

$$\frac{\partial u_i}{\partial x_i} = 0 \tag{2.1}$$

$$\rho[\frac{\partial u}{\partial t} + \frac{\partial}{\partial x_j}(u_j u_i)] = -\frac{\partial p}{\partial x_i} + \mu\frac{\partial}{\partial x_j}(\frac{\partial u_i}{\partial x_j} + \frac{\partial u_j}{\partial x_i}) + f \tag{2.2}$$

Where:

- ρ is the density of the fluid;
- μ is the viscosity of the fluid;
- f is the body force acting on the fluid;
- u and p are the velocity and pressure variables that will be used to describe the motion of the flow.

Equations 2.1 and 2.2 contain four coupled non-linear partial differential equations for a 3D flow system, which can be simplified to three equations for 2D flow. The continuity equation (Equation 2.1) is a direct description of the mass conservation for an incompressible fluid. The momentum equation (Equation 2.2) is derived by applying momentum conservation on a flowing fluid element and thus contains terms that affect the motion of the fluid. The left hand side shows the inertia term which contains both the time dependent term and the local convective acceleration. At the right hand side of the equation, the first term is the pressure gradient and the second one shows diffusion of momentum. These two terms are derived by determining the surface force acting on a material control volume. Hence they represent the internal change of momentum in the flow system. The last term represents external forces that may affect the motion of the flow.

In fluid mechanics, the Reynolds number (Re) is a very important dimensionless number and it arises when considering the dimensionless form of the Navier-Stokes equations. It represents the ratio of the inertia force and the viscous force, so it gives an indication of the importance of various terms in the Navier-Stokes equations. The definition of Re is:

$$Re = \frac{\rho U^2/l}{\mu U/l^2} = \frac{\rho U l}{\mu} \tag{2.3}$$

where U is the reference velocity of the fluid and L is a characteristic length.

For fully developed pipe flow, Reynolds has demonstrated in his pipe experiment that there is a transition from smooth orderly laminar flow to irregular turbulent flow when $Re = \rho U d/\mu$ is between 2000 to 3000, in which U is the average velocity over the cross sectional area of the pipe and d is the pipe diameter.

Given the complexity of the Navier-Stokes equations, analytical solutions do not exist except for some very simple cases. In practical applications, the fluid flow problems are often solved numerically. In general, numerical simulation methods are classified into three categories. The most complete and accurate one is Direct Numerical Simulation (DNS) in which the Navier-Stoke equations are directly discretized and the corresponding discretized system is then solved. This implies that the numerical mesh has to represent the whole range of spatial and temporal scales of the flow in the computational flow domain. The computational mesh has to be small enough to capture the smallest dissipative scales which leads to an exponential growth of the mesh number when the Reynolds number increases. Due to this large cost, there is a need to reduce the complexity of the equations of motion, which can be done through using submodels to represent the effect of turbulence. The Large Eddy Simulation (LES) is a method that only resolves the large scales of the flow and the small scales are modelled. By filtering the small scales of the flow, this method largely decreases the computational cost compared with DNS. The

computational cost of LES, however, may still exceed what is available for most engineering problems, for which all fine details of the flow can be of less interest. To further reduce the computational cost, the Reynolds-Averaged Navier-Stokes (RANS) equations can be applied, which are indeed quite often used for solving industrial problems.

2.2.2. Reynolds-Averaged Navier-Stokes (RANS) Equations

The RANS equations are obtained by applying the so-called Reynolds decomposition to the Navier-Stokes equations. Reynolds decomposition assumes that an instantaneous quantity in turbulent flow can be decomposed into an average value plus a fluctuation. It is also assumed that the turbulent flow behaviour is statistically stationary, which implies a constant average and fluctuation value. In this way, the velocity components u_i and the pressure p can be decomposed as follows:

$$u_i = \bar{u}_i + u_i', \qquad p = \bar{p} + p' \tag{2.4}$$

By applying the above decomposition and the Reynolds conditions, the following RANS equations can be obtained:

$$\rho[\frac{\partial \overline{u_i}}{\partial t} + \overline{u_j}\frac{\partial \overline{u_i}}{\partial x_j}] = -\frac{\partial \overline{p}}{\partial x_i} + \frac{\partial}{\partial x_j}(\mu\frac{\partial \overline{u_i}}{\partial x_j} - \rho\overline{u_i'u_j'}) \tag{2.5}$$

$$\frac{\partial \overline{u_i}}{\partial x_i} = 0 \tag{2.6}$$

It can be seen from the above equations that a new term has appeared, which is called the Reynolds stress. It is defined as:

$$\tau_{ij} = -\rho\overline{u_i'u_j'} \tag{2.7}$$

The appearance of this term has closed the set of equations. In order to solve the RANS equations, various turbulence models at a different level of complexity have been developed, which range from the algebraic model (Prandtl mixing length) to the Reynolds Stress Model. In this study, the two-equation $k-\epsilon$ and $k-\omega$ turbulence models are applied since they are most widely used in the industry.

Two equation models are developed based on the Boussinesq eddy viscosity assumption, which applies the analogy between turbulence transport and the role of molecular viscosity in the momentum transfer. It can be expressed as:

$$-\rho\overline{u_i'u_j'} = \mu_t(\frac{\partial u_i}{\partial x_j} + \frac{\partial u_j}{\partial x_i}) - \frac{2}{3}(\rho k + \mu_t\frac{\partial u_k}{\partial x_k})\delta_{ij} \tag{2.8}$$

The turbulent viscosity is assumed to be a scalar quantity which is a function of two other quantities. At the same time, two more transport equations are developed for these two quantities, which are the turbulent kinetic energy k and the turbulent dissipation rate ϵ for the $k-\epsilon$ model and the turbulent kinetic energy k and the specific dissipation rate for the $k-\omega$ model. The expressions of these two models are described below.

Standard $k-\epsilon$ model

The turbulent kinetic energy k and its rate of dissipation ϵ are computed by the following transport equations:

$$\frac{\partial}{\partial t}(\rho k) + \frac{\partial}{\partial x_i}(\rho k u_i) = \frac{\partial}{\partial x_j}[(\mu + \frac{\mu_t}{\sigma_k})\frac{\partial k}{\partial x_j}] + G_k + G_b - \rho\epsilon - Y_M + S_k \tag{2.9}$$

$$\frac{\partial}{\partial t}(\rho\epsilon) + \frac{\partial}{\partial x_i}(\rho\epsilon u_i) = \frac{\partial}{\partial x_j}[(\mu + \frac{\mu_t}{\sigma_\epsilon})\frac{\partial \epsilon}{\partial x_j}] + C_{1\sigma}\frac{\sigma}{k}(G_k + C_{3\epsilon}G_b) - C_{2\epsilon}\rho\frac{\epsilon^2}{k} + S_\epsilon \tag{2.10}$$

In these equations, G_b represents the generated turbulent kinetic energy due to buoyancy, which is neglected in this research. Y_m is set to zero since the value of this term is related to compressible flow. S_k and S_ϵ are user-defined source terms which are also set to 0 in this research. G_k and μ_t are the turbulent kinetic energy generated by the mean velocity gradients and the turbulent viscosity, respectively. Their expressions are:

$$G_k = -\rho\overline{u_i' u_j'}\frac{\partial u_j}{\partial x_i} \tag{2.11}$$

$$\mu_t = \rho C_u \frac{k^2}{\epsilon} \tag{2.12}$$

Other parameters in the equations are constant. Their values have been determined from experiments for fundamental turbulent flows. The following default values have been proven to work quite well for a wide range of fluid flows:

$$C_{1\epsilon} = 1.44, C_{2\epsilon} = 1.92. C_\mu = 0.09, \sigma_k = 1.0, \sigma_\epsilon = 1.3$$

Shear-Stress Transport (SST) $k-\omega$ model

The shear-stress transport (SST) $k-\omega$ model was developed from the $k-\epsilon$ model. The transport equation for the SST $k-\omega$ model is:

$$\frac{\partial}{\partial t}(\rho k) + \frac{\partial}{\partial x_i}(\rho k u_i) = \frac{\partial}{\partial x_j}(\Gamma_k \frac{\partial k}{\partial x_j}) + G_k - Y_k + S_k \tag{2.13}$$

$$\frac{\partial}{\partial t}(\rho \omega) + \frac{\partial}{\partial x_j}(\rho \omega u_j) = \frac{\partial}{\partial x_j}(\Gamma_\omega \frac{\partial \omega}{\partial x_j}) + G_\omega - Y_\omega + D_\omega + S_\omega \tag{2.14}$$

In this equation, G_k still represents the production of turbulent kinetic energy and it is defined in the same manner as above. Γ_k and Γ_ω are the effective diffusivity of k and ω, respectively. They are given by:

$$\Gamma_k = \mu + \frac{\mu_t}{\sigma_k} \tag{2.15}$$

$$\Gamma_\omega = \mu + \frac{\mu_t}{\sigma_\omega} \tag{2.16}$$

where σ_k and σ_ω are the turbulent Prandtl number for k and ω. The turbulent viscosity is again a function of k and ω and it has the following expression:

$$\mu_t = \frac{\rho k}{\omega}\frac{1}{max[\frac{1}{\alpha^*}, \frac{SF_2}{\alpha_1}\omega]} \tag{2.17}$$

G_ω is the generation of ω and it has the following expression:

$$G_\omega = \alpha \frac{\omega}{k} \tag{2.18}$$

α^* is a coefficient which damps the turbulent viscosity causing a low-Reynolds number correction and it has the following expression:

$$\alpha^* = \alpha_\infty^* (\frac{\alpha_0^* + Re_t/R_k}{1 + Re_t/R_k}) \tag{2.19}$$

where

- $Re_t = \frac{\rho k}{\mu \omega}$;
- $R_k = 6$;
- $\alpha_0^* = \frac{\beta_i}{3}$;
- $\beta_i = 0.072$;

When the $k-\omega$ model is in the high-Reynolds number form, $\alpha^* = \alpha_\infty^* = 1$. In this research, the low-Reynolds number correction is always applied in the simulation to represent the near-wall turbulence damping effects.

2.2.3. Near-Wall Treatment for Wall-Bounded Turbulent Flows

For turbulent flow, the presence of a wall plays a significant role since it imposes the no-slip boundary condition to the velocity profile. Since the solution variables have very large gradients in the region close to the wall, the near-wall modelling has a significant impact on the numerical solution.

It has been shown in various experiments that the velocity profile in the near wall region can be divided into three layers. Very close to wall, it is the viscous sublayer, in which the flow is almost laminar and dominated by the viscosity effects. Then the flow enters the logarithmic layer, in which the mean velocity has a logarithmic form. Finally, there is the outer layer or the fully turbulent layer. Turbulence plays the major role in this region. Between the viscous sublayer and the logarithmic layer, the transition area is called the buffer layer. Commonly, the dimensionless variables y^+ and u^+ are applied which have the following definitions:

$$\begin{aligned} u^+ &= \frac{\overline{u}}{u^\star} \\ y^+ &= y\frac{u^\star}{\nu} \end{aligned} \tag{2.20}$$

where $u^\star$ is the wall friction velocity which is defined by using the wall shear stress, where ν is the kinematic viscosity. The comparison between experimental data and the theoretical profiles for the viscous sublayer and for the logarithmic layer shows that the viscous sublayer profile is valid for $y^+ < 5$ and that the logarithmic profile is valid for $y^+ > 30$. It was also found that the solution of the viscous sublayer and that of the logarithmic layer match at about $y^+ = 11.5$.

Normally, two approaches are used to model the flow in the near wall region. One of them is to use wall functions which are semi-empirical formulas aiming at representing the flow in the viscosity-affected region and connecting this region with the outer region. In this method, the flow in the viscous sublayer and in the buffer layer are not explicitly resolved and the value obtained from the wall function is assumed to be the start point of the logarithmic layer. Over the years, various types of wall functions have been developed and they have different requirements for the value of y^+ as listed below:

- The standard wall function is the default option in Ansys Fluent and it only resolves the flow profile by using the logarithmic layer. Apparently, the first mesh node has to lie in the logarithmic layer if this wall function is used. This imposes a required range for the value for y^+ (i.e. the first grid point away from the wall) must fall between 30 and 300;

- The scalable wall function overcomes the deterioration of the standard wall function when grid refinement gives a grid point that is located in the viscous sub layer. It produces consistent results for the value of y^+ at 11.225 for grids of any refinement.

- The enhanced wall treatment for the $k-\epsilon$ model is actually a near-wall modelling method which requires the near wall mesh to be fine enough to resolve the viscous sublayer.

For the application of the standard $k-\epsilon$ model in Fluent, a wall function is required. The scalable wall function is adopted as the wall function in this study due to its powerful adaptation to mesh refinement.

Except for the wall function method, another method, which is called the near-wall modelling approach, was also developed. This method requires the turbulence models to resolve the flow all the way to the wall including the viscous sublayer. Therefore, the mesh is required to be fine enough to simulate the flow in the viscous sublayer. The SST $k-\omega$ model with low-Reynolds number modification aims at resolving this area and therefore requires an appropriate mesh resolution to do this with good accuracy. As has already been stated, the value of y^+ needs to be smaller than 5 to fall within the viscous sublayer. More strictly, for flows with a changing pressure gradient where separation is expected, the value of y^+ is even expected to be smaller than 1.

2.2.4. Governing Equations for the Undersized Ball Pig

The motion of the pig is driven by the incoming flow in the pipe. The general equation of the pig motion can be derived by applying Newton's second law to the pig:

$$m\frac{dV'_{pig}}{dt} = T \cdot S_{pig} - F_{fric} + mg_i \tag{2.21}$$

where m and V'_{pig} are the mass and velocity of the pig, respectively. The term on the left hand side is the acceleration of the pig and the ones on the right hand side are the forces exerted on the pig. The first term represents the surface force exerted by the fluid on the pig in axial direction. T is the surface force which can be decomposed into a pressure and viscous force by applying the constitutive equation and S_{pig} is the surface area of the pig. The second term is the friction force between the pig and the pipe wall. In this study, this friction term is not considered. The last term represents gravity which has a value of zero in the axial direction, as the pipe is horizontal.

The current study only focuses on the steady state simulation, which means that acceleration of the pig motion is not considered. The axial force is the quantity of most interest since the zero-drag point corresponds to the terminal velocity of the pig, which in turn determines the residence time of the pig in the pipe. In order to find the terminal velocity of the pig, the velocity of the pig is varied (through running multiple simulations) until the axial drag force exerted on the pig is found to be zero. In order to get a steady state simulation, the grid is connected to the pig, and the flow is solved in a framework in which the pipe wall is moving with respect to the pig.

2.3. Dimension Analysis

For engineering problems, dimension analysis is a very useful and broadly applied technique. It helps to analyze the relationships between different physical quantities and eventually simplifies the problems. It is also used in this study to figure out the fundamental relationship between different quantities involved in the problem. Among the various formal methods of dimension analysis, Buckingham's method is used to perform the dimension analysis in this research.

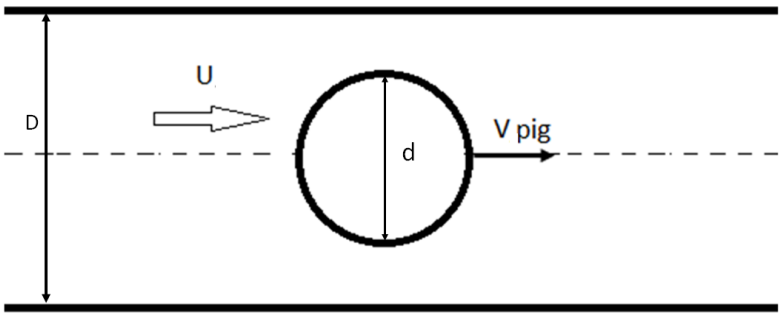

Figure 2.1: 2D simulation geometry

Figure 2.1 shows a 2D sketch of the flow domain after simplification. It can be seen from the figure that the key parameters involved in this problem are: the bulk velocity in the pipe (U), the pig terminal velocity (V_{pig}), the pipe diameter (D), the pig diameter(d) and fluid properties density (ρ) and viscosity (μ). The dimensions of those variables are listed in Table 2.1. It can be seen that the involved basic units are: length (m), mass (kg) and time (s). By applying Buckingham's theory, the following dimensionless groups can be found:

- The undersized diameter ratio d/D indicates the area contraction by the appearance of the pig for the flow to pass the pig.
- The normalized pig velocity V_{pig}/U is the ratio of the pig velocity and the bulk velocity. It shows how much liquid is by-passing the ball pig.

Table 2.1: Parameters and their dimensions involved in the problem

Parameter	Units
Pipe diameter (D)	$[m]$
Pig diameter (d)	$[m]$
Bulk velocity (U)	$[m][s]^{-1}$
Pig terminal velocity (V_{pig})	$[m][s]^{-1}$
Fluid density (ρ)	$[kg][m]^{-3}$
Fluid viscosity (μ)	$[kg][m]^{-1}[s]^{-1}$

- The bulk Reynolds number $Re = \rho UD/\mu$ describes the flow condition of the incoming flow.

According to Buckingham's theory, one of the above variable will be the function of the other two. In this research, the terminal velocity of the pig is the quantity of most interest. Therefore, the following relationship will be considered:

$$\frac{V_{pig}}{U} = f(Re, \frac{d}{D}) \tag{2.22}$$

2.4. Entrance Length

Since the current study focuses on the steady state simulation, only the flow in the fully developed region is considered. This means that the developing flow is not the realm of this study. To obtain the fully developed flow profile, a certain length before the pig is required. The length of the hydrodynamic entry region along the pipe is called the hydrodynamic entry length (L_h). It is a function of Re and for a horizontal circular pipe with diameter of D, its expression in various flow regimes has the following appearance [14]:

For laminar flow:

$$Lh_{laminar} = 0.05DRe \tag{2.23}$$

For turbulent flow:

$$Lh_{turbulent} = 4.4DRe^{1/6} \tag{2.24}$$

Apparently, this entrance length is a function of Re and it is shorter in the turbulent flow regime than in the laminar one.

3

Numerical Model Validation

For the steady state simulation of the flow around the undersized ball pig, the force in the axial direction is the quantity of most interest since it determines the flow motion of the pig. Therefore, it is very important that the numerical model, which is used to simulate the flow is capable to accurately predict the drag force. In this chapter, a test of the ability of Ansys Fluent to reproduce the flow around a sphere is studied by comparing numerical simulation results with experimental data. The benchmark data from the experiments of Schlichting [15] are used for the validation.

3.1. Flow Domain

The experimental data as described in the literature were obtained by conducting wind tunnel tests. For the simulation, it is important to investigate the size of the simulation domain to make sure that the simulation results are independent of the domain size. Nidhul et al.[16] concluded after a careful study that for a sphere with diameter D, a rectangular domain with dimensions $15D$ in upstream direction, $15D$ in transverse direction and $20D$ along downstream direction will be sufficient to simulate the flow. Therefore, those dimensions are also used in the present part of the simulations to capture the flow around a sphere in an open space. The diameter of the sphere is set to $0.01m$.

The behaviour of the flow around a sphere changes dramatically when Re increases in different flow regimes. Jones and Clarke[17] stated that the nature of the flow around a sphere varies from steady to unsteady and from axisymmetric to asymmetric when the Reynolds number increases. In order to capture the phenomena observed in the experiments, both 2D and 3D simulations are performed and the simulation results are compared with experimental data.

For the 3D simulations, the simulation domain is a rectangular hexahedron which has the same dimension as has been suggested by Nidhul et al.. It is not possible to use the same rectangular domain for the 2D simulation. Therefore, there is a need to do the 2D simulation in a cylinder so that the axisymmetric assumption can be applied. Inspired by the dimension of the rectangular hexahedron, the size of the cylinder in the upstream and downstream directions of the sphere are also set to $15D$ and $20D$, respectively, and the lateral side dimension is set to $15D$. The sphere is located along the centre line of the cylinder. The geometries for both the 2D and 3D simulations are shown in Figure 3.1 and Figure 3.2, respectively.

3.2. Parameters and Boundary Conditions

The fluid used in this part of the simulations is air which has a viscosity and density of $1.7894 \times 10^{-5} kg/(ms)$ and $1.225 kg/m^3$, respectively. The fluid flows in the positive X direction and the velocity various from $7.3 \times 10^{-4} m/s$ to $1.46 \times 10^{4} m/s$, which gives a wide range of the Reynolds number from 0.5 to 10^7. The Reynolds number in this part is defined by the fluid velocity and the sphere diameter.

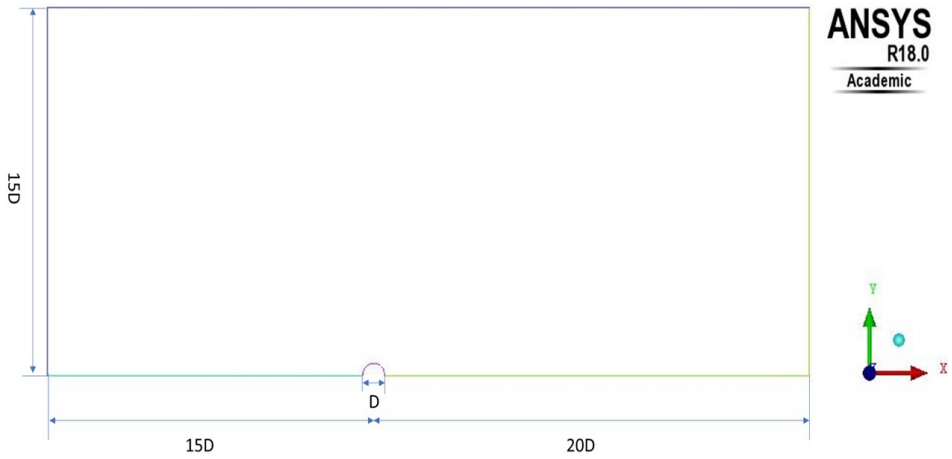

Figure 3.1: 2D simulation geometry

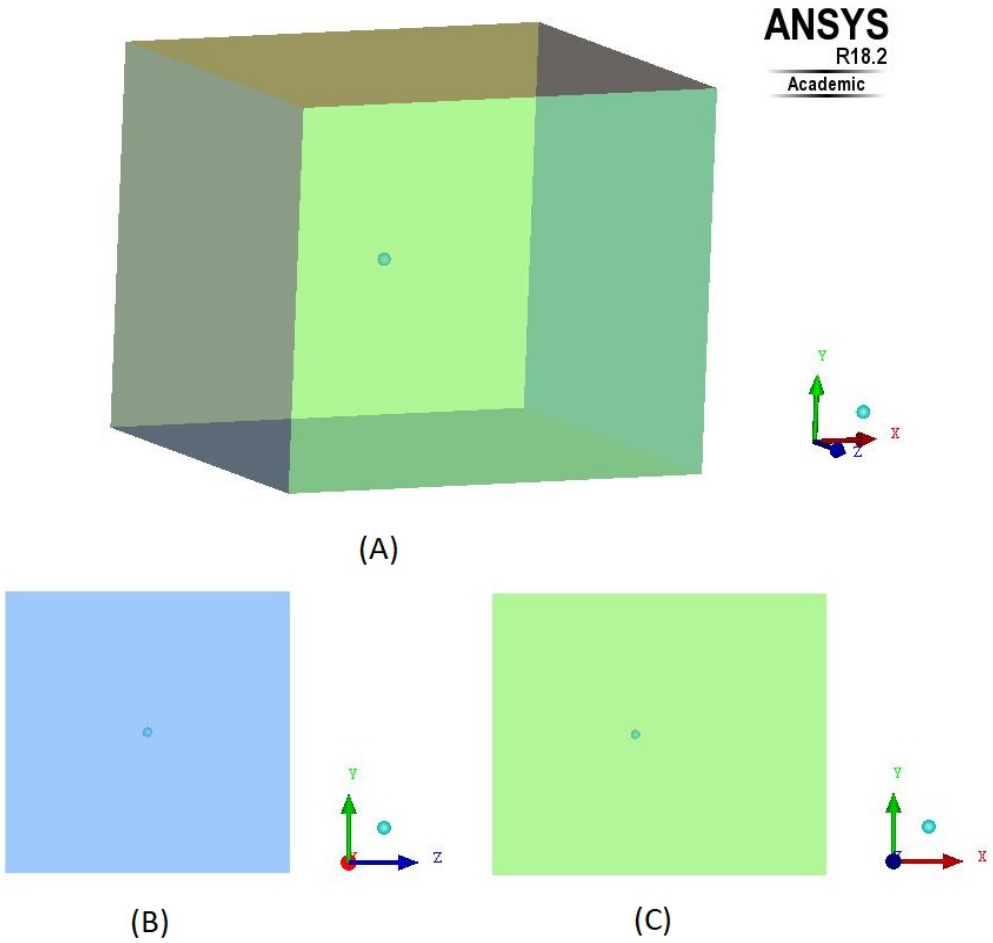

Figure 3.2: 3D simulation geometry (A: 3D view; B: front view; C: side view)

As has been explained in Chapter 2, the standard $k-\epsilon$ model with the scalable wall function and the SST $k-\omega$ model with low-Reynolds number modifications are used for the simulation of the turbulent flow. Default values of the model parameters are used for the turbulence models.

The experimental results were obtained for a uniform incoming flow past a sphere. Therefore, the

boundary conditions in the simulation have been appropriately set such that a uniform incoming flow velocity is generated. For the 2D simulation, the left and the top face in Figure 3.1 are both chosen to velocity inlet boundary conditions. The velocity components in the x direction for both these two faces are set to the fluid velocity which is used for the calculation of Re. The face downstream of the sphere has been given a prescribed outflow. The centre line, which is located at the bottom of Figure 3.1, serves as the axis boundary condition. The surface of the sphere has a stationary wall boundary condition. For the 3D simulation, the faces at the upstream side and at the lateral side are all given as velocity inlet boundary conditions. The outflow and stationary wall boundary conditions are again used for the outlet and for the surface of the sphere.

3.3. Mesh Generation

In this study, the mesh is generated by using the Ansys ICEM-CFD. This tool applies a topology block concept to generate the mesh based on the shape of the simulation domain. Given the geometry of the simulation domain, it is possible to generate a structured mesh in Ansys ICEM-CFD with an O-grid operation due to the existence of the sphere. Therefore, all the meshes used in this part of the simulations are structured, which largely saves computational time.

The mesh size has been modified and refined in various flow regimes to satisfy the corresponding requirements from the numerical models that are used. In the low-Re regime, where the turbulence model is not used, there is no extra requirement for the mesh size close to the wall region, and therefore the mesh nodes are uniformly distributed. When the Reynolds number is in a flow regime where the turbulence model has to be used, the mesh size in the area close to the wall will need some extra refinement since the first grid cell has to lie in a certain region to satisfy the condition of the corresponding wall treatment strategy. When a low-Reynolds number modification is used, the location of the first grid cell has to be sufficiently close to the wall so that the value of y^+ will be smaller than 1. The application of the standard $k-\epsilon$ model with scalable wall function, however, has a less strict requirement on the value of y^+ next to the wall. This is because it elegantly offers an appropriate solution by virtually displacing the mesh to the location where y^+ is 11.225 irrespective of the level of refinement. This means that no extra attention is needed when the scalable wall function is used. Therefore, the mesh which satisfies the requirement of the SST $k-\omega$ model was also used for the calculation when the $k-\epsilon$ model is used. In the calculation where the SST $k-\omega$ model is used, the value of y^+ at the first grid cell along the surface of the sphere was always checked after each simulation when the Reynolds number is increased. As long as the value of y^+ is found to be above 1, the mesh close to the wall area will be refined. Eventually five mesh refinements have been made for the 2D simulation and two mesh refinements were used for the 3D simulation. The number of grid cells for each refinement and the corresponding Re calculation range is shown in Table 3.1. Structured meshes are generated in the whole domain; the grid cells listed in Table 3.1 are quadrilateral cells for the 2D mesh and hexahedral cells for the 3D mesh. In Figure 3.3 and Figure 3.4, some details of the mesh used in both the 2D and 3D simulations are shown, respectively.

Table 3.1: Meshes as used for the validation of the drag coefficient

Name	Mesh number	Calculation Re region
2D_mesh1	18,820	0.5 - 5E3
2D_mesh2	107,098	5E3 - 1E4
2D_mesh3	113,518	1E4 - 2E5
2D_mesh4	227,228	2E5 - 1E7
2D_mesh5	436,108	2E5 - 1E7
3D_mesh1	1,757,088	200 - 1E4
3D_mesh2	3,751,538	200 - 1E4

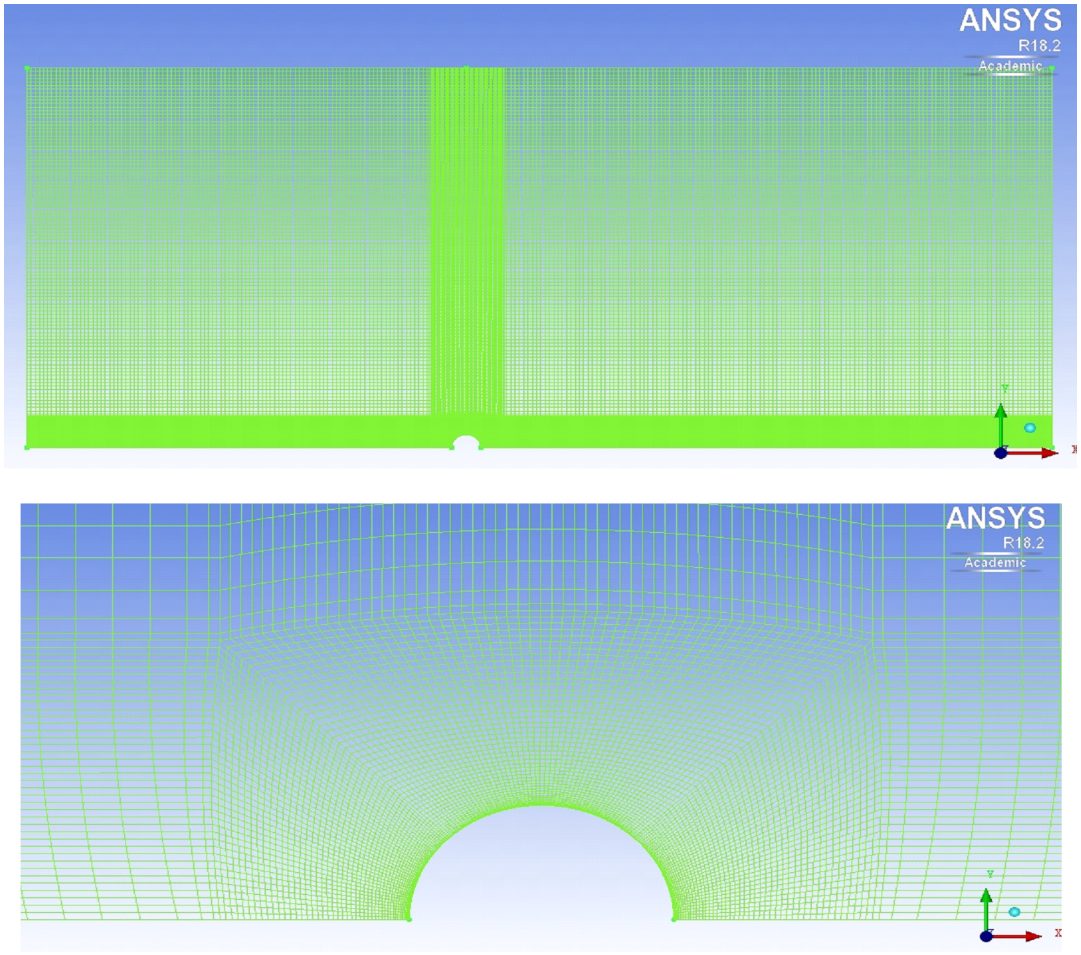

Figure 3.3: Detailed 2D mesh as used in the model validation

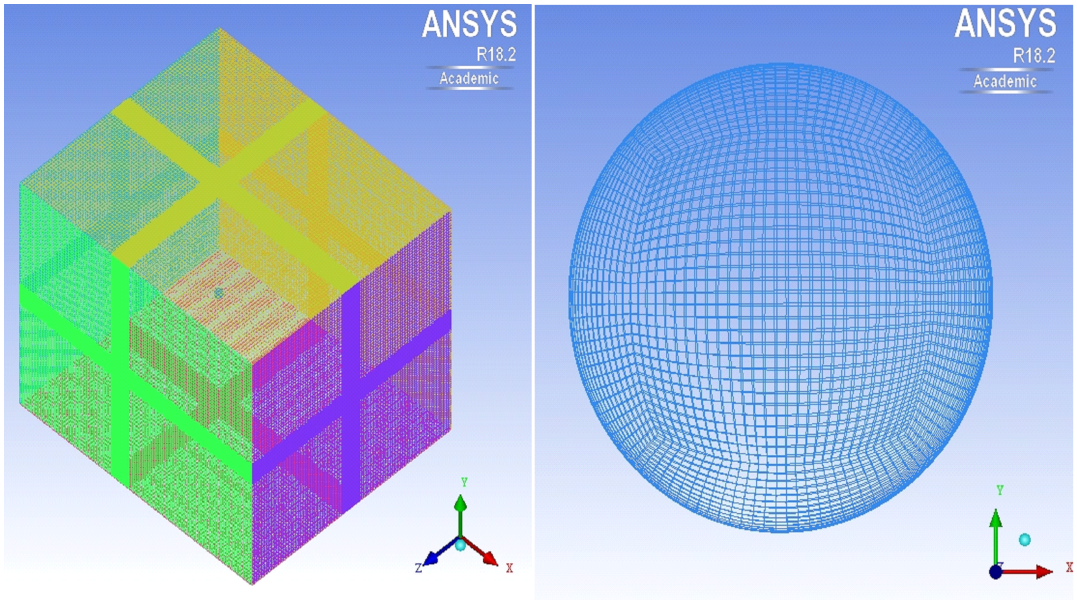

Figure 3.4: Detailed 3D mesh as used in the model validation

3.4. Discussion of the Simulation Results

Jones and Clarke [17] elaborated in their research that the behaviour of the flow past a sphere experiences several different flow regimes and the detailed flow behaviour is very sensitive to the change of Re. The flow past a sphere will eventually reach steady state and the drag coefficient becomes constant at a given Re when Re is smaller than 210. The detailed flow field also shows that the flow is axisymmetric in this region, but the axisymmetry is lost when Re is above 210. Then unsteadiness is clearly observed when Re is above 280 and the flow field gives periodic vortex shedding when Re is between 280 and 400. When Re is above 400, the flow is observed to become more and more irregular. The flow experiences a transition when Re is reaching values between around 800 to 1000 where the turbulent wake is generated. This flow region continuous until Re reaches the so-called critical value of 3.8×10^5, where the flow undergoes a transition to turbulent flow.

Apparently, the behaviour of the flow around a sphere is very sensitive to the change in Re. This study aims at reproducing the flow characters at various Reynolds numbers by using Ansys Fluent and hence at finding out the most appropriate numerical model to predict the drag coefficient of the flow past a sphere. Therefore, the drag coefficient as computed in the simulation will be compared with the experimental data.

3.4.1. Steady Axisymmetric Flow Regime

This section describes the flow over a sphere when Re is between 0.5 to 200. Since the flow was found to be steady and axisymmetric in the experiments [18], the simulation results as obtained by using 2D and 3D geometries are expected to be the same. To validate this, 2D and 3D steady state simulations are performed in this regime. A laminar simulation was performed with the SIMPLE Pressure-Velocity Coupling method and the momentum equation is discretized by using a second-order upwind method. The 2D mesh1 and 3D mesh1 from Table 3.1 are used for the laminar simulation. The simulations converged quite rapidly after a few thousands of iterations and the drag coefficients eventually became constants. The comparison of the computed drag coefficient and the experimental values is shown in Figure 3.5. It can be seen that the results for the flow from both the 2D and 3D simulations are axisymmetric in this regime. This means that 2D simulation is good enough to capture the flow.

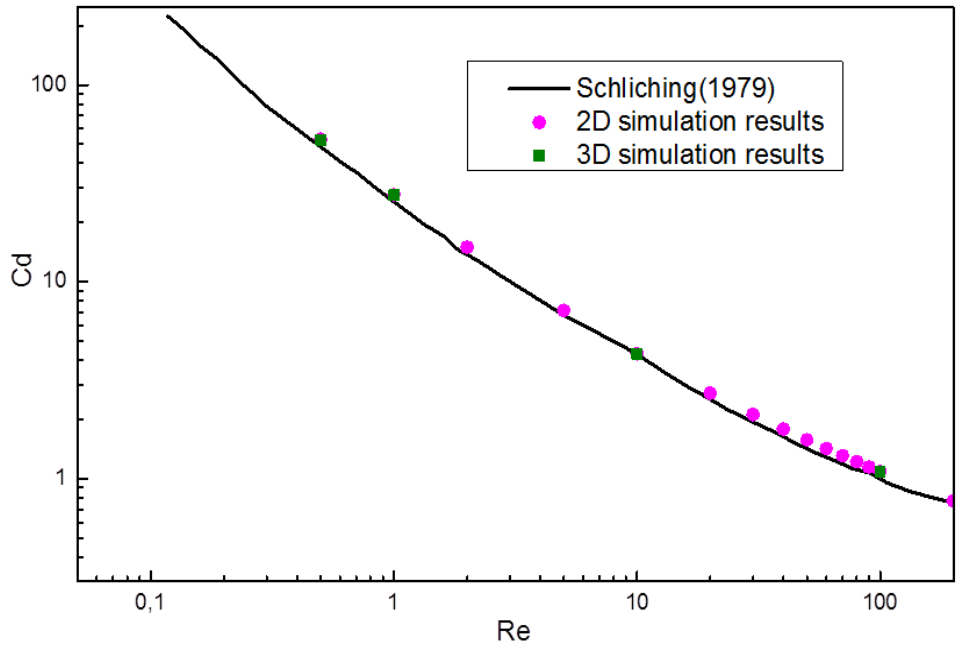

Figure 3.5: Comparison of the computed drag coefficient with the experimental results of Schlichting for Re < 200 [15]

To further check the axisymmetry of the flow, the detailed flow velocity fields from the 2D and 3D simulations are compared. It turns out that in this regime, the flow velocity field contours of two

perpendicular planes in the x-y plane and in the x-z plane, which both contain the x axis, are the same. Moreover, these velocity field contours are also found to be the same as those obtained from the 2D simulation. Figure 3.5 shows the comparison of the velocity field obtained in the 2D and 3D simulations at Re=100. The axial velocity profile at $x = 1D$ downstream of the sphere is also shown. It can be seen that the axial velocity profiles obtained from the 2D and 3D simulations are completely overlapping. This further validates that the flow in this region is steady and axisymmetric. Therefore, it is concluded that the 2D laminar simulation as carried out with Ansys Fluent is accurate enough to represent the flow around a sphere when Re is smaller than 200.

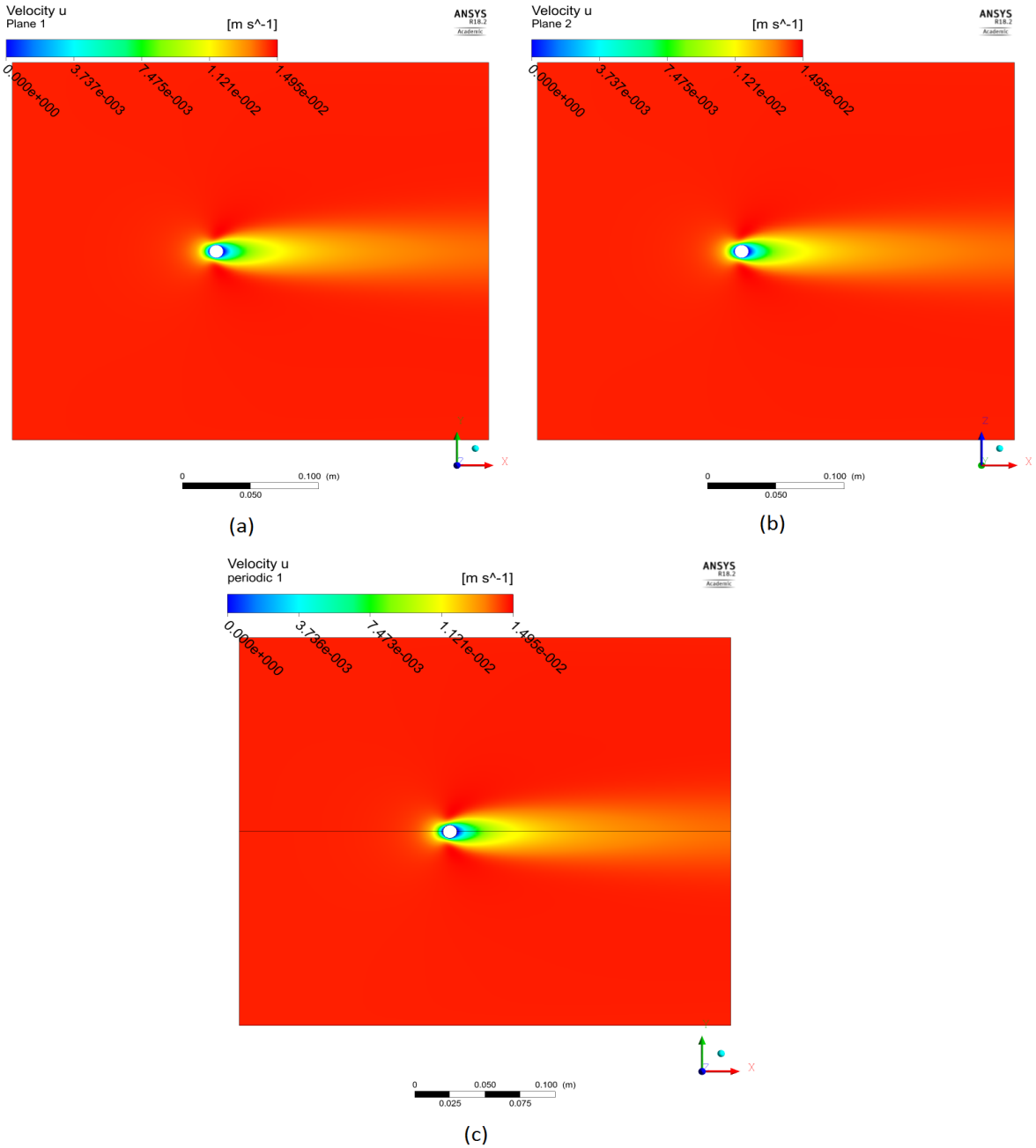

Figure 3.6: Comparison of the axial velocity field at different planes; a: x-y plane axial velocity contour from the 3D simulation; b: x-z plane axial velocity contour from the 3D simulation; 2D axial velocity contour

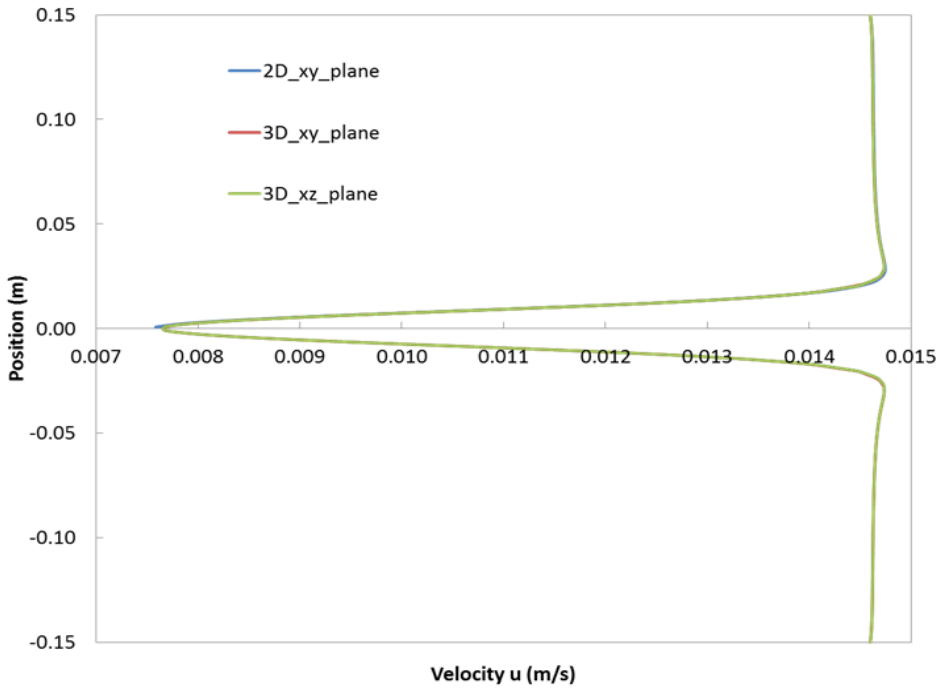

Figure 3.7: Comparison of the axial velocity profile at $x = 1D$ in the 2D and 3D simulations

3.4.2. Unsteady Asymmetric Flow Regime

According to Jones and Clarke [17], the axial symmetry and steadiness of the flow will be lost when Re is above 280 and the solution of the flow will become periodic. Therefore, a 3D simulation is necessary and a difference in the solution between the 2D and 3D simulations is expected in this region. The validation of the numerical model in this region started from the laminar simulation and the discretization methods are kept the same as those used in the steady axisymmetric flow regime. The simulation results show an essential difference when Re is 300 compared with the results in the steady axisymmetric flow regime. The 2D simulation is still very well converged after about 4000 iterations and the drag coefficient eventually became a constant of 0.632. For the 3D simulation, however, instead of becoming a constant, a periodic profile of the drag coefficient is obtained. Figure 3.8 shows this periodic profile, which has a (small) variation between 0.6638 to 0.66452. Compared with the result of 0.641, which is extracted from the experimental results curve, the 2D simulation slightly underpredicts the drag coefficient and the 3D simulation gives a slight overprediction.

When Re is increased further, the 2D laminar simulation turns out to consequently underpredict the drag coefficient and the difference between the computed and experimental values becomes larger and larger. In the 3D simulations, however, the periodic profile of the drag coefficient disappears and more chaotic profiles are obtained even after a large number of iterations. Figure 3.13 shows the comparison of the drag coefficient between the computed results for both the 2D and 3D laminar simulations and the experimental data when Re is increased between 300 and 50000. It can be seen that the 2D laminar simulation is not a good choice in this region since the predicted drag coefficients show some significant difference with the experimental data. As has been stated before, the 3D simulation generates fluctuating profiles of the drag coefficient. The data shown in the figure are obtained by taking the average value of the fluctuations. It can been seen from the comparison that the drag coefficient obtained from the 3D laminar simulation has a better agreement with the experimental data than the value obtained from the 2D simulation. Apparently, Fluent has successfully captured the onset of unsteadiness and the periodic solution of the flow when Re is 300. Even the transition from periodic flow to the more chaotic flow nature at a higher Re is very well captured.

The appearance of unsteadiness and asymmetry makes the simulation in this regime quite complex.

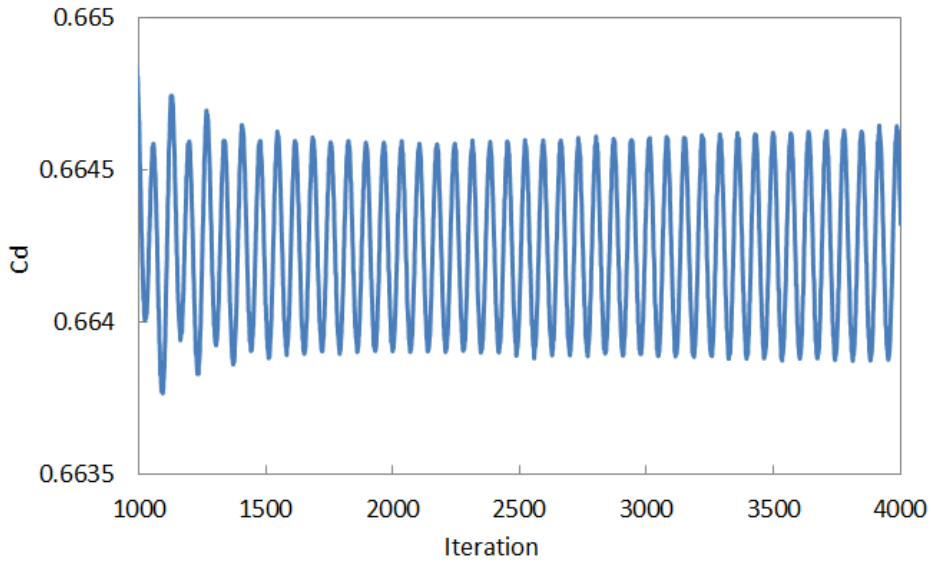

Figure 3.8: Drag coefficient profile at Re = 300

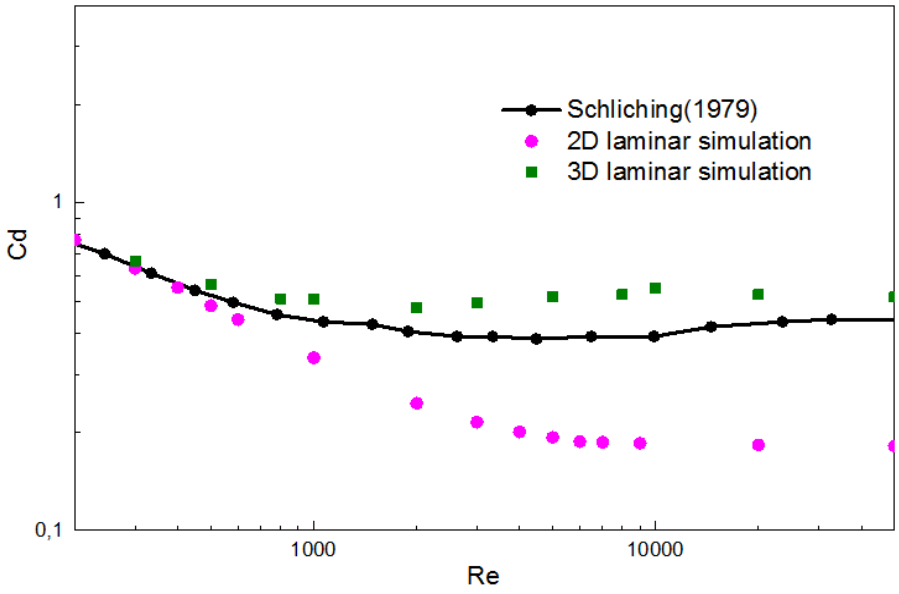

Figure 3.9: Comparison of the drag coefficient from the laminar simulations with the experimental data when 200 < Re < 50000

Apparently, a 3D unsteady simulation is required if a turbulence model is not used. To find the optimal way to simulate the flow, 2D turbulent simulations in this regime are also performed. The standard $k-\epsilon$ model with scalable wall function and the SST $k-\omega$ model are used.

For the simulation in this regime, the 2D mesh1, mesh2 and mesh3 from Table 3.1 are used, because when Re increases, the thickness of the boundary layer also changes. As was stated in Chapter 2, the value of y^+ at the first grid cell along the wall should be smaller than 1 when the SST $k-\omega$ model is used. Therefore, the mesh is successively refined to satisfy this requirement since it was found that the turbulent simulation with SST $k-\omega$ model is very sensitive to the value of y^+. Figure 3.10 shows the y^+ profiles generated by using the three different meshes at four different Reynolds numbers. It can be seen that the values of y^+ are all well controlled to be under 1 by mesh refine-

ment. At the same time, it can also be found that when y^+ is smaller than 1, the value of y^+ is equal to $y*$. Figure 3.10 (A) shows the profile at Re = 3000 when mesh1 is used for the simulation. The maximum value of y^+ at this Reynolds number is around 0.7. It is found that when Re is increased to around 5000, the maximum value of y^+ increases to around 1 and the profiles of $y*$ and y^+ are not completely overlapping any more. Therefore, mesh2 is generated by refinement close to the sphere surface. The values of y^+ after this refinement are shown in Figure 3.10 (B) at Re = 6000. When the Reynolds number again increases to around 10000 in Figure 3.10 (C), the maximum value of y^+ has increased from around 0.3 to 0.9, which leads to the need for further grid refinement by using mesh3. The maximum value of y^+ and y^* has decreased again to around 0.3 by this new mesh refinement.

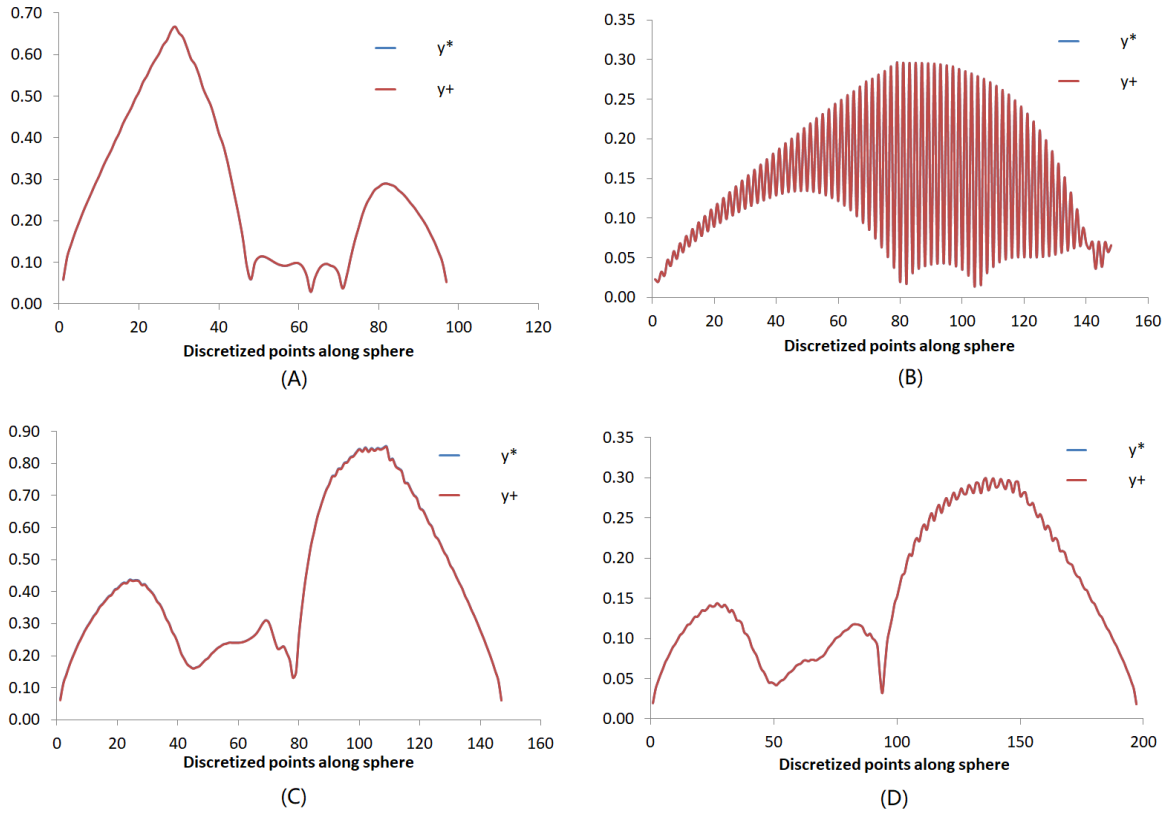

Figure 3.10: Profiles of y^+ along the sphere at a Reynolds number of: A) 3000 with mesh1; B) 6000 with mesh2; C) 10000 with mesh2; D) 20000 with mesh3

Although it has been stressed that the value of y^+ is very important for the mesh quality, a minimum number of nodes between 10 to 20 within the boundary layer is required. Therefore, the number of grid cells in the wall normal direction should always be checked to make sure that at least 10 cells are located in the wall layer. The quality of the numerical solution can be verified by at least plotting the turbulent viscosity profile perpendicular to the wall boundary condition. A clear maximum should be visible in the mid of the boundary layer. The simulation results with the SST $k-\omega$ model are found to be of high quality if the value of y^+ is well controlled and if the overall flow in the boundary layer is well resolved.

The comparison between the computed results and the experimental data shows that the predictions with the SST $k-\omega$ model using the low-Reynolds number correction lie nicely on the drag coefficient curve obtained from the experiment. In contrast to this, the results obtained with the $k-\epsilon$ model underpredict the value of the drag coefficient in this regime. Therefore, the SST $k-\omega$ model with low-Reynolds number correction is selected as the best model to simulate the flow around a sphere when Re is between 300 and 50000.

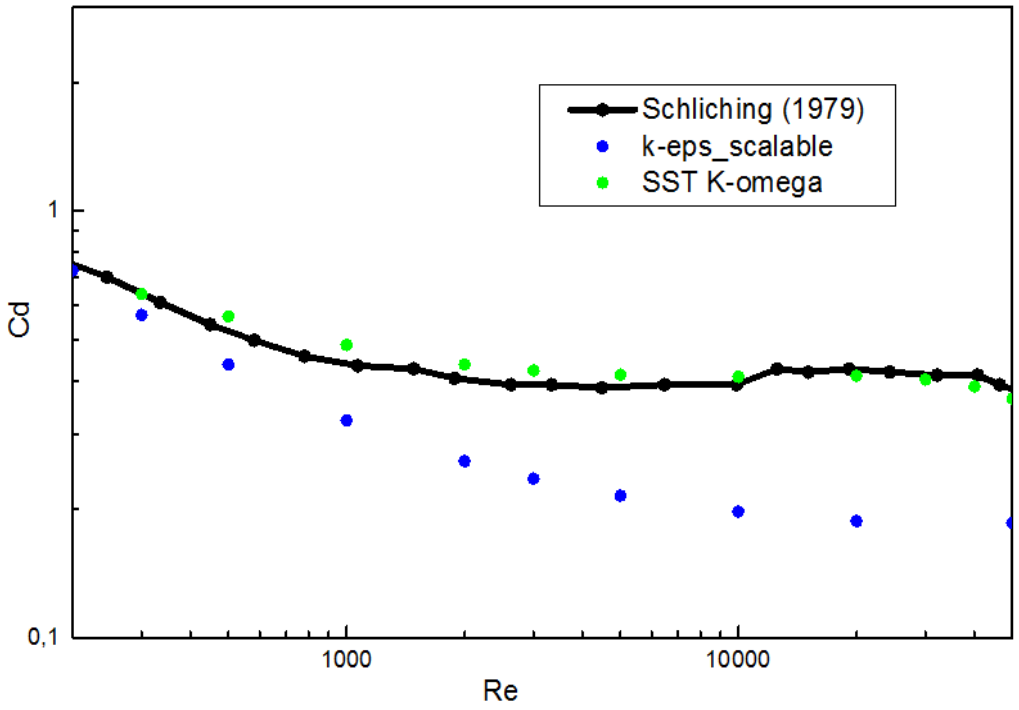

Figure 3.11: Comparison of the drag coefficient in the experimental results and the turbulent simulations when 200 < Re < 50000

Further attempts have also been made to validate the numerical models when Re is above 50000. The simulation results show that the two-equation models are not capable of capturing the boundary layer transition when the Reynolds number approaches the critical value. Although the mesh has been carefully refined in the wall region, the simulation results still show quite a large difference with the experimental data. Figure 3.12 shows the y^+ profile obtained by using mesh4 and mesh5 when Re = 200000. Apparently, the values of y^+ along the sphere for both mesh4 and mesh5 are below 1. Moreover, the number of grid cells within the boundary layer at Re = 200000 are 32 and 54 for mesh4 and mesh5, respectively. Apparently, the difference between the numerical results and the experimental data is caused by the limitation in the turbulence model. Therefore, it is concluded here that two-equation models are not suitable for the simulation of the flow around a sphere when Re is above 50000.

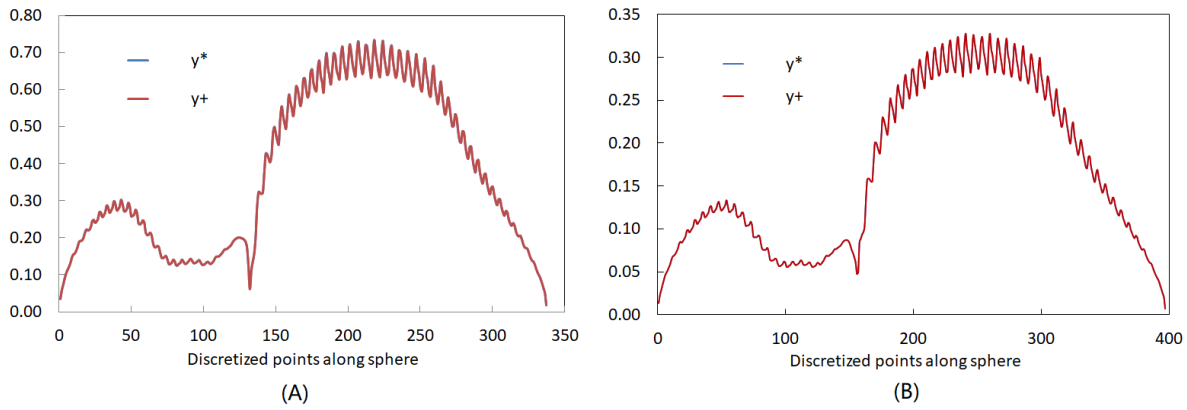

Figure 3.12: Profiles of y^+ along the sphere at a Reynolds number of: A) 200000 with mesh4; B) 200000 with mesh5

Based on the analysis as given above, it is concluded that for the flow past a sphere in the open space, the 2D laminar simulation in Ansys Fluent is sufficient to reproduce the flow when Re is smaller than 300. When Re is between 300 to 50000, the drag coefficient obtained from the 2D simulation with the SST $k-\omega$ model with low-Re correlation agrees very well with the experimental data. For the flow with Re higher than 50000, the two-equation models are not suitable. Those results are included in Figure 3.13 and they will be used for the simulation of the flow around the undersized ball pig in a pipe in the corresponding regimes.

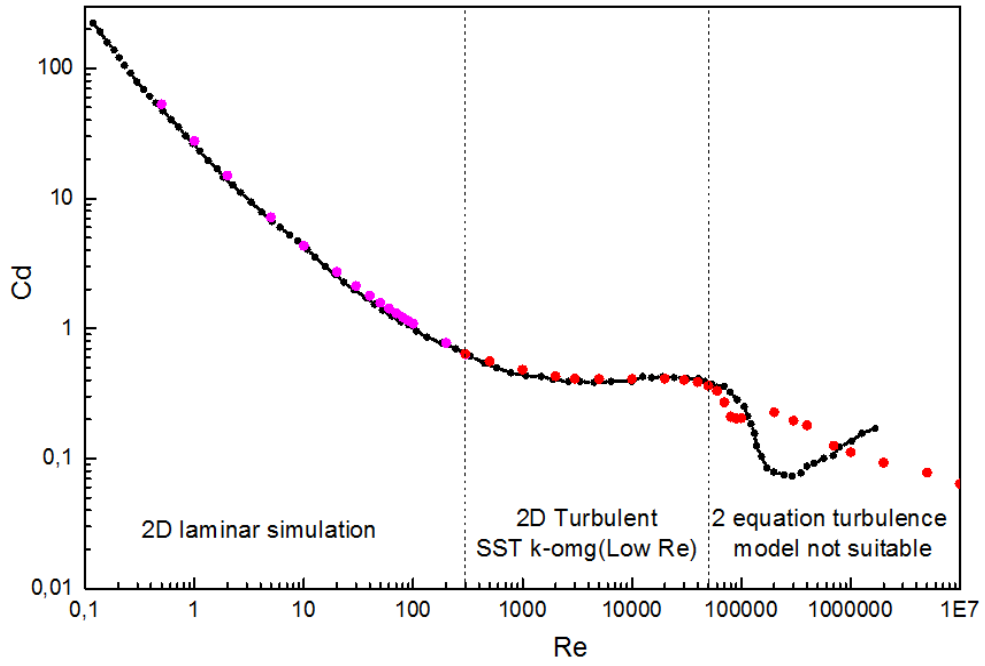

Figure 3.13: Comparison between the numerical simulations and the experimental data

4

Results for the Flow around an Undersized Ball Pig in a Pipe with Fixed Diameter Ratio

In the previous chapter the appropriate numerical models which can be used to simulate the flow around a sphere have been selected. In this chapter, the selected numerical models will be used to simulate the flow around an undersized ball pig in a pipe. The undersized ratio in this chapter is fixed at 0.5. Simulations are performed to find the equilibrium condition of the ball pig at various Reynolds numbers.

4.1. Flow Domain and Boundary Conditions

As has been stated in Chapter 2, simulations will be run under the axisymmetric assumption while the sphere is also assumed to be moving along the centre line of the pipe. Since the flow loop in the lab of the Process Energy Department has a pipe diameter of $52mm$, this same diameter is used in the simulation. This will enable a comparison with experimental results to be obtained in a future study. The diameter ratio of 0.5 gives a pig diameter of $26mm$. The length of the pipe requires further investigation and the results of which will be discussed later.

Figure 2.1 shows the schematic of the flow domain. In real applications, the flow enters the pipe at the inlet with an average velocity U and leaves the pipe at the outlet. The pig is driven by the incoming flow and moves with the terminal velocity V_{pig}. The pipe is stationary which gives a zero fluid velocity at the pipe wall. The simulation of this domain in the frame of reference attached the pipe is quite challenging since it requires a moving mesh around the pig. An alternative is to change the frame of reference to one that is attached to the pig, so that the pig remains stationary. In this new system, the velocity of the pig is set to zero and the pipe wall will be moving with a negative pig velocity. Accordingly, the average velocity of the incoming fluid will become $U - V_{pig}$. The transformed simulation domain and the corresponding velocity changes are shown in Figure 4.1 and in Table 4.1.

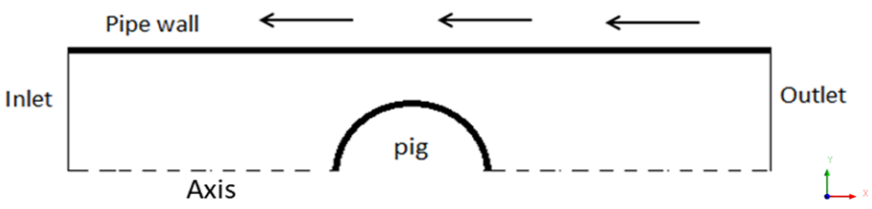

Figure 4.1: Flow domain for the simulation at a diameter ratio of 0.5

Table 4.1: Transformation of the velocity in two different frames of references

Boundary	Pipe's frame	Pig's frame
Inlet	U	$U - V_{pig}$
Pig	V_{pig}	0
Pipe wall	0	$-V_{pig}$

4.1.1. Boundary Conditions

This research focuses only on the simulation of the flow around an undersized ball pig at steady state. Hence it is assumed that the incoming flow is fully developed. As was discussed in Chapter 2, to obtain a fully developed velocity profile, the required upstream pipe length is a function of Reynolds number. For instance, the required entrance length for pipe flow with a Re of 50000 will be approximately 27 times the pipe diameter. Apparently, this length is too long if it is used as the pipe length upstream of the pig as this will give a too long computational time. To save computational time, first a simulation was made to obtain the fully developed velocity profile. Thereafter the obtained velocity profile is set as the inlet boundary condition in a new simulation with the pig (through the user defined function, UDF, as available in Fluent). By doing this, the computational length before the ball pig can be dramatically decreased.

The fully developed velocity profile can be obtained in two ways. The first one is to use a uniform velocity as inlet boundary condition with a pipe length of the required entrance length to allow the flow to develop until the profile is independent of the axial position. The second one is to use a periodic boundary condition and the pipe length in the simulation can be very short. The latter method is preferred since it requires a smaller computational domain, which helps to save computational time.

In order to validate the application of the periodic boundary condition method, the fully developed velocity profiles obtained by the two mentioned methods are compared for Re = 10670. At the same time, simulations in the two reference frames (i.e. for the pipe only, thus without pig) are also run to check whether the moving wall will influence the detailed flow field. The pipe length is set to $52mm$ for the simulation with the periodic boundary condition and to $4m$ for the simulation with the uniform velocity inlet boundary condition. The mesh sensitivity analysis shows that the simulation results are independent of the mesh when the number of grid cells in the direction perpendicular to the wall is above 200. Therefore, a mesh with 200 grid cells in the vertical direction is used here. To specify the uniform velocity as the inlet boundary condition in the turbulent flow regime, two extra parameters are required. In this study, the turbulence intensity and the turbulent length scale are used. The value of turbulent length scale is taken equal to the pipe diameter. The turbulent intensity is calculated from:

$$I = \frac{u'}{U} = 0.16(Re)^{-1/8} \tag{4.1}$$

For the simulation with periodic boundary conditions, the mass flow rate is specified by using the incoming fluid velocity ($U - V_{pig}$). The precise values of the boundary conditions are listed in Table 4.2.

Figure 4.2 shows the comparison of the fully developed velocity profiles as obtained with the different methods in the two frames of reference. The simulation results are transformed into the pipe's frame of reference for comparison. It can be seen that those two methods give the same velocity profile and the simulation results are thus independent of the frame of reference. Therefore, it has been proven that changing the frame of reference to the pig's frame and getting a fully developed velocity profile by using periodic boundary conditions do not affect the simulation results and these will thus be used in the simulations for the rest of the study.

The surface of the pig has a stationary wall boundary condition since the simulation is in the pig's frame of reference. Due to the motion of the pipe wall, a reverse flow at outlet will be introduced. Since the pressure outlet boundary condition gives a strict restriction on the pressure field, it is difficult

Table 4.2: Boundary conditions as used in the comparison at the two frames of reference

	Face	BC type	Parameters	Value	
				Pipe's frame of reference	Pig's frame of reference
Uniform velocity inlet BC method	Inlet	Velocity inlet	Velocity magnitude (m/s)	3	0
			Turbulent intensity $(\%)$	5	0
			Turbulent length scale (m)	0.052	0.052
	Outlet	Outflow	Flow rate weighting	1	1
	Pipe wall	Wall	Speed (m/s)	0	-3
Periodic BC method	Periodic condition		Mass flow rate (kg/s)	7.805E-3	0
	Pipe wall	Wall	Speed (m/s)	0	-3

to obtain converged results when the pressure outlet boundary condition is used at the outlet. By using an outflow boundary condition, however, the simulation did converge much easier. Therefore, the outflow is used as the outlet boundary condition. Based on the above study, boundary conditions at different faces in Figure 4.1 are defined accordingly and they are listed in Table 4.3.

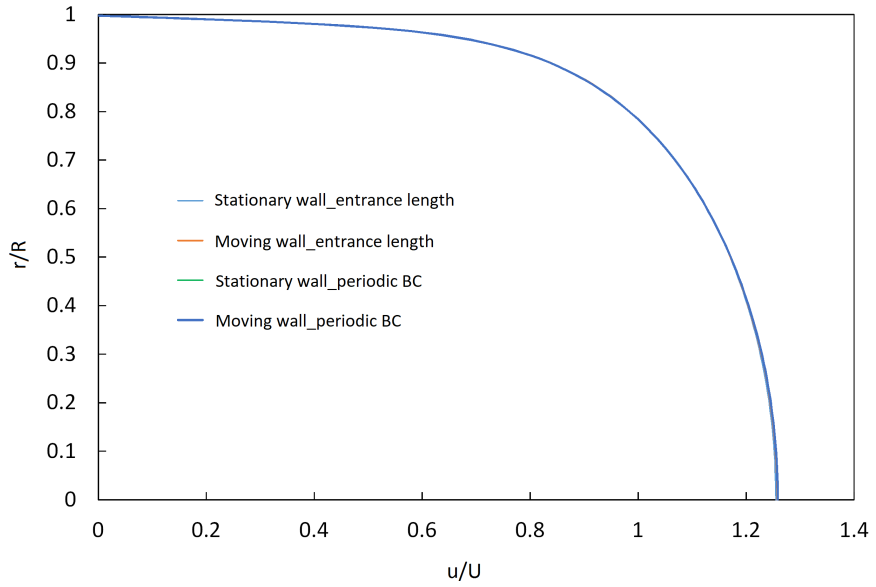

Figure 4.2: Comparison of the axial velocity profiles with various boundary conditions

4.1.2. Pipe Length

By specifying the fully developed velocity profile as the inlet boundary condition, the computational length before the ball pig can be significantly decreased. Of course, this length should still be long enough to capture the flow change due to the presence of the ball pig. To select this length, a simulation is run with a pipe length of 1 m before the ball pig when Re is 10670 using the pig's frame of reference. A fully developed velocity profile is first obtained and then imported as the velocity inlet boundary condition. The flow enters the inlet at $x = 0$ and moves along the x axis. The centre of the pig is located at $x = 1m$. The pipe wall moves with a speed of $-3m/s$. The computed axial velocity profile at various stream wise locations is shown in Figure 4.3. It can be seen from the figure that the velocity profile at $x = 0.9m$ is obviously affected by the presence of the ball pig. The velocity

Table 4.3: Boundary conditions for the flow around an undersized ball pig

Faces	Boundary condition type
Inlet	Velocity inlet (UDF)
Outlet	Outflow
Pig	Wall (stationary)
Pipe	Wall (moving)
Axis	Axis

profile at $x = 0.8m$ is already very close to the fully developed velocity profile. Moving to the location $x = 0.7m$, the comparison shows that here the velocity profile is completely overlapping with the fully developed velocity profile. Apparently, a pipe length of $0.3m$ before the sphere is enough for the flow to develop. Therefore, this length of $0.3m$ is used as the pipe length before the ball pig. The pipe length downstream of the pig is also set to $0.3m$, without further investigation.

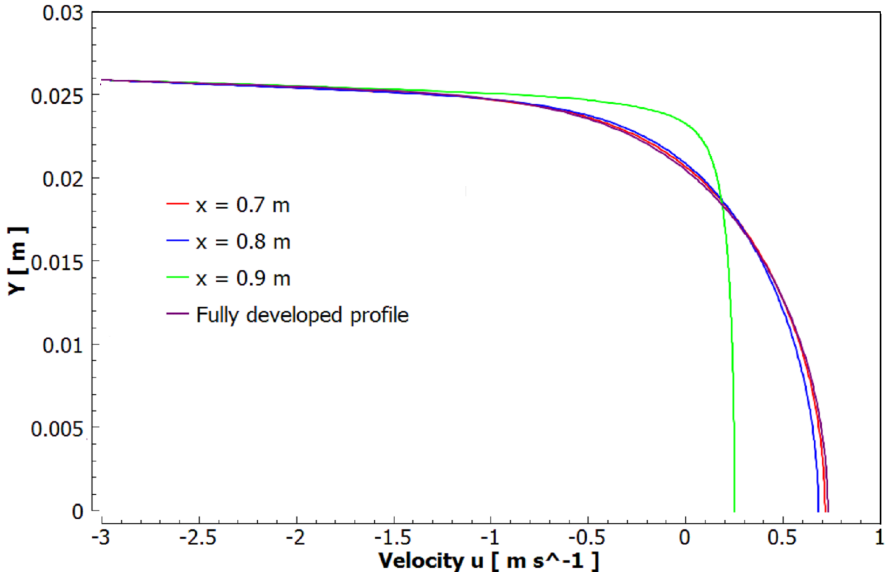

Figure 4.3: Comparison of the axial velocity profiles at different axial positions

4.2. Mesh Generation and Parameters

Compared to the simulation domain used in Chapter 3, which considered the flow in an open area, the simulations in the present chapter consider the flow that is contained in a circular pipe. Therefore, the same mesh strategy as used in Chapter 3 is used here with an extra refinement close to pipe wall and close to the surface of the sphere. Structured meshes are generated by cutting the O-grid around the pig. Figure 4.4 shows the extra refinement around the pig and close to the pipe wall for mesh1.

The SST $k - \omega$ model has been selected as the turbulence model. The same requirements for the value of y^+ and the discretization resolution in the boundary layer also applies to the simulation in this part. Three different meshes are selected for the simulations in which Re varies from 36 to 4.5E5. Each mesh is used for the simulation in a certain Re range. The details of these three meshes are shown in Table 4.4.

In the simulations, gravity is applied in the y direction, which means that it is not affecting the motion of the pig in axial direction. When Re < 1068, the laminar simulation is run with the SIMPLE

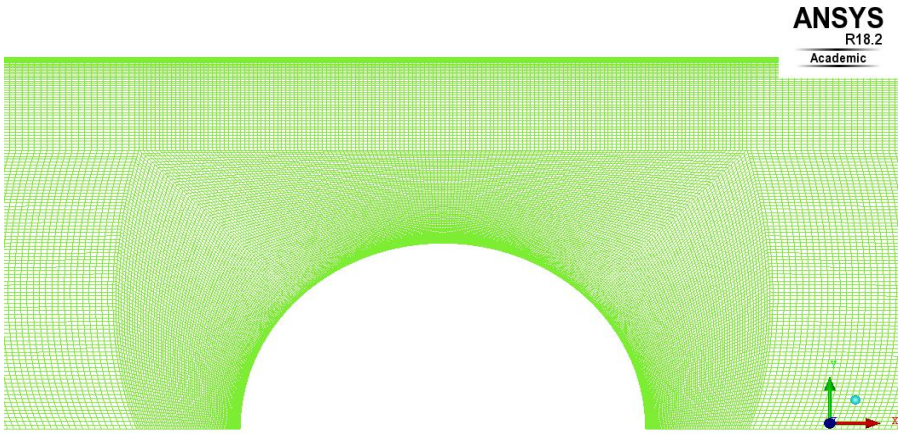

Figure 4.4: Mesh details around the ball pig

Pressure-Velocity Coupling method and the second-order upwind discretization method for the momentum equation. The SST $k-\omega$ model with low-Re number correction is used in the simulations when Re is larger than 2136. The default values of the parameters in the turbulence models are used and the under relaxation factors are adjusted at some Reynolds numbers to obtain converged results. The SIMPLE method is again used for the Pressure-Velocity coupling scheme. For the spatial discretization, the second-order method is used for the pressure and the first-order upwind method is used for the turbulent kinetic energy and for the specific dissipation rate.

Table 4.4: Mesh details for the simulation at a diameter ratio of 0.5

Mesh name	Mesh number	Calculation Re range
Mesh1	60898	36-71197
Mesh2	77638	71197-10677
Mesh3	210498	10677-427182

4.3. Force on the Ball Pig

This section first describes the overall momentum conservation in the computational domain and then analyzes the forces exerted on the ball pig at a low Reynolds number to understand the detailed stresses that are affecting the motion of the ball pig.

By applying the momentum conservation law over the entire flow domain, the following expression can be obtained:

$$F = \int_{inlet} (p + \rho uu) \cdot ds + \int_{outlet} (p + \rho uu) \cdot ds + \int_{wall} \tau_w \cdot ds \tag{4.2}$$

In this equation, F refers to the net force exerted on the ball pig. The right hand side contains different terms of the momentum change on the computational domain. The first and the second term represent the integration of the pressure force and of the net momentum entering and leaving the control volume, respectively. The third term is the integration of the wall shear stress.

For the motion of the ball pig, the quantity of most interest is the net axial force, which is a result of the above momentum balance. By definition, the axial component of the above net force F is the drag force (F_d) exerted on the ball pig which is the sum of the pressure force (F_p) and the viscous shear force (F_f) exerted on the pig.

$$F_d = F \cdot \hat{x} = F_p + F_f \tag{4.3}$$

Following the standard practice for the definition of the drag coefficient, two more similar parameters are defined to quantify the contributions of the pressure and viscous components in the overall drag coefficient:

$$C_d = \frac{F_d}{\frac{1}{2}\rho A U^2} \tag{4.4}$$

$$C_p = \frac{F_p}{\frac{1}{2}\rho A U^2} \tag{4.5}$$

$$C_f = \frac{F_f}{\frac{1}{2}\rho A U^2} \tag{4.6}$$

where ρ is the fluid density and A is the projected frontal area of the pig, which is calculated by: $A = \pi R^2$. U is the bulk velocity of the incoming flow in the pipe.

In this study, the prediction of the drag acting on the ball pig is very important since it helps to find the zero drag condition, which leads to the terminal velocity equilibrium condition for the pig. In practice, the pig is driven by the incoming flow in the pipe. Since this study only focuses on the steady state motion of the pig, the acceleration in the pig motion is not considered. Therefore, the zero drag condition is found by analyzing the forces exerted on the pig for various pig velocities. If the net axial force exerted on the pig is positive, then the pig will be essentially accelerating and a negative drag force means that the pig will be decelerating. The pig will only reach an equilibrium state when the drag force exerted on the pig is zero. The pig velocity is varied and the forces exerted on the pig at various pig velocities are computed until the zero drag point is found.

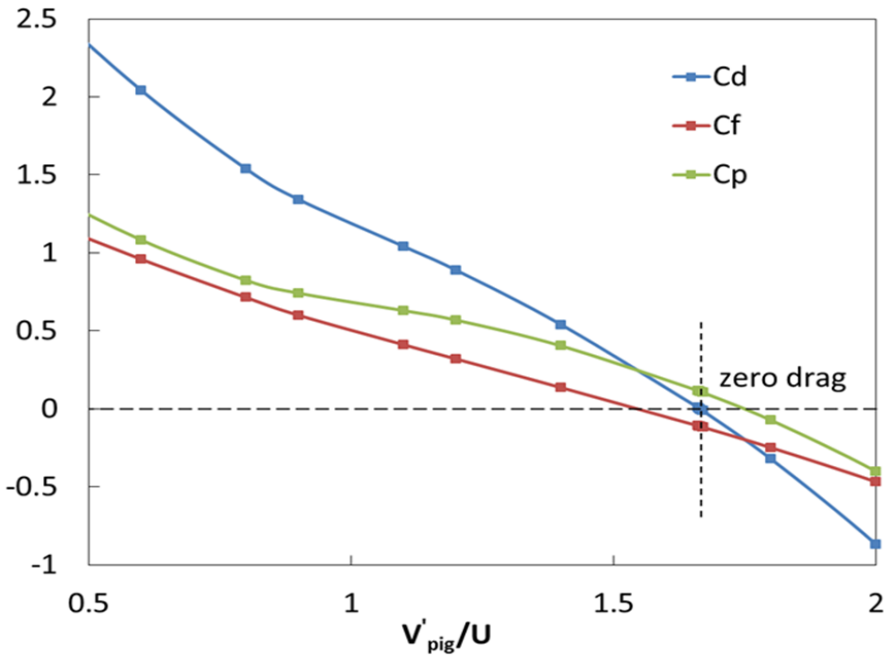

Figure 4.5: The computed drag and its components of the pressure and viscous shear for various pig velocities at Re = 178

Figure 4.5 shows the computed drag coefficient and its components of pressure and viscous shear for different pig velocities at Re = 178. The pig velocity is scaled with the incoming average fluid velocity and this will be used to quantify the change of the pig velocity in the rest of the analysis. To differentiate from the terminal velocity V_{pig}, the change of the pig velocity is denoted as V'_{pig}. Figure 4.5 shows that when the velocity of the pig is much lower than the fluid velocity, both the pressure and

viscous shear drag coefficient are positive, which leads to a positive overall drag coefficient. When the pig velocity increases, those two components decrease and the viscous drag first becomes negative at around $V'_{pig}/U = 1.52$. The force exerted on the pig then reaches the zero drag point which is labelled with the dash line in the figure at $V'_{pig}/U = 1.6642$. At the zero drag point, the negative viscous drag balances the positive pressure drag. This indicates that at the equilibrium point, the pig experiences a positive pressure force and a negative shear stress. When V'_{pig}/U is larger than 1.6642, all the three terms become negative and consequently the net force exerted on the ball pig becomes negative.

For laminar pipe flow, the fully developed velocity profile reaches its maximum value of $2U$ at the axis of pipe. Since the motion of the pig is driven by the incoming flow, the pig will be able to reach a maximum velocity of $2U$ when the pig diameter is extremely small. When the pig diameter increases, the terminal pig velocity will decrease. It will reach a value of $1.6642U$ when the pig diameter is half the pipe diameter. To better understand this relative flow motion, a comparison between the incoming fluid velocity profile occupied by the frontal area of the ball pig and the terminal velocity of the pig is sketched in Figure 4.6 (A). It can be seen that the incoming fluid velocity is larger than the pig velocity at the centre area and it is smaller than the pig velocity at the edge area of the ball pig. The fluid velocity profile along the vertical central line of the pig between the pipe wall and the pig is also shown in Figure 4.6(B). It shows that the derivative of the fluid velocity at the surface of the pig is negative which indicates a negative viscous shear force. According to the force information shown in Figure 4.3, this negative viscous shear force will be balanced by the positive pressure force and leads to a zero drag force. It can also be seen that the velocity profile shows some deviation from a linear profile.

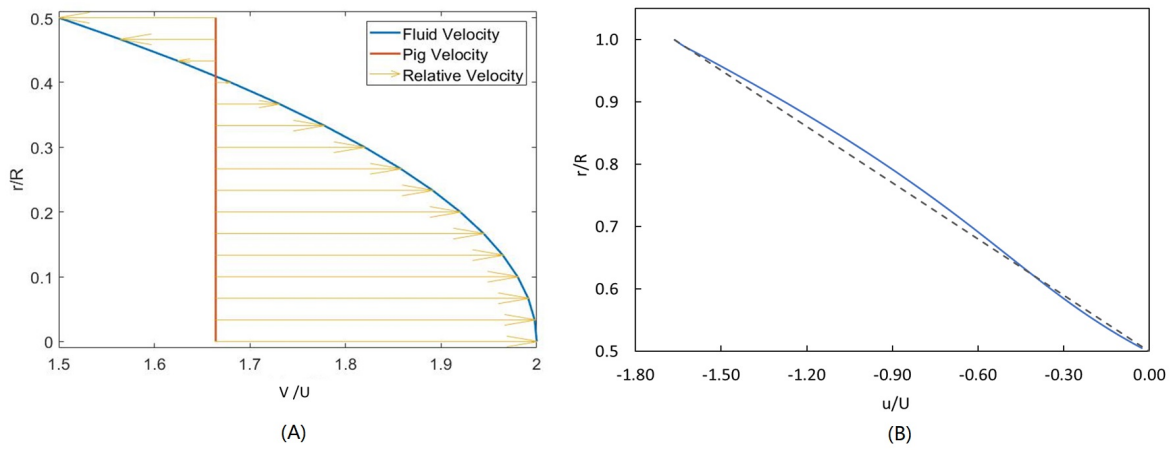

Figure 4.6: Velocity profiles of the pig and the fluid. A) Comparison between the incoming fluid velocity profile occupied by the frontal area of the ball pig and the terminal velocity of the pig at Re = 178; B) Fluid velocity profile along the vertical centre line of the pig between the pipe wall and the pig

4.4. Zero Drag Condition at Various Reynolds Numbers

Equation 2.22 from the dimension analysis shows that the normalized terminal velocity of a pig is a function of Reynolds number and of the pig diameter. After finding the zero drag point at one fixed Reynolds number, this section explores the zero drag condition at various Reynolds numbers.

Figure 4.7 shows the normalized pig terminal velocity against Re when the undersized diameter ratio is 0.5. The terminal pig velocity is explored when Reynolds number is in the range of 36 to 5E5. It can be seen that the normalized pig terminal velocity decreases when the Reynolds number increases and the profile experiences three different stages which are labelled as region A, region B, and region C in Figure 4.7. In region A, the normalized pig velocity decreases slightly from around 1.68 to 1.66. In region B, where Reynolds number is increased from 365 to 5340, the normalized pig velocity experiences a dramatic decrease from 1.66 to 1.246. Then in region C, the value of the normalized pig velocity first stayed in a stable range of around 1.2-1.23 and then decreased slightly at Re=71200.

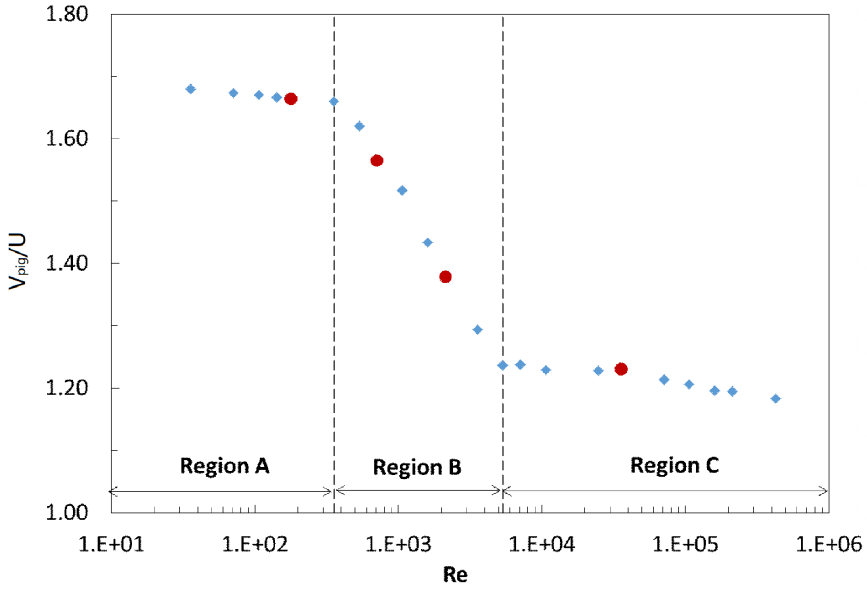

Figure 4.7: Normalized pig terminal velocity against Re at a diameter ratio of 0.5

After obtaining the normalized pig terminal velocity profile, it is also of interest to explore the driving factors of the pig's motion. Since the pig is driven by the incoming flow, the average fluid velocity in the pig projected area at various Re is computed and normalized by the incoming fluid velocity in Figure 4.8. The figure shows that in the laminar region when Re is smaller than 1067, the normalized fluid average velocity is a constant of 1.75. This constant can also be derived from the analytical solution of the pipe flow in the laminar regime. When Re is increased to 1600, there is a sudden change of the average fluid velocity profile due to the appearance of turbulence. Thereafter, the normalized fluid velocity decreases gradually when Re is increased. Apparently, the change of the fluid velocity profile from laminar to turbulent has been affecting the terminal velocity of the pig. To further figure out the dominant factor that affects the motion of the pig, the detailed force balance and the flow field in various regions are studied below.

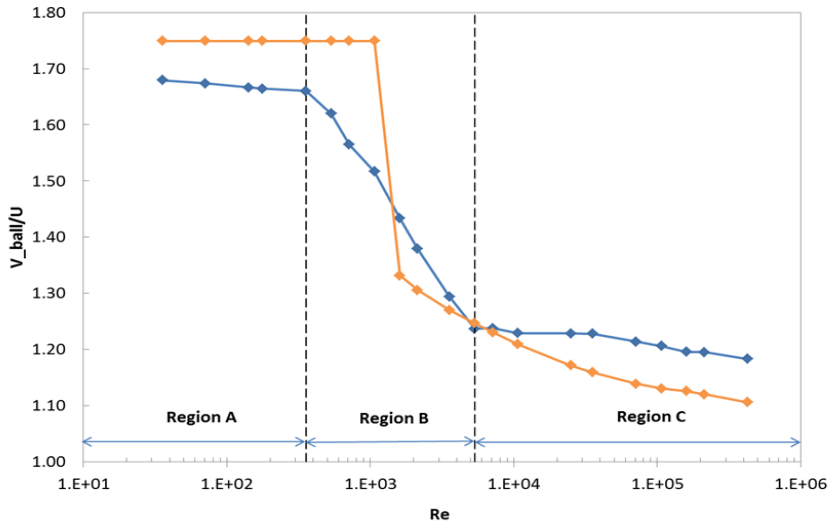

Figure 4.8: Comparison of the pig terminal velocity and of the integrated fluid velocity occupied by the frontal area of the pig (both the pig velocity and the fluid velocity are normalized by the incoming bulk fluid velocity)

Four points in different regions shown in figure 4.7 are selected for further study. They are the

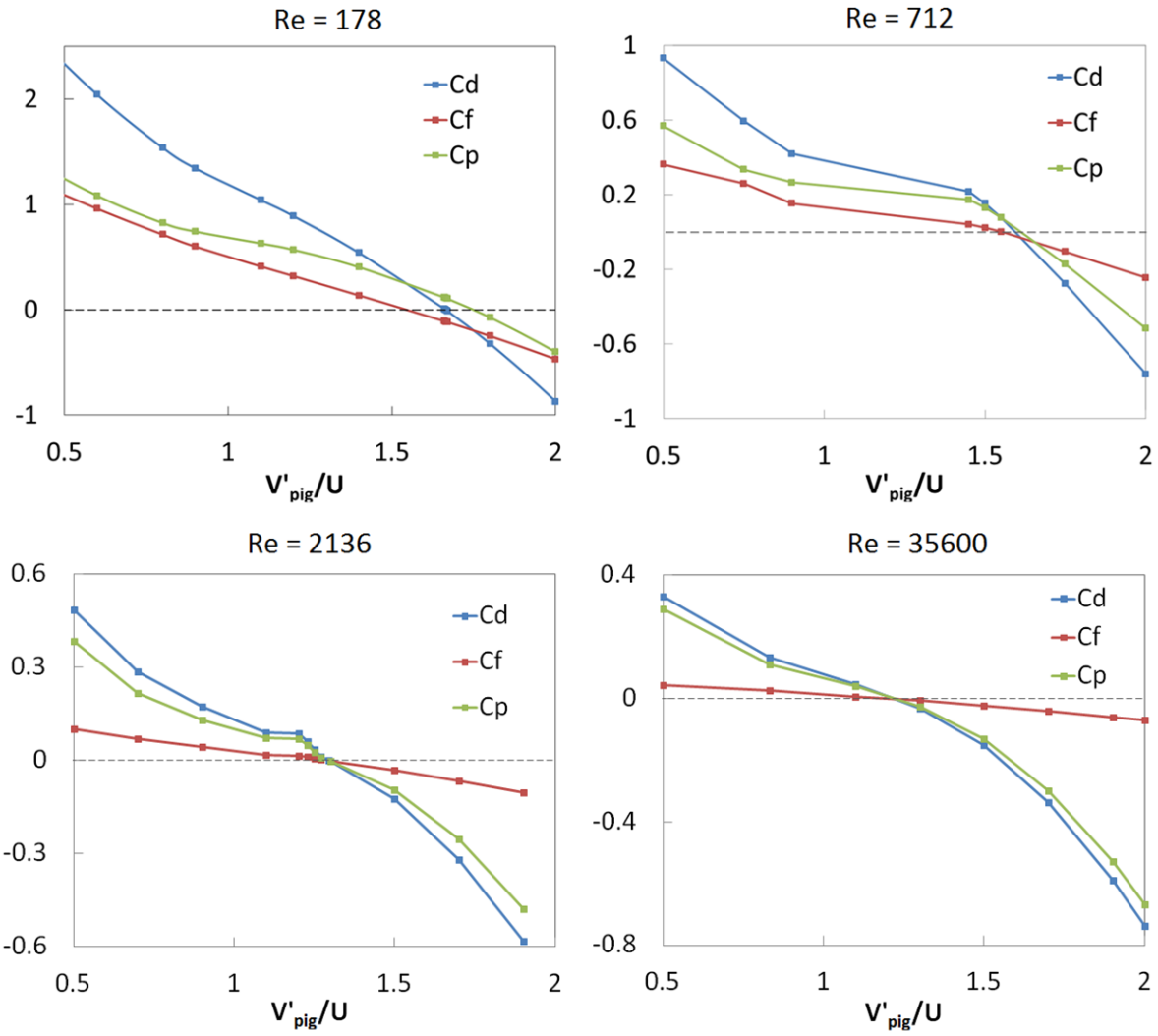

Figure 4.9: Detailed forces on the pig at various Reynolds numbers

flows at Re = 178 in region A, at Re= 712 and Re = 3560 in region B and at Re = 10680 in region C. In Figure 4.9, the detailed forces for various pig velocities at the four values of Re are shown. The normalized pig velocity varies between 0.5 to 2, which includes the state in which the pig is experiencing positive, negative and zero drag forces. It can be seen that when Re is increased, the overall drag coefficient and its components of the pressure drag and the viscous drag are all decreasing. The profiles of the pressure drag and viscous drag at Re = 178 show that the change of the pressure drag is largely affected by the trend in the viscous drag curve. This indicates that the flow around the ball pig at this Reynolds number is mainly affected by the viscous shear force. Therefore the motion of the pig in this region is also dominated by the viscous shear force. When Reynolds number is increased to region B, the viscous drag curve is no longer leading the pressure drag coefficient curve. When Re is 712, the viscous drag is still a major composition in the pressure drag. When Re is increased to 2136, there is a significant difference between the value of the pressure drag coefficient and the viscous drag coefficient. Apparently, the viscous drag coefficient is no longer the major term to affect the curve of the pressure drag coefficient. This means that the inertia force start playing a role in region B and its influence on the flow motion is getting more and more important as Re increases. When Re is further increased to region C, the value of the viscous drag is so small that the pressure drag curve is not affected by the viscous drag at all. The flow is completely dominated by the inertia force. The analysis as given above shows that the driving factor of the flow motion in the three regions in Figure 4.7 is different. In region A, the flow motion is dominated by the viscous shear force and

the pressure generated in the wake is scaled with the viscous shear force. In region B, the viscous shear force and the inertia force are both affecting the flow motion. The influence of the viscous shear force decreases and that of the inertia force increases when Re increases. The flow enters the region C after this transition region. In region C, the flow is completely dominated by the inertia force and the pressure force will be scaling with the inertia force.

The detailed flow field around the pig, when it is in the equilibrium state is also an area of interest. Therefore the streamlines of the flow domain when the ball pig moves with its terminal velocity at the four Re values are shown in Figure 4.10. The streamline patterns can contain so-called critical points, which is either a saddle or a centre. When the pig is in the equilibrium state, the topology of the streamlines is a saddle with two centres at each side of the pig. The distance between the location of the upstream centre and the pig is longer than the distance between the downstream centre and the pig. Both these two centres get closer and closer to the pig when Re increases.

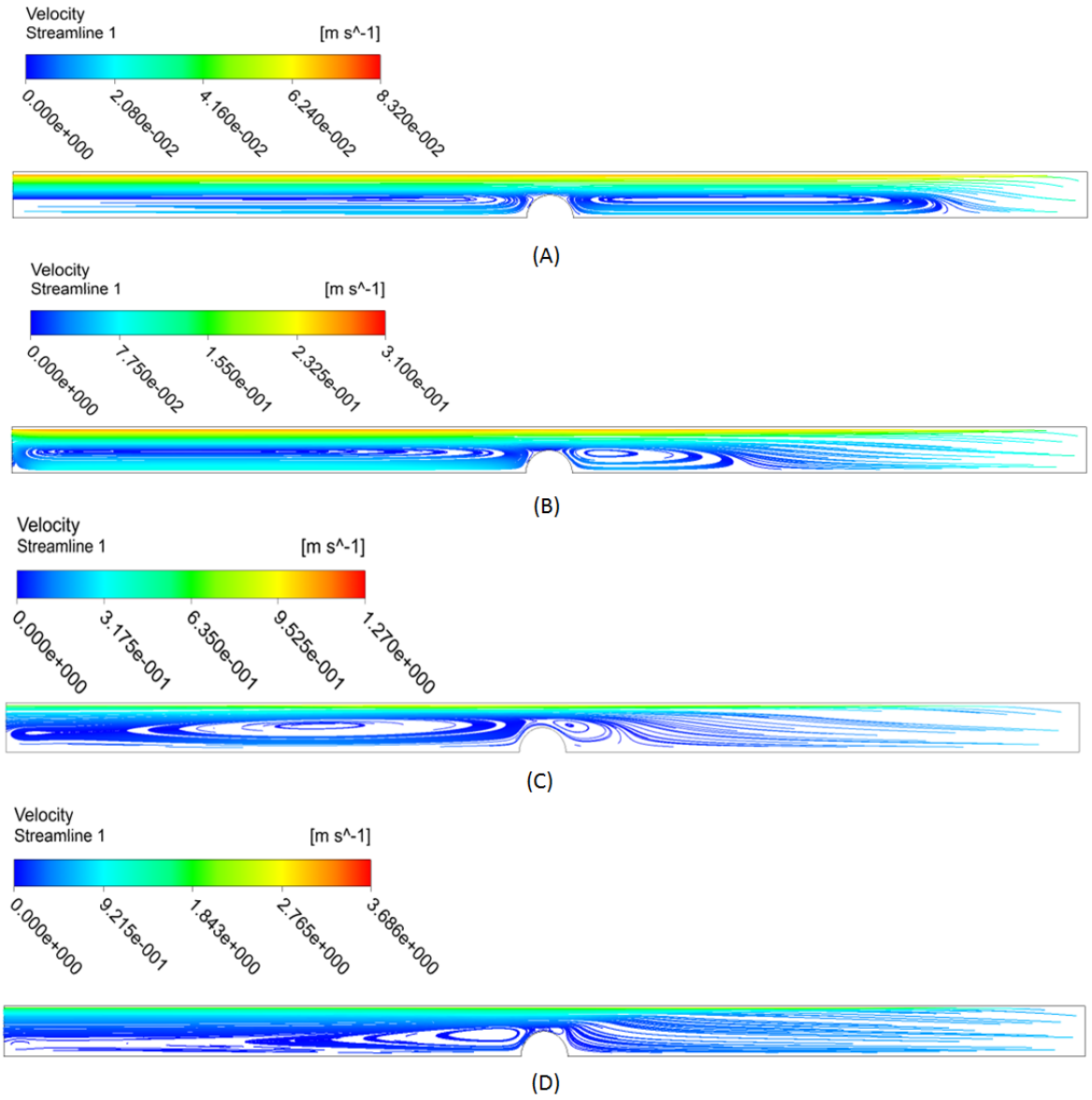

Figure 4.10: Streamlines through the pipe at various Reynolds numbers A) 178; B) 712; C) 2136; D) 35600

Since the pig experiences a positive pressure force in the equilibrium state, there exist a wake down-

stream of the ball pig. To further check the flow in the boundary layer, the separation angle at various Reynolds numbers is also checked. It can be seen from Figure 4.10 that when the centre approaches the pig for increasing Re, the separation angle between the surface of the ball pig and the wake increases. The computed separation angles of the flow at several Reynolds numbers in the three regions are listed in Table 4.5. The separation angle is in the range between 35° to 50° in region A of Figure 4.7. It then continuously increases when Re increases in region B and reaches a value of around 80°. In region C, the separation angle first approaches 90° and eventually the circulation downstream of the pig is shifted in the upstream direction, which leads to an increase of the separation angle to around 110°. This indicates that even when Re is in region C where the flow in the pipe is highly turbulent, the flow in the boundary layer at the surface of the pig is still very laminar in the studied Reynolds number range.

Table 4.5: Separation angle at various Reynolds numbers

Region	Re	Separation Angle (°)
A	71	39.14
	178	42.32
B	712	61.28
	3560	80.22
C	10680	88.29

4.5. Leakage Profile

Since the function of the pig is to drive part of the fluid out of the pipeline, leakage is another important quantity of interest for the oil and gas industry. In this simulation study, the leakage is defined as the percentage of the part of total incoming fluid that moves slower than the pig.

$$leakage = \frac{\dot{Q}_{leakage}}{\dot{Q}_{in}} \tag{4.7}$$

Where $\dot{Q}_{leakage}$ is the mass flow rate of the fluid for which the velocity is lower than the pig velocity along the vertical centre line of the pig. $\dot{Q}_{in}$ is the mass flow rate of the incoming fluid. Based on this definition, the value of the leakage should be between 0 and 1. The incoming flow comprises the leakage part and the by-passing part. Therefore, the sum of the leakage part and of the by-passing part should always be 1. For extreme cases, the leakage should be 0 when the pig is stagnant and it should be 1 when the pig is fully sealed or when the pig moves with a velocity higher than the maximum value of the incoming flow. Figure 4.11 shows the leakage at various normalized pig velocities for Re=178. It can be seen that the leakage increases from 0 to 1 when the normalized pig velocity is increased from 0 to $2U$ which is the maximum fluid velocity in the laminar regime. This indicates that the leakage is properly defined here.

Given the definition of the leakage, it can also be calculated in a simpler way. Since the mass is conserved, the part of leakage can be quantified by $A \times (V_{pig} - U)$ and the incoming fluid can be calculated by $A \times U$. Therefore, the leakage can also be calculated by:

$$Leakage = \frac{V_{pig} - U}{U} = \frac{V_{pig}}{U} - 1 \tag{4.8}$$

Figure 4.12 shows the profile of the leakage with respect to Re. Both the results calculated by using Equation 4.8 and the data obtained from the numerical integration at zero drag condition are shown. As expected, those two profiles are overlapping except for some slight deviations. The latter

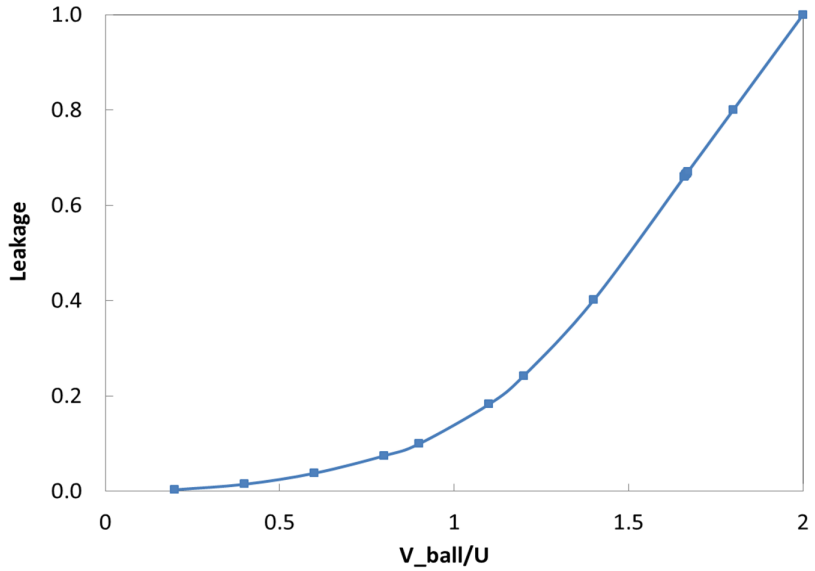

Figure 4.11: Leakage profile with various pig velocities at Re = 178

are present because the final value of the terminal velocity is obtained by interpolation. It can be seen that the leakage is quite high when Re is smaller than 356. It decreases dramatically from around 0.68 to 0.2 when Re is increased from 356 to around 5000. Then it remains at around 0.2 when Re is larger than 5000.

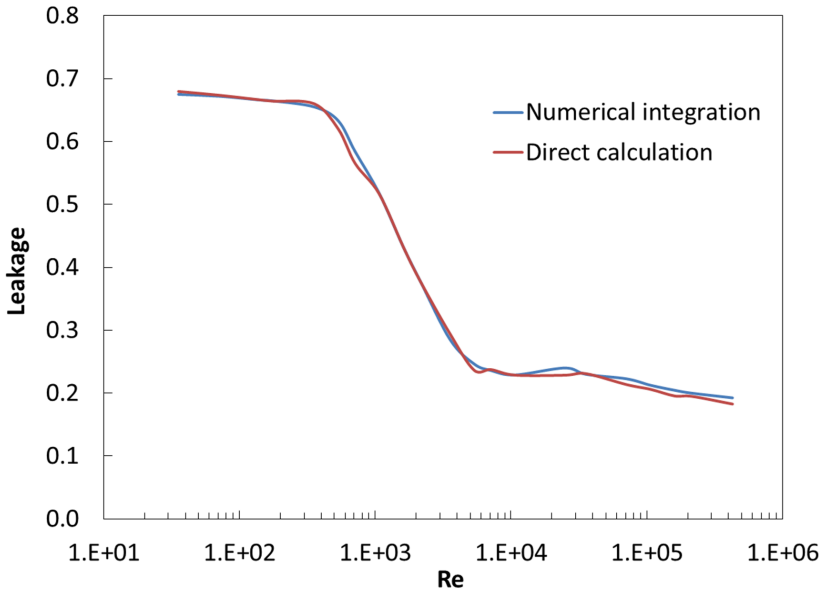

Figure 4.12: Comparison of the leakage profile obtained by the direct calculation from the terminal velocity and by numerical integration of the part of the fluid that is moving slower than the pig at various Reynolds numbers

5

Geometry Variation

The dimension analysis in Chapter 2 has shown that the normalized pig terminal velocity is a function of the Reynolds number and of the ratio of the pig diameter and the pipe diameter. The influence of the Reynolds number has been studied in the previous chapter. This chapter will focus on the simulation of the flow around pigs with various diameters and it will thus study the influence of the diameter change on the motion of the pig. Then the location of the pig will be moved from the centre to the bottom of the pipe and the influence of this location change will be studied.

5.1. Influence of the Pig Diameter on the Motion of the Pig

5.1.1. Numerical Setup and Mesh Details

For the simulations in this part of the study, only the diameter of the pig is varied. The flow domain and geometry parameters have remained the same as those used in Chapter 4. The meshes in this chapter are refined at the largest Reynolds number to satisfy the requirements for the turbulence model. This mesh is then used for the simulation at all the Reynolds numbers. Details of the meshes that have been used for the simulations at each pig diameter ratio are listed in Table 5.1. The parameters in the turbulence model and the numerical setups have also remained the same as those that have been used in Chapter 4.

Table 5.1: Mesh details at various diameter ratios

Diameter ratio	Mesh number
0.3	391,973
0.7	550,573
0.9	536,253
0.95	671,753

5.1.2. Terminal Velocity Profile at Various Diameter Ratios

Figure 5.1 shows the computed terminal pig velocity profile at various pig diameter ratios when Re is varied from 36 to 4.15E5. It can be seen from the figure that when the pig diameter increases, the overall pig terminal velocity decreases. Besides this, the pig terminal velocities at various diameter ratios have similar profiles. When Re increases, the simulations for all diameter ratios experience three stages as has been discussed in Chapter 4 when the diameter ratio was 0.5. Although the Reynolds number range corresponding to the three regions is slightly different when the diameter ratio changes, the overall change in the profile and the characteristics in the three regions can still be observed. At the same time, the terminal pig velocity profiles also show some major differences. At smaller diameter ratios, differences between the normalized pig terminal velocity in the laminar and turbulent flow regimes are quite large. The profiles experience a very sharp decrease in the transition stage

in Region B. As the diameter ratio increases, the difference in the normalized pig terminal velocity between the laminar and turbulent flow regimes decreases. It can be seen from the figure that when the diameter ratio is 0.95, the difference in the terminal pig velocity in the laminar and turbulence flow regimes is so small that the terminal pig velocity profile against Re is almost flat.

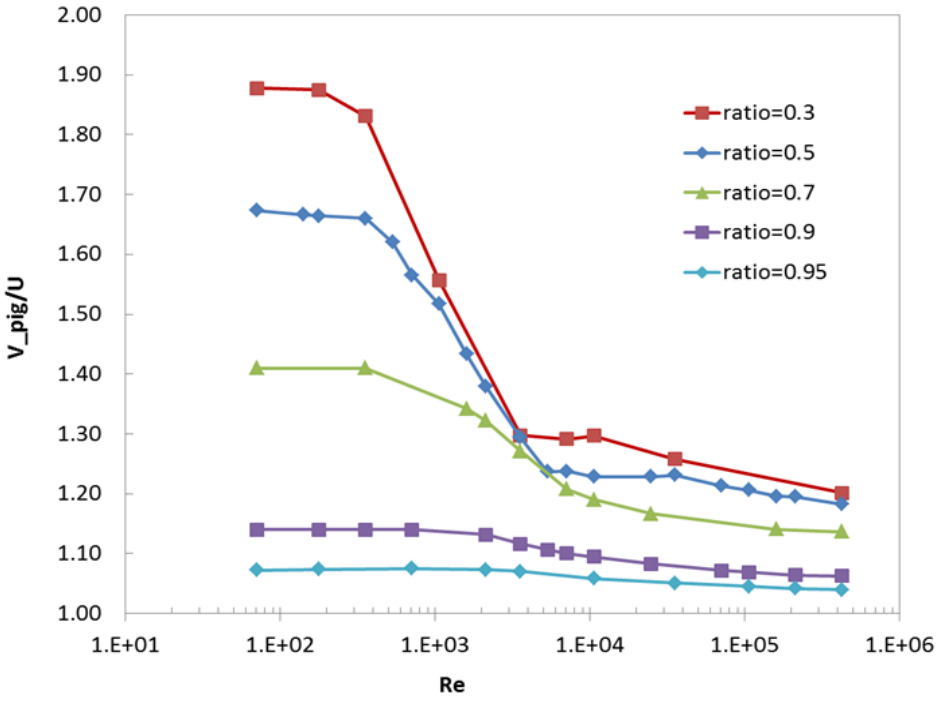

Figure 5.1: The normalized terminal pig velocity against Re at various diameter ratios

Recalling Equation 2.22, the dimension analysis shows that the normalized pig terminal velocity is a function of Re and of the diameter ratio. Now the profiles of the normalized terminal pig velocity profile against Re at various diameter ratios are obtained. An explicit expression of the function is ready to be generated. The force analysis shows that the driving factor for the motion of the pig in the laminar and turbulent flow regimes is different. Because of this difference, the profiles of the terminal pig velocity against the diameter ratio in the laminar and turbulent flow regimes are expected to be different. It can also be seen from Figure 5.1 that when the Reynolds number is in Region A (Re < 300), the normalized pig terminal velocity at each diameter ratio remains almost constant. The profile also stays in a very stable range when Re is in Region C (Re > 10000). This indicates a simpler relationship between the terminal pig velocity and the diameter ratio. To find this relationship, the profile of the normalized pig terminal velocity against the diameter ratio at several Reynolds numbers is studied below.

Pig Terminal Velocity Profile as a Function of Diameter Ratio in Laminar Regime (Re < 300)

When Re in the pipe is smaller than 300, the flow is laminar; therefore, this region is called the laminar flow regime here. The simulation results in this region shows that the normalized pig terminal velocity at a given diameter ratio is almost a constant. Therefore, the normalized pig terminal velocity in this region is only a function of the diameter ratio. Figure 5.2 shows the normalized terminal pig velocity against the diameter ratio, which is varied from 0.3 to 0.95 in this region. It can be seen that the profile lies nicely on a second-order polynomial with the following expression:

$$\frac{V_{pig}}{U} = -0.63(\frac{d}{D})^2 - 0.37(\frac{d}{D}) + 2.00, \tag{5.1}$$

For the motion of the pig along the pipe axis in the laminar flow regime, the maximum velocity that the pig can reach is $2U$ when the diameter of pig approaches 0. This is because the fluid velocity reaches its maximum value of $2U$ along the axis of the pipe. On the other hand, the minimum velocity of the pig will be the same as the bulk velocity when the pig is fully sealed and has the same diameter

as the pipe. From Equation 5.1, it can be seen that the value of V_{pig}/U is 2 at $d/D = 0$ and it is 1 at $d/D = 1$. This shows that although Equation 5.1 is obtained from a limited data set, the results obtained from it are quite reasonable. The check of the curve at two extreme cases is also shown in Figure 5.2 by a dashed line.

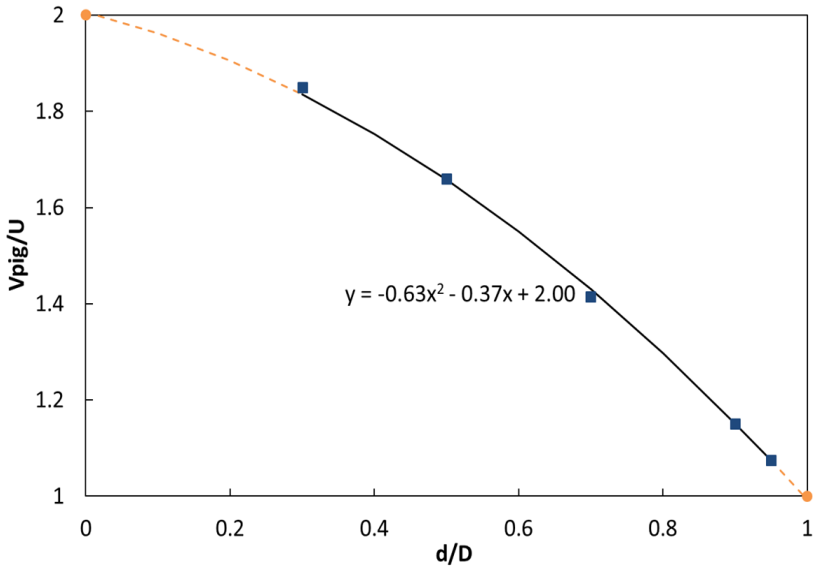

Figure 5.2: The normalized pig terminal velocity against the diameter ratio in the laminar regime

Pig Terminal Velocity Profile as a Function of Diameter Ratio in Turbulent Regime (Re > 10000)

Figure 5.1 shows that the normalized pig terminal velocity in the region where Re > 10000 also remains in a very stable range. Compared with the flow in the laminar flow regime, where the normalized terminal pig velocity is constant at each diameter ratio, the profile of the normalized terminal pig velocities in this region shows a slight decrease when Re increases. The profiles of the normalized pig terminal velocity against the diameter ratio at several Reynolds numbers are shown in Figure 5.3. The figure shows that the profiles of the normalized terminal pig velocity against the diameter ratio are also lying on second order polynomials. Therefore, the profile in the turbulent flow regime also has the following form:

$$\frac{V_{pig}}{U} = a(\frac{d}{D})^2 + b(\frac{d}{D}) + c \tag{5.2}$$

where a, b, and c are constants at different Reynolds numbers. Values of these three constants at the four Reynolds numbers shown in Figure 5.3 and are listed in Table 5.2.

Table 5.2: Values of the constants in Equation 5.2 at various Reynolds numbers

Reynolds number	Constants		
	a	b	c
10680	-0.39	0.13	1.28
35599	-0.44	0.21	1.23
106796	-0.36	0.15	1.22
427182	-0.40	0.25	1.16

The values of the normalized pig terminal velocity with a diameter ratio of 1 at those four Reynolds number, as calculated with Equation 5.2, are 1.02, 1, 1.01 and 1.01, respectively. These values are

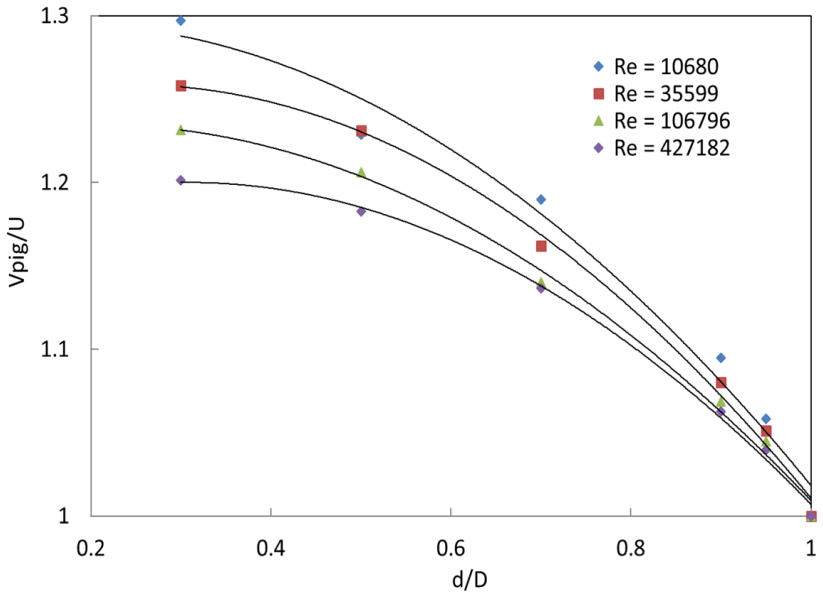

Figure 5.3: The normalized pig terminal velocity against the diameter ratio in the turbulent flow regime

very close to the expected value of 1 when the pig is fully sealed. This thus shows that the expression obtained from the Equation 5.2 is reasonable.

As has been described in Chapter 4, once the terminal velocity profile is obtained, the leakage profile can be directly calculated by combing Equation 4.8 and the terminal pig velocity Equation 5.1. The computed leakage profiles with various diameter ratios when Re increases from 76 to 4e5 are shown in Figure 5.4. Apparently, the leakage percentage decreases when the pig diameter ratio increases and this can be as low as around 10% when the diameter ratio reaches 0.9 or above. Since the purpose of using the ball pig is to remove fluid from the pipe, a low leakage percentage is preferred.

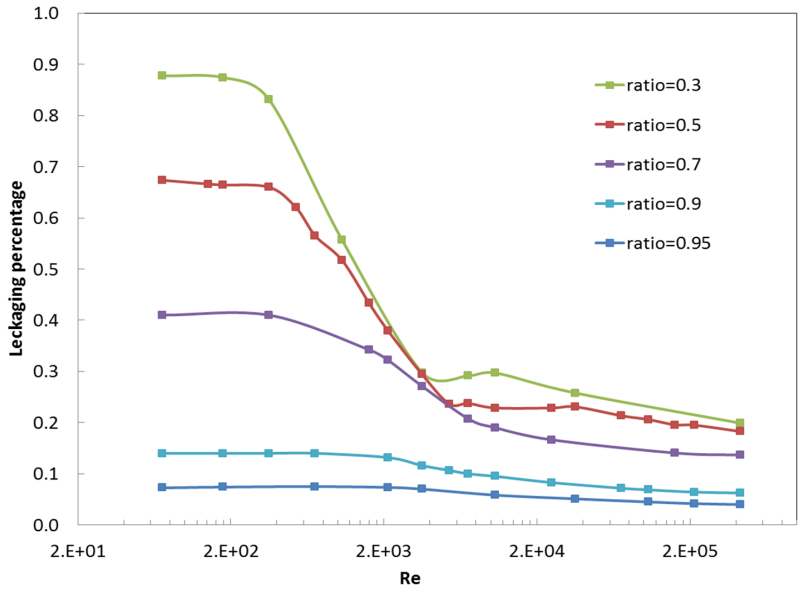

Figure 5.4: The leakage profile against Re at various diameter ratios

5.1.3. Discussion of the Flow Field at Large Diameter Ratios

The leakage profile at various diameter ratios shows that the larger diameter ratios are preferred in the application of the undersized ball pig since it produces a smaller leakage. Therefore, this section will study the detailed flow field information at a diameter ratio of 0.9.

Laminar Flow Regime

We make an observation from the pig's frame of reference, since this makes that the pig remains stationary (while the wall moves with a negative pig velocity). The flow between the pig and the pipe wall can be seen as a wall-driven flow. At the same time, since there is a relative motion between the incoming fluid and the pig, the pressure gradient in the x direction is non-zero. Therefore, the flow between the pig and the pipe wall is a wall-driven flow with a pressure gradient. For this type of wall-driven flow with non-zero pressure gradient between two parallel plates, the Navier-Stokes equations can be largely simplified by assuming that the flow is fully developed. The solution is a parabola in the laminar flow regime, which can be obtained by applying the no slip boundary condition at the two plate boundaries. When the upper plates moves with constant velocity V and a constant pressure gradient (dp/dx) is maintained along the direction of the flow (as shown in Figure 5.5, an analytical solution of the Navier-Stokes equations can be obtained:

$$u = V(\frac{y}{b}) + (\frac{1}{2\mu})(\frac{dp}{dx})(y^2 - by) \tag{5.3}$$

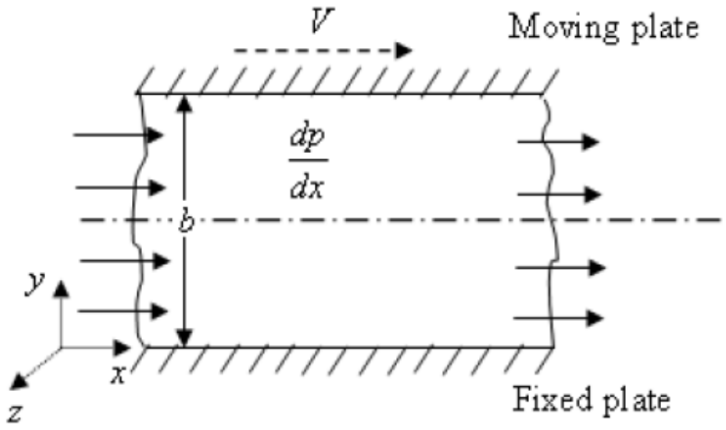

Figure 5.5: Schematic representation of a combined Couette-Poiseuille flow between parallel plates

The actual velocity profile depends on the dimensionless parameter:

$$P = (-\frac{b^2}{2\mu V})(\frac{dp}{dx}) \tag{5.4}$$

Typical velocity profiles at different values of the parameter P are shown in Figure 5.6. The flow velocity profile is linear when the pressure gradient is zero. When the pressure gradient is positive, the value of P will be negative and the flow is referred to as back flow.

In the case of flow between the pipe wall and the pig, because the surface of the pig is curved, the fully developed flow condition cannot be assumed and it is not possible to obtain an analytical solution. At large diameter ratios, however, the gap between the pipe wall and the pig is very narrow and the curvature of the pig is very small (as shown in Figure 5.7). For the part of the fluid moving in the gap with height of H_f, which is much smaller than the curvature diameter, it is reasonable to assume that the fluid velocity profile in the x direction is parallel. The fluid velocity profile between the pig and the pipe wall in the y direction is expected to have the same shape as the combined Couette and Poiseuille flow. In this case, the value of P in Equation 5.4 is negative since V and (dp/dx) are both negative. Therefore, the flow type is also expected to be back flow.

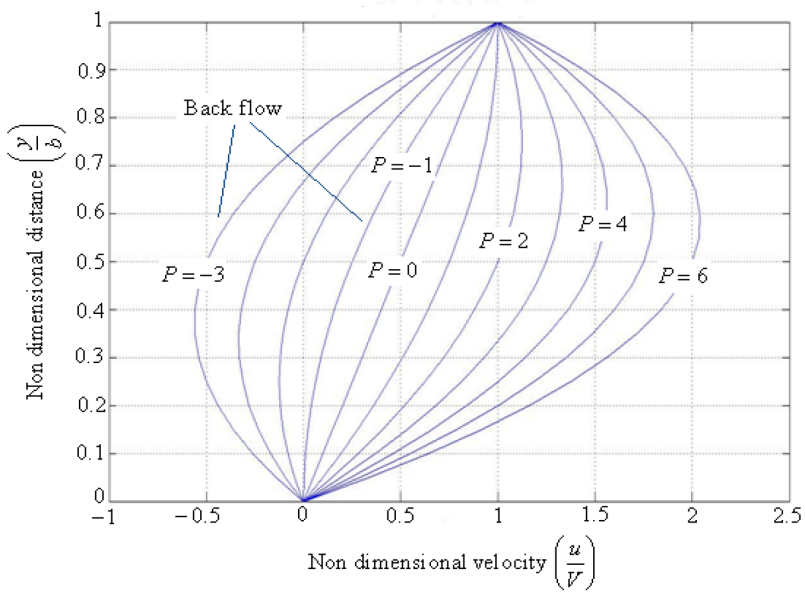

Figure 5.6: Velocity profile for a combined Couette-Poiseuille flow between parallel plates

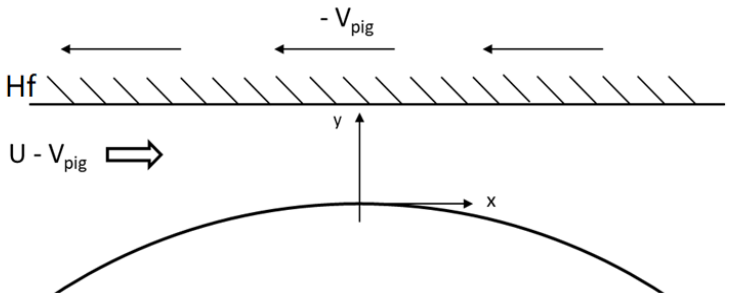

Figure 5.7: Sketch of the flow domain between the pig and the pipe wall

Figure 5.8 shows the velocity profile between the pig and the pipe wall in the y direction at different Reynolds numbers in the laminar regime. It can be seen that the profile is also a parabola with a reverse flow type. Since the pipe wall moves with negative velocity, the back flow profile is flipped. It also shows that the velocity profiles at different Reynolds numbers are overlapping. This means that the value of P remains a constant at different Reynolds numbers. This gives a good indication that the flow between the pig and the pipe wall behaves as a combined Couette and Poiseuille flow. Therefore, the general velocity profile of a combined Couette and Poiseuille flow can be used to describe the flow between the pig and the pipe wall:

$$u = V_{pig}\left(\frac{y}{H_f}\right) + \left(\frac{1}{2\mu}\right)\left(\frac{dp}{dx}\right)(y^2 - H_f y) \tag{5.5}$$

Where H_f is the film height, which is equal to $(D-d)/2$. Given this explicit expression, the average fluid velocity in the film can be calculated by integrating the axial fluid velocity along the y axis and by dividing the result with H_f. In this way the following expression for the average fluid velocity u_f can be obtained:

$$\frac{u_f}{V_{pig}} = 0.5 + \frac{1}{6}V_{pig}P \tag{5.6}$$

Since V_{pig} and P are both negative, the value of u_f/V_{pig} in the laminar flow regime is expected to be larger than 0.5.

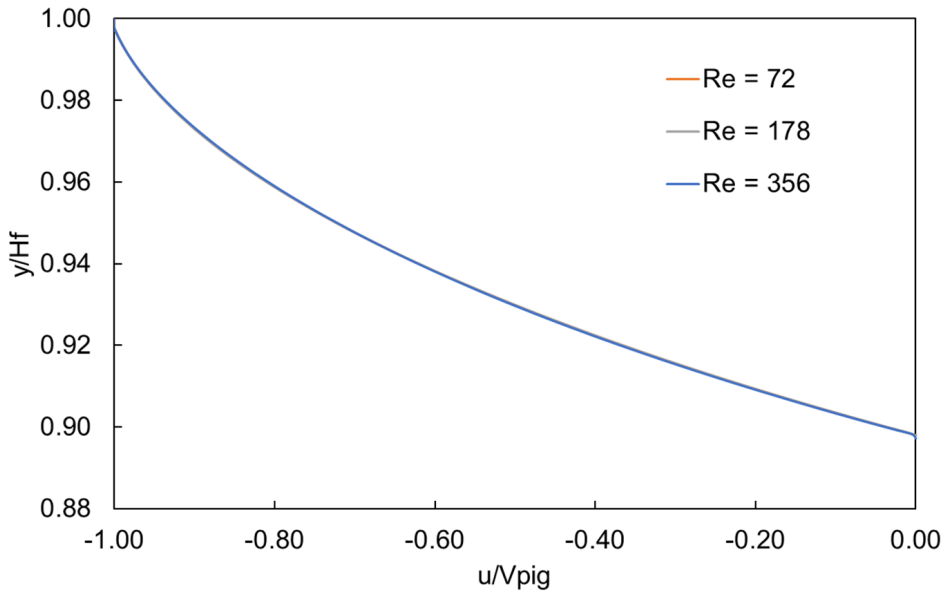

Figure 5.8: Velocity profile of the flow between the pig and the pipe wall at different Reynolds numbers in the laminar regime

To check this, the profile of u_f/V_{pig} in the laminar regime at several Reynolds numbers is depicted in Figure 5.9. It can be seen that all the values of u_f/V_{pig} are around 0.645 at various Reynolds numbers in the laminar flow regime. Therefore, it can be concluded here that the average fluid velocity in the film is larger than $V_{pig}/2$. Since the terminal pig velocity is obtained by interpolation, the relationship between u_f/V_{pig} and V_{pig} is not validated here. But from Equation 5.6, it is expected that u_f/V_{pig} and V_{pig} have a linear relationship for a fixed pig diameter since the previous analysis shows that P is a constant at a given diameter ratio.

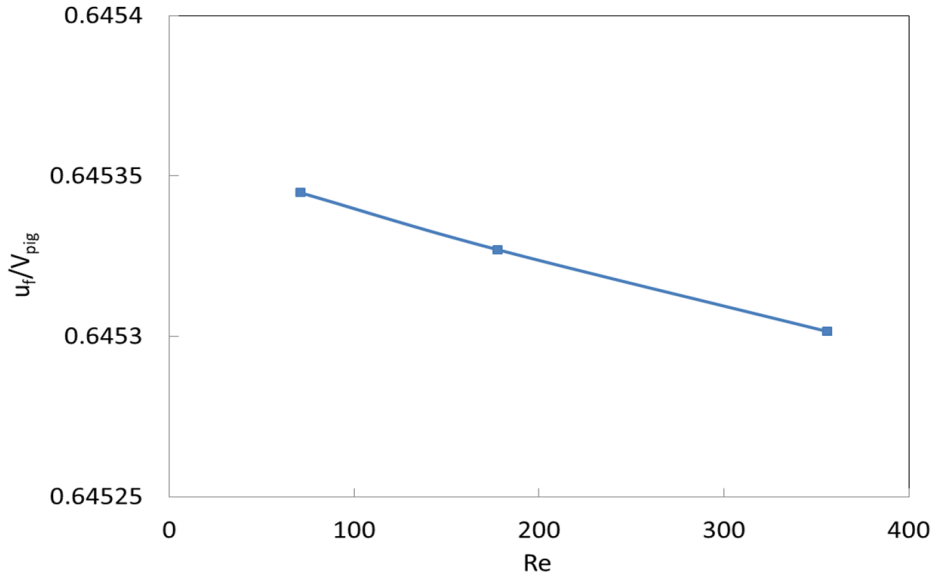

Figure 5.9: Average fluid velocity against Re at d/D = 0.9 in the laminar flow regime

Turbulent Flow Regime

In the turbulent flow regime, the velocity profile will be largely affected by the appearance of the wall since the velocity profile in the near wall region changes rapidly and follows different laws in different layers. It is difficult to obtain an analytical solution for the flow velocity profile. A DNS [19] captured

the mean velocity profile of the turbulent Couette flow at various conditions and it is shown in Figure 5.10. The simulation results show that the flow appears to follow the linear law in the viscous sublayer along the moving wall side. The interval in which the linear law holds is larger along the moving wall side than along the stationary side.

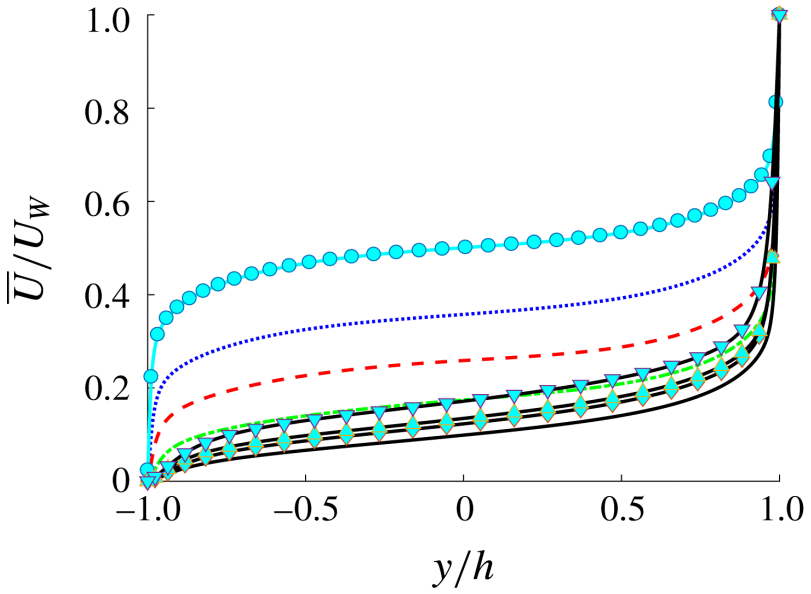

Figure 5.10: Mean velocity profile for turbulent Couette flow between parallel plates, reproduced from [19]

Figure 5.11 shows the fluid mean velocity profile between the pig and the pipe wall at various Reynolds numbers. It can be seen that the velocity profiles have a similar shape as the one of the turbulent Couette flow obtained from the DNS. The linear law holds longer along the moving side than along the stationary side. This comparison further validates that the flow between the pig and the pipe wall at a large diameter ratio in turbulent flow regime also has a Couette flow profile.

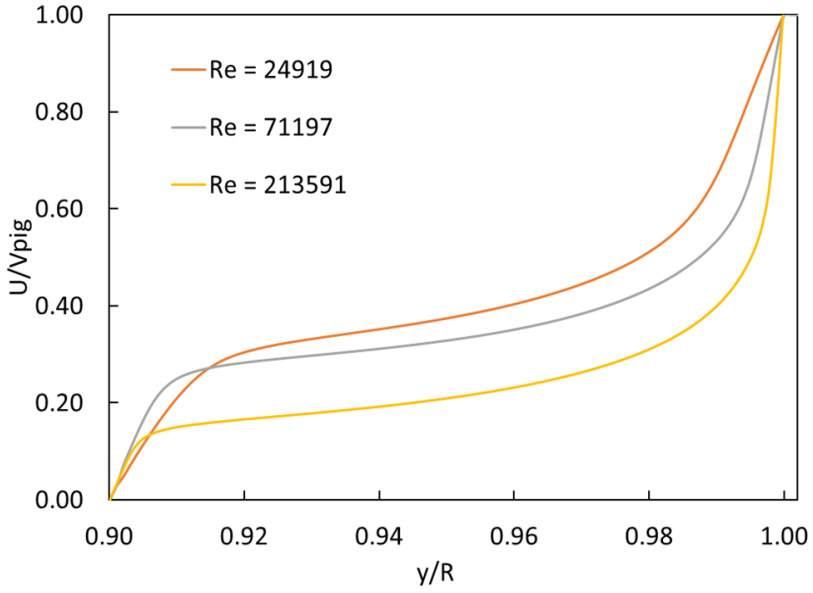

Figure 5.11: Computed mean velocity profile for the flow between the pig and the pipe wall

Figure 5.12 shows the profile of the average fluid velocity in the gap between the pig and the wall u_f/V_{pig} against Re in the turbulent flow regime. It can be seen that when Re increases, the value of

u_f/V_{pig} decreases exponentially. A data regression analysis shows that the values of u_f/V_{pig} and Re in the turbulent flow regime (Re > 2140) have the following relationship:

$$\frac{u_f}{V_{pig}} = 1.625Re^{-0.134} \tag{5.7}$$

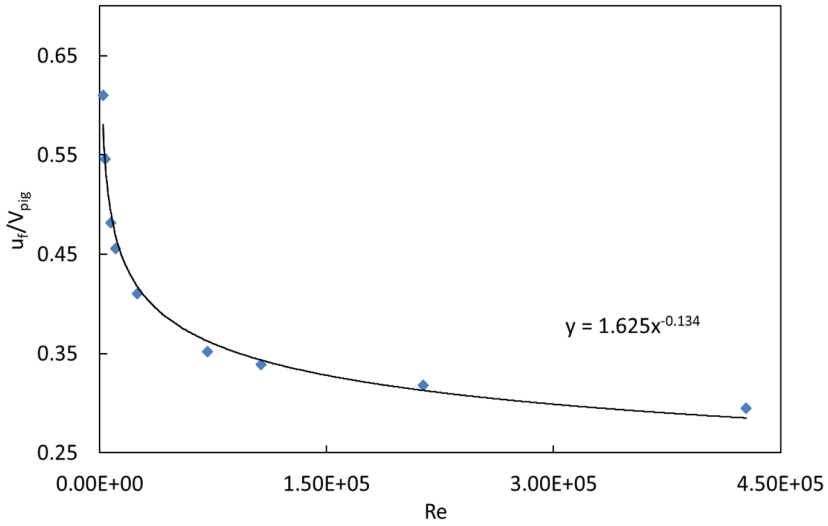

Figure 5.12: Average film velocity between the pig and the pipe wall against Re in the turbulent flow regime

Although the relationship between the average fluid velocity in the gap and the pig velocity is obtained based on a single-phase flow simulation, the obtained expressions of 5.6 and 5.7 can also be directly used for the multiphase flow model. According to OLGA model, the leakage is quantified by using the volumetric flow rate Q_{fl}:

$$Q_{fl} = \frac{\pi(D^2 - d^2)}{4} u_f \tag{5.8}$$

The average film velocity u_f between the pig and the pipe wall is calculated by $V_{pig}/2$, while neglecting the effects of pressure gradient and assuming a laminar flow. However, the simulation results show that both the pressure gradient and the turbulence effect influence the average film velocity significantly. The coefficient of 0.5 is not accurate, neither in the laminar nor in the turbulent flow regime. For laminar flow, depending on the pig terminal velocity, the value of u_f/V_{pig} is larger than 0.5 while in the turbulent flow regime, it is a function of the Reynolds number and decreases exponentially when Re increases.

5.2. Influence of the Pig Location On the Flow Motion

When the pig is moving along the axis of pipe, it is possible to make the axisymmetric assumption and a 2D simulation is reasonable. When the pig is not positioned along the axis of pipe, however, a 3D simulation is necessary. In order to test the influence of the position of the pig in the pipe on the flow motion, the study moved to performing a 3D simulation in this section. The influence of the position of the pig on the flow motion will only be studied at a diameter ratio of 0.9 since this was used in the actual field operation in the F14 pipeline in Sarawak.

5.2.1. Numerical Setup and Mesh Generation

The complexity of the simulation is significantly increased when the study is moved from 2D to 3D. The 2D simulation has shown that a pipe length of $0.3m$ before the pig and a total pipe length of $0.6m$ is sufficient for the flow to develop when a fully developed velocity profile is prescribed at the inlet. The results from the 3D simulation, however, show that the pipe length used in the 2D simulation is not sufficient anymore. Two problems were encountered when the pipe length from 2D simulation was used. First, the reverse flow from the outlet makes the continuity equation very difficult to converge.

Second, the comparison of the velocity profile at different locations upstream of the pig shows that length of $0.3m$ is not sufficient for the flow to develop. Both these two problems are solved by increasing the pipe length to $1.6m$ with $0.8m$ upstream and $0.8m$ downstream of the pig. Therefore, this pipe length will be used for the simulation in this section. The pipe diameter is kept the same as $0.052m$ and the diameter ratio of 0.9 gives a pig diameter of $0.0468m$.

In practice, depending on the density of the pig and of the fluid, the pig could be located at the bottom of the pipe. It is impossible, however, to generate the geometry with the pig completely touching the wall since this will generate a degenerated manifold body. To solve this, a narrow gap is left between the pipe wall and the pig. From a physical point of view, this gap should be as narrow as possible in order to simulate the real flow situation. Numerically, however, this narrow gap will lead to a skewed mesh, which will decrease the mesh quality. Therefore, the height of the gap needs to be carefully chosen. It turns out that an acceptable mesh could be generated when the gap is $6 \times 10^{-4}m$. When the height of the gap is further decreased, the very large skewness of the mesh will result in convergence problem. Therefore, a height of $6 \times 10^{-4}m$ is used for the gap. Figure 5.13 shows the geometry used in the 3D simulation. Simulations with the pig moving at both the centre and bottom of the pipe are performed in this section. Figures 5.13 (B) and (C) show the frontal view of the flow domain with the pig at the centre and and at the bottom of the pipe, respectively.

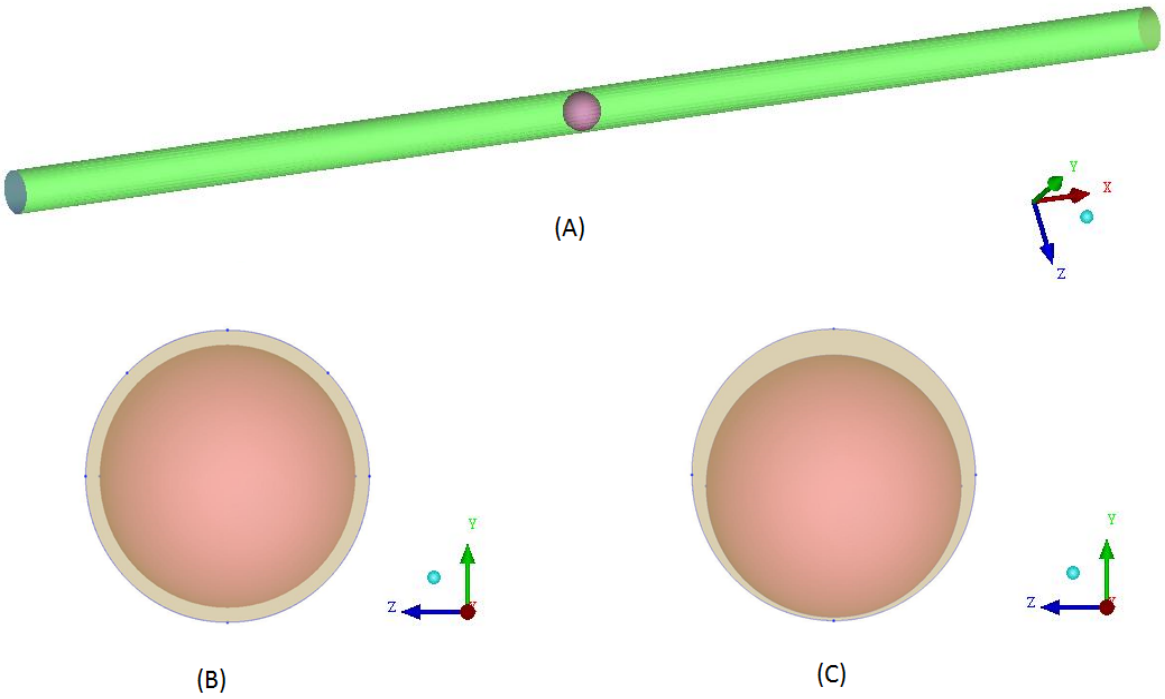

Figure 5.13: Flow domain in the 3D simulation (A) Full view; (B) Frontal view with the pig at the centre of the pipe; (C) Frontal view with the pig at the bottom of the pipe

For this part of the simulation, unstructured meshes are generated since the generation of a structured mesh becomes difficult at such a high diameter ratio, especially when the pig is located at the bottom of the pipe. Since most of the simulations are in the turbulent flow regime, an extra prism layer needs to be generated along the wall region. Due to the same reason as described in Chapter 3 for the 2D turbulent simulation, 15 more prism layers are generated along the pipe wall and around the pig. Besides this, the size of the first node is refined to make sure that the value of $y^+$is smaller than 1. After a mesh sensitivity analysis, 5,857,227 and 4,845,942 grid cells are used for the simulation of the pig moving along the axis and at the bottom of the pipe, respectively. Figure 5.14 shows the mesh details at various critical positions. It can be seen from Figure 5.14 (A) that the mesh sizes around the pig have been very much decreased in order to capture the complex flow around the pig. The extra prism layers along the pipe wall can be seen from the mesh at the inlet as shown in Figure 5.14 (B).

The 3D simulation shows that the flow around the pig in the pipe at the large Reynolds number

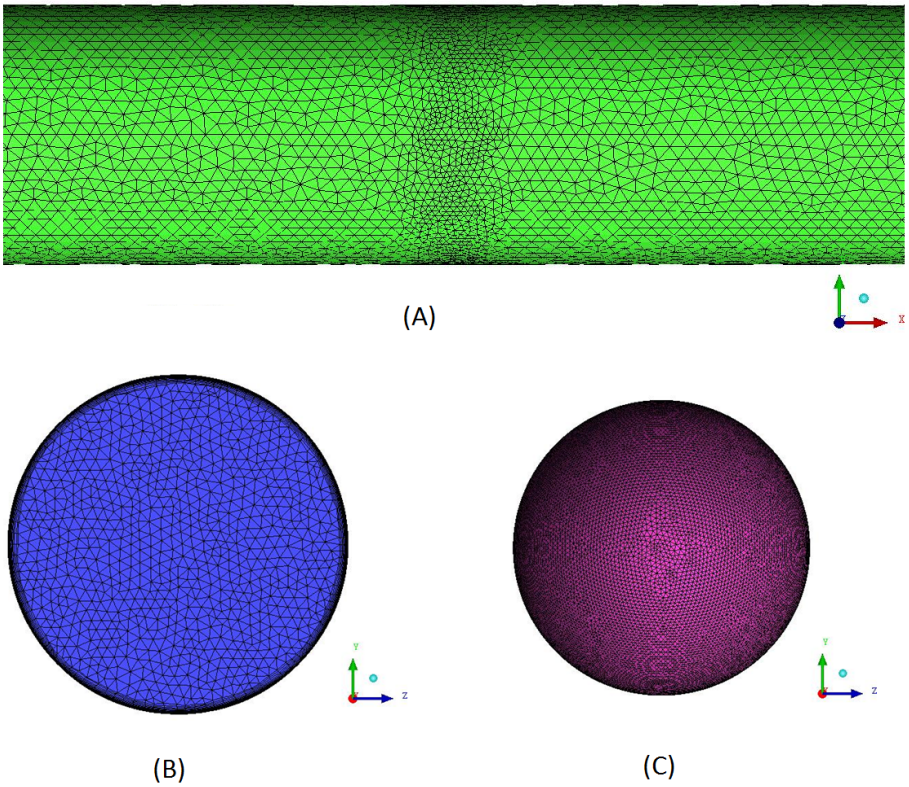

Figure 5.14: 3D Mesh details at different positions (A) At the pipe wall close to the pig; (B) At the inlet of the pipe; (C) Around the pig

is unsteady. For an unsteady simulation, it is important to select the appropriate temporal discretization scheme and the appropriate time step size. In this study, an implicit method is selected for the discretization of the time derivative since compared with the equivalent steady state problem, this gives an unconditional numerical stability of the solution. For the pressure-velocity coupling method, the SIMPLE scheme is selected again. For the spatial discretization, the pressure is discretized with second-order accuracy and the momentum is discretized by using the second-order upwind method. Since the implicit method is used, the size of the time step does not affect the stability of the solution. The time step size only needs to be small enough to generate a step size independent solution. A comparison shows that the results are independent of the time step size when it is smaller than $0.01s$. Therefore, the time step size is set to $0.01s$ during the simulation. At each time step, 200 iterations are used to generate a converged solution.

5.2.2. Comparison Between 2D and 3D Simulations

Since the simulation domain and mesh strategy are changed in the 3D simulation, this section compares the results obtained from the 3D simulation when the pig is positioned at the centre of the pipe with the results of the 2D simulation.

The 3D simulation shows that steady state flow is found when Re is smaller than 365, for the pig at a diameter ratio of 0.9, which moves at the center of the pipe. This is because the steady state solver gives a good convergence. Also, later the unsteady state simulation shows that the drag coefficient eventually converges to a constant. Figure 5.15 shows the results of the normalized terminal pig velocity against Re for both the 2D and 3D simulations when Re is smaller than 365. 2D simulations show that the normalized pig terminal velocity stays at a constant of 1.14 when the Reynolds number is smaller than 712. Therefore, the profile in this range is shown as a straight line in the figure. Compared with the 2D simulation, the 3D simulation is more time consuming, so only a few points are selected for the simulation and the results are shown as dots in the figure. The terminal velocity of the pig is

again found by changing the velocity of the pig and by computing the drag force exerted on the pig. The final results show that the terminal pig velocities found from the 3D simulations are the same as those that were found from the 2D simulations in this Re range. This indicates that the flow in this Re range is in steady state and axisymmetric.

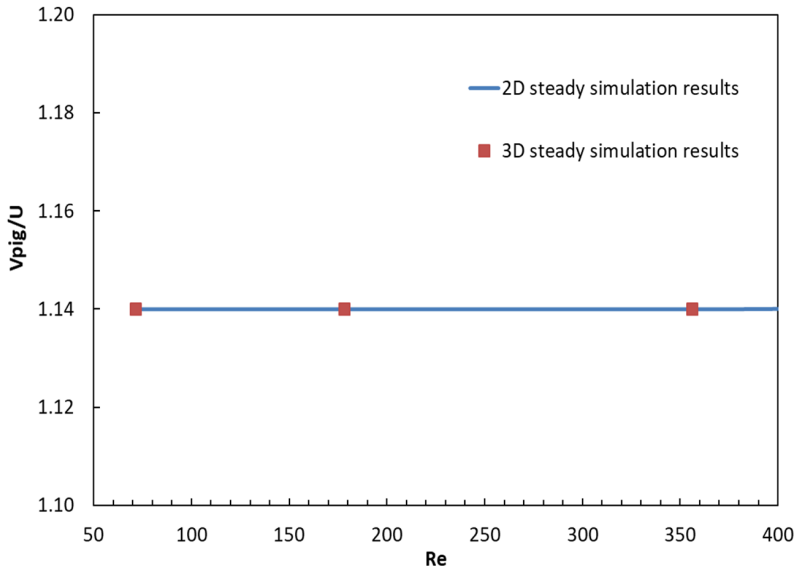

Figure 5.15: Comparison of the computed terminal pig velocity between the 2D and 3D simulations when Re < 365

When the Reynolds number is further increased, the 3D steady state simulation is not converging any more and the profile of the residuals and of the drag coefficient start to fluctuate. This indicates that the flow become unsteady. Therefore, unsteady simulations are performed when the Reynolds number is larger than 365.

Here we will give some more detail on the applied procedure to find the terminal pig velocity, since the profiles of the drag coefficients are not constants anymore. Also, the terminal pig velocity was found by interpolation in a larger range compared with previous simulations due to the long computational time for 3D unsteady state simulation. For example, the incoming fluid velocity is $2m/s$ at Re = 7120. It is found that when the pig velocity is set to $2.2m/s$, the computed drag coefficient profile fluctuates around 0.1195 after about 6 seconds. When the velocity of the pig is increased to $2.3m/s$, however, the value of the drag coefficient becomes negative and it fluctuates at around -0.1946. Although the amplitude of the fluctuation becomes smaller as time passes by, it does not converge to a constant even not after $50s$ of simulation. The profiles of the fluctuating drag coefficient at a pig velocity of $2.2m/s$ and $2.3m/s$ are shown in Figure 5.16. To find the terminal velocity of the pig, a linear relationship between the drag coefficient and the pig velocity in this range is assumed. Since the drag coefficient is fluctuating, the average value is used for the interpolation. After this linear interpolation between $2.2m/s$ and $2.3m/s$, it is found that the zero drag condition occurs when the pig velocity is $2.224m/s$. Therefore, the velocity of $2.224m/s$ will be taken as the terminal velocity of pig, which gives that $V_{pig}/U = 1.112$ at this Re.

The same interpolation process is used to find the terminal velocity of the pig at various Reynolds numbers. Table 5.3 summarizes the velocities of the pig which are used for the interpolation and the interpolated terminal pig velocities at different Reynolds numbers. It can be seen from Table 5.3 that the terminal pig velocity at Re = 2136 is directly found to be $0.68m/s$ since the drag coefficient profile is fluctuating around zero. Drag coefficient profiles at various pig velocities used for the interpolation are shown in Appendix A.

Figure 5.17 shows the normalized terminal pig velocity profile against Re when the Reynolds number is larger than 365. It can be seen that the terminal pig velocities obtained from the unsteady 3D simulations agree quite well with the ones obtained from the 2D steady state simulations. When the

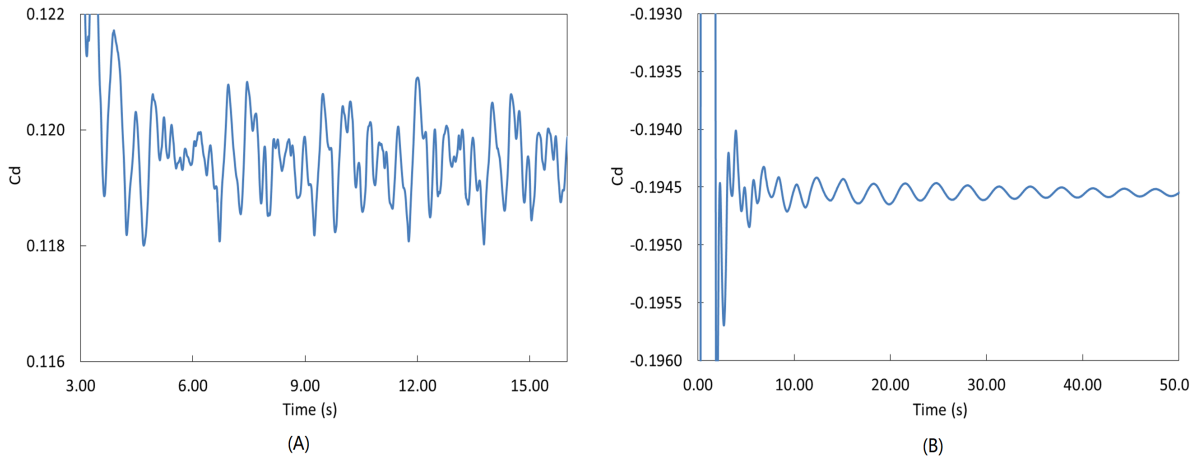

Figure 5.16: Profiles of the computed drag coefficient at Re = 7120 when the pig velocity is: A) $2.2m/s$; B) $2.3m/s$

Table 5.3: Details of the velocity and drag coefficients as used for the interpolation

Re	Fluid velocity (m/s)	Pig velocity (m/s)	Drag coefficient (average)	Terminal pig velocity (m/s)
712	0.2	0.228	0.01862	0.2282
		0.23	-0.1845	
2136	0.6	0.68	0	0.68
7120	2	2.2	0.102	2.24
		2.3	-0.19451	
10680	3	3.3	0.058	3.31
		3.4	-0.295	
24919	7	7.6	0.14356	7.64
		7.7	-0.17451	
71197	20	21	0.1025	21.4
		22	-0.1340	
106796	30	32	0.01286	32.3
		33	-0.0275	

Reynolds number is smaller than 4000, the terminal pig velocities found from the 3D simulations are almost completely overlapping with the ones obtained from the 2D simulations. When Re is increased to 5000, a slight disagreement between 2D and 3D results starts to appear and it can be seen that the terminal velocity obtained from the 3D simulation is slightly larger than the one obtained from the 2D simulation.

This disagreement can be due to two possible reasons. First, since unstructured meshes are generated for the 3D simulation, the quality of the 3D mesh is much lower than that of the 2D mesh. Therefore, the disagreement could be caused by the linearization error in the 3D simulation. Another possibility is that the force exerted on the pig is affected by the essential asymmetry of the flow. To find the reason of the disagreement, the mesh details and the flow field contours are checked.

As has been stated before, the value of y^+ and the discretization resolution in the boundary layer

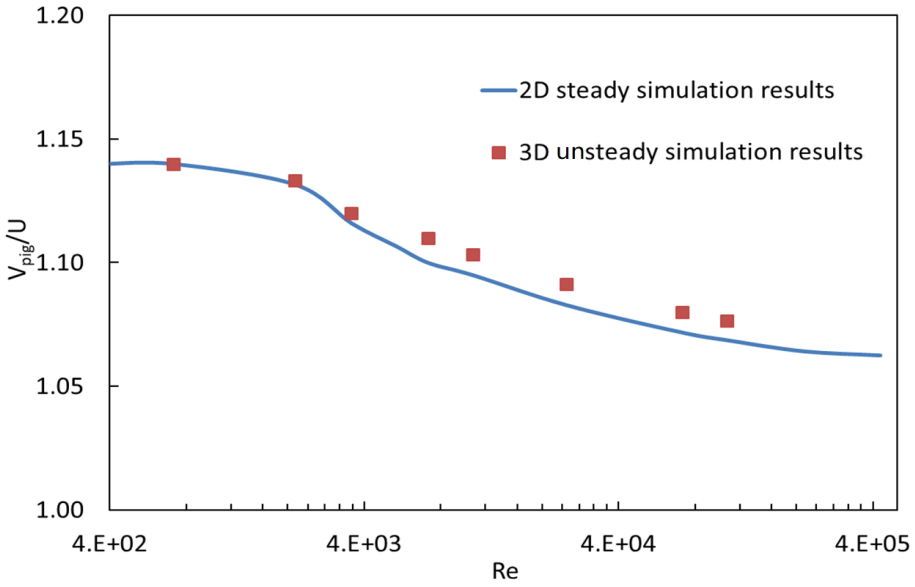

Figure 5.17: Comparison of the pig terminal velocity obtained from the 2D and 3D simulations when Re > 365

are the two quantities of most importance to obtain a high quality turbulent simulation. Figure 5.18 shows the profiles of y^+ along the pipe wall at Re = 106796. It can be seen that the value of y^+ both along the pipe wall and around the pig are smaller than 1. For lower Reynolds numbers, this value is even smaller. Besides this, the simulation results also show that the number of nodes in the boundary layers is larger than 15. This means that the requirements of the turbulence model are well satisfied in the near wall region. Previous studies have shown that the mesh sizes in other regions are less likely to be the reason of the disagreement.

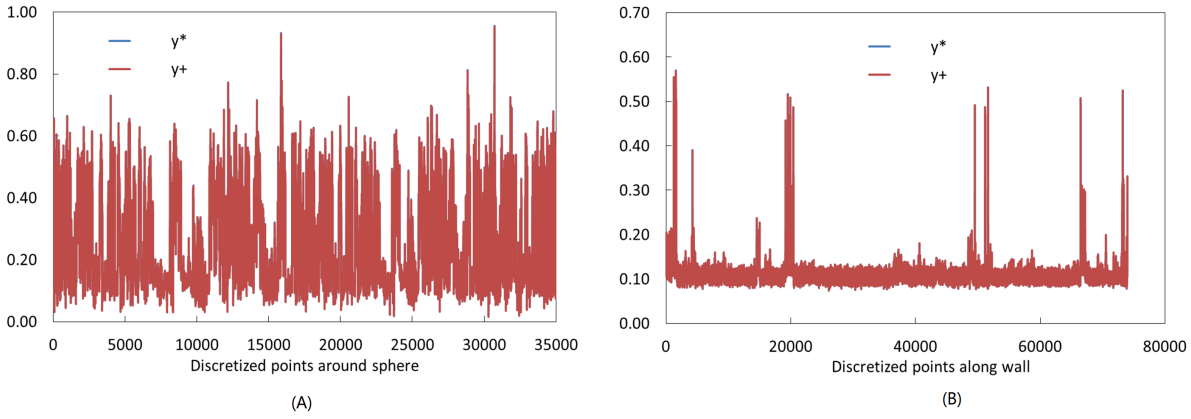

Figure 5.18: Profiles of y^+ around the pig and along the pipe wall at a Reynolds number of 106796

Figure 5.17 shows that the disagreement starts to appear when Re is larger than 4000. To find the actual reason for the disagreement between the 2D and 3D results, the detailed flow field contours at two different Reynolds numbers are examined.

The axial velocity field contours close to the pig at Re = 2136 as obtained from the 2D and 3D simulations at 30 s are shown in Figure 5.19. It can be seen from the 3D simulation results that the flow field upstream of the pig is significantly affected by the presence of the pig. The 2D simulation results, however, show that the flow field upstream of the pig is only slightly affected by the presence of the pig. In fact, the 3D simulation results show that the flow is essentially non-axisymmetric, which makes the velocity field from the 3D simulation different from the one obtained from the 2D simulation. The wake after the pig in the 3D simulation looks quite symmetric.

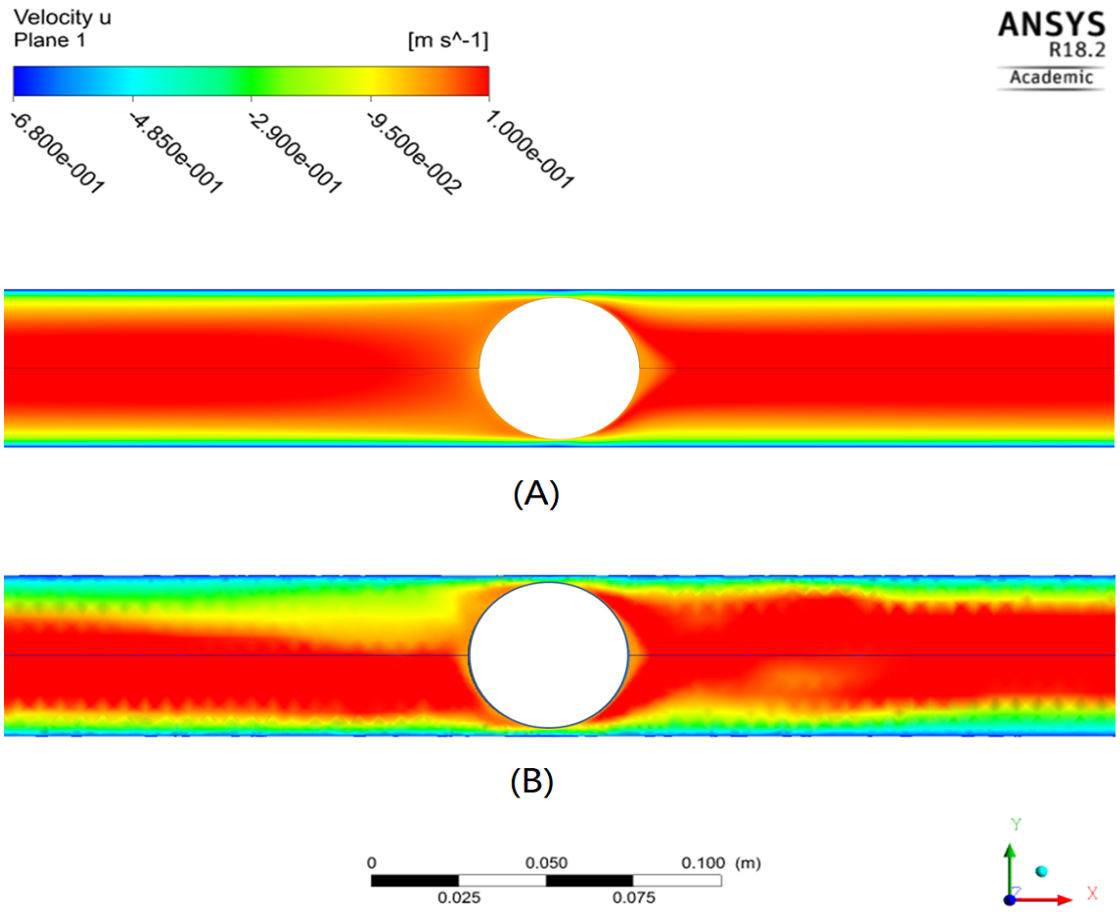

Figure 5.19: Axial velocity field contours around the pig at Re = 2136 from A) 2D simulation; B) 3D simulation (xy plane)

Figure 5.20 shows a similar comparison of the axial velocity field contour close to pig, but now for Re = 71197. The contours of the 3D simulation are taken at 20 s. Both the 2D and 3D simulation results show that the flow upstream of the pig at this large value of the Reynolds number is not much affected by the presence of the pig. However, the velocity field contours downstream of the pig show some major differences. The 2D simulation assumes that the flow is axisymmetric and hence the wake after the pig is also symmetric with respect to the x-axis. The 3D simulation results, however, show that the wake is not at the centre.

The analysis above shows that the terminal pig velocity as obtained from the 2D and 3D simulations are the same at Re = 2136. Here the wake after the pig in both the 2D and 3D simulations is symmetric with respect to the axis of pipe. In contrast to this, the terminal pig velocity obtained from the 3D simulation is slightly higher than the one obtained from the 2D simulation at Re = 71197. Here also the wake after the pig as found in the 2D and 3D simulations shows a difference. Since the pressure force exerted on the pig is very important for the motion of the pig, the successful prediction of the pressure force is largely dependent on the accurate prediction of the wake. It is concluded that the disagreement between the 2D and 3D simulations is due to the essential asymmetric behaviour of flow downstream of the pig. Results obtained from the 2D simulation are not accurate because this cannot properly capture the wake after the pig.

5.2.3. Influence of the Pig Location on the Flow Motion

The comparison between the 2D and 3D simulations when the pig is positioned at the centre of the pipe has shown that the unstructured mesh and discretization methods as used in the 3D simulation are accurate. The same parameters and mesh generation methods will therefore be used to simulate

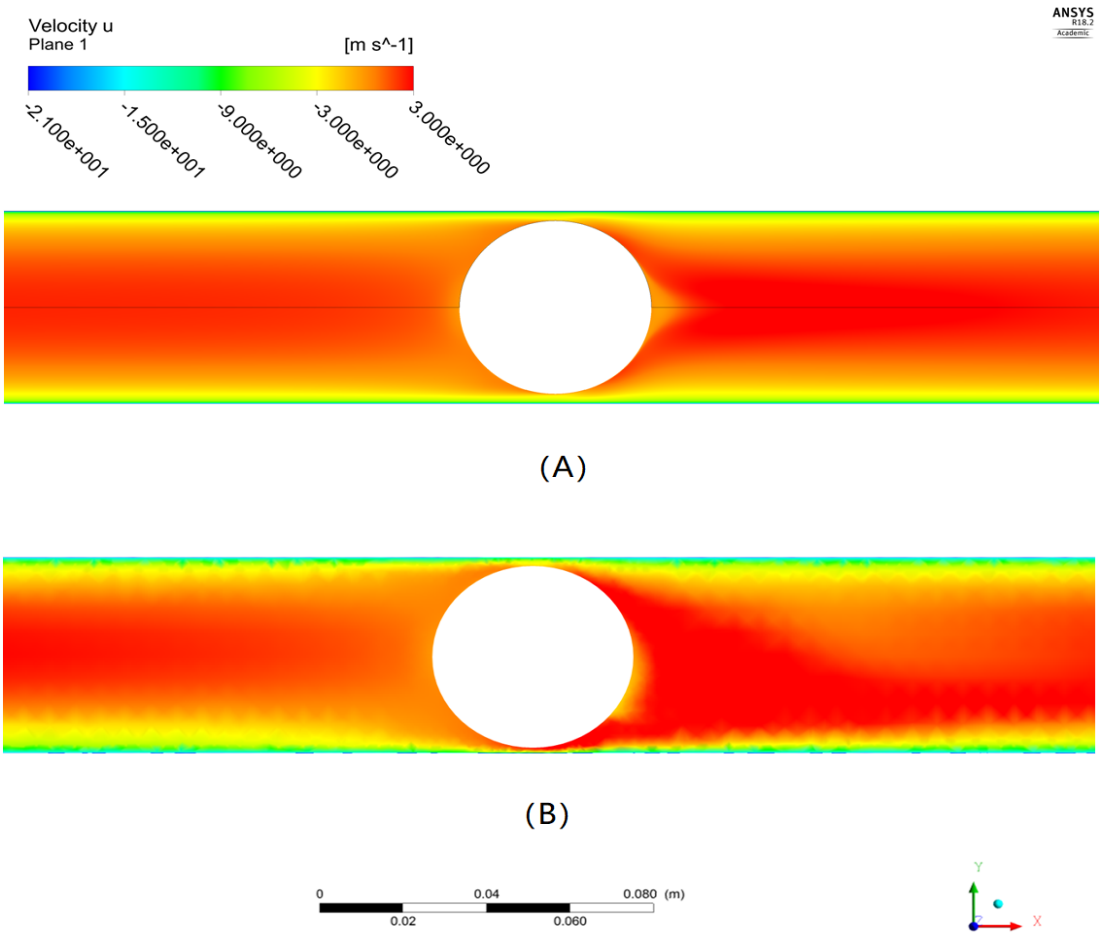

Figure 5.20: Axial velocity field contours around the pig at Re = 71197 from A) 2D simulation ; B) 3D simulation (xy plane)

the flow past an undersized ball pig which moves along the bottom of the pipe.

In contrast to the simulation results found when the pig is at the centre of the pipe, where the flow is in steady state when Re is smaller than 365, the flow is found to be unsteady at Re = 178 when the pig is moving along the bottom of the pipe. Figure 5.21 shows the drag coefficient profiles at this Reynolds number with the velocities which are used to interpolate the terminal pig velocity. When Re is 178, the average fluid velocity of the incoming flow is $0.05m/s$. It can be seen from the figure that when the pig velocity is $0.0555m/s$, the computed drag coefficient fluctuates around 0.206. When the pig velocity is increased to $0.056m/s$, the computed drag coefficient becomes negative and fluctuates around -0.22 after about 17 seconds. By using the same interpolation method which assumes a linear relationship between the pig velocity and the drag coefficient in this range and by using the average value of drag coefficient, the terminal pig velocity is found to be $0.0558m/s$. This is only slightly smaller than the value of $0.057m/s$ which was found when the pig is located at the centre of the pipe.

When Re is increased, the flow remains unsteady and the computed terminal pig velocities are always smaller than the ones obtained when the pig is at the centre of the pipe. For example, at Re = 2136, the pig velocity is $0.6m/s$ for the pig along the bottom and $0.68m/s$ for the pig in the centre. Figure 5.22 shows the computed drag coefficient profile when the pig is moving along the axis of the pipe with the velocity of $0.68m/s$. It can be seen that the computed drag coefficient fluctuates around zero.

When the pig is moving along the bottom, however, the simulation results show that the computed drag coefficient fluctuates around -0.51 after 15 seconds when the pig velocity is set to $0.68m/s$. Based on the finding from the force analysis that the drag coefficient decreases when the pig velocity

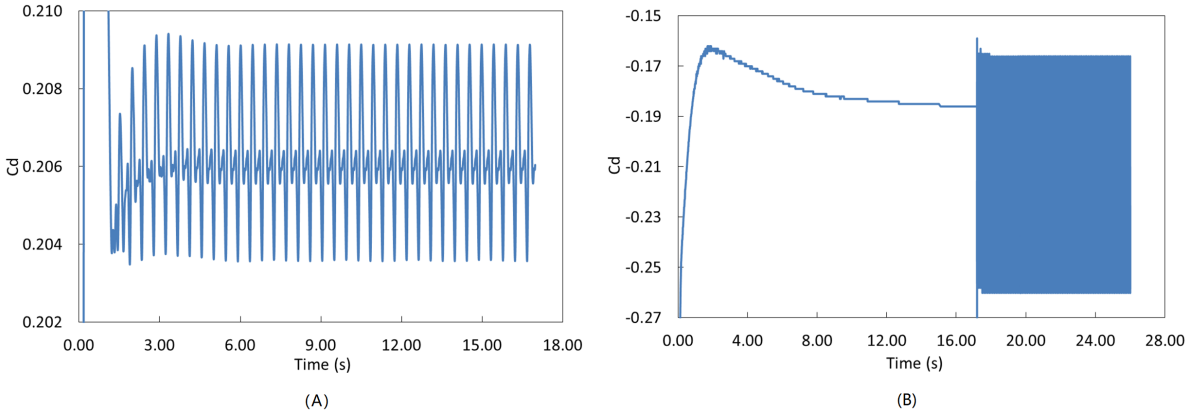

Figure 5.21: Drag coefficient profiles when Re = 178 with a pig velocity of: A) $0.0555m/s$; B) $0.056m/s$

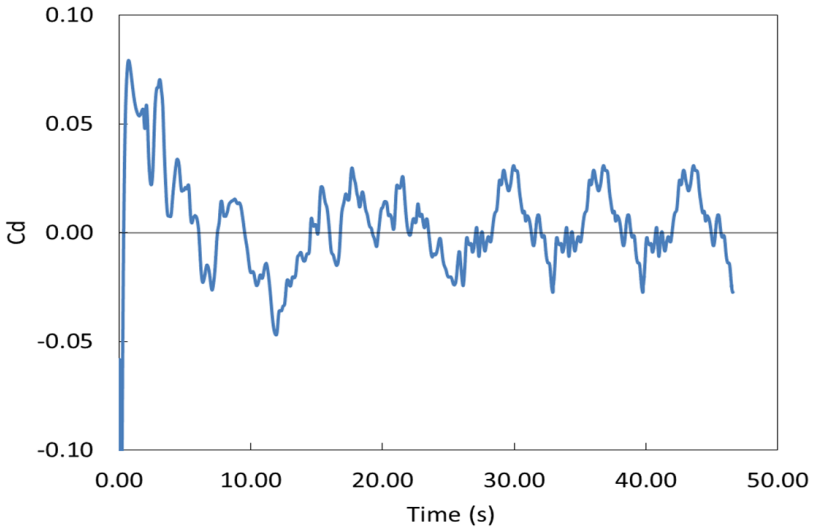

Figure 5.22: The drag coefficient profile when the pig moves along the axis of the pipe with a velocity of 0.68 m/s for Re = 2136

increases, this negative drag coefficient indicates that the terminal pig velocity is smaller than $0.68m/s$. Therefore, the pig velocity is decreased further to find the zero drag point. Figure 5.23 shows the computed drag coefficient profiles when the pig velocity is $0.67m/s$ and $0.66m/s$. It can be seen that the drag coefficient remains negative even when the pig velocity is decreased to $0.66m/s$. Figure 5.23 shows that the drag coefficient fluctuates around 2.4 after around 8 seconds. Linear interpolation between $0.66m/s$ and $0.67m/s$ gives a terminal pig velocity of $0.6685m/s$. Compared with the terminal pig velocity of $0.68m/s$, as found when the pig is at the centre of the pipe, moving the pig to the bottom of the pipe decreases the terminal pig velocity by 1.69% for Re is 2136.

The same procedure is used to find the terminal pig velocity when Re varies between 178 and 106796. Table 5.4 shows the pig terminal velocities and the decreased percentage compared with the computed results when the pig moves along the centre of the pipe at various values of the Reynolds number. It can be seen from the table that moving the pig from the centre to the bottom of the pipe leads to a decrease of the terminal pig velocity by 1.69% to 5.74% when Re is increased from 178 to 106796.

Figure 5.24 shows the comparison of the normalized pig terminal velocity profile against Re when the pig moves at the centre and along the bottom of the pipe. Apparently, by moving the pig from the centre to the bottom of the pipe, the value of $\frac{V_{pig}}{U}$ is decreased. The current results are obtained when the diameter ratio is 0.9. It is expected that similar results will be obtained for other pig diameters.

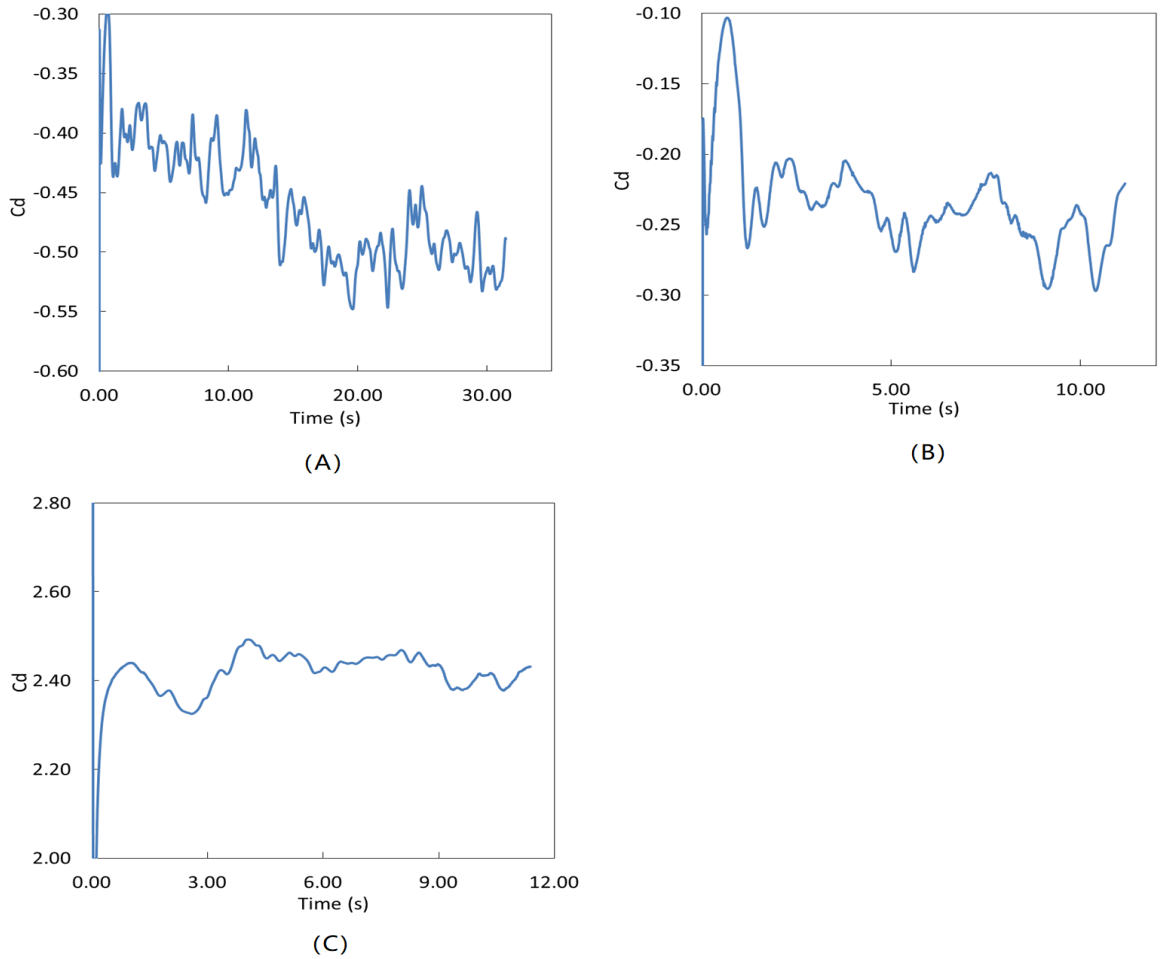

Figure 5.23: The drag coefficient profile when the pig moves along the bottom of pipe at Re = 2136 with various pig velocities: A) $0.68m/s$; B) $0.67m/s$; C) $0.66m/s$

Table 5.4: Pig terminal velocities when the pig moves along the bottom of the pipe and the percentage decrease in the pig terminal velocity compared with the results when the pig moves along the centre of the pipe

Re	Fluid velocity (m/s)	Terminal pig velocity (m/s)	Decrease percent $(\%)$
178	0.05	0.0558	2.11
356	0.1	0.1116	2.11
712	0.2	0.2235	2.06
2136	0.6	0.669	1.69
7120	2	2.15	4.02
10680	3	3.2	3.90
71197	20	20.8	5.74
106796	30	30.9	5.63

This effect should be included in the previously obtained expressions 5.1 and 5.2. However, since the current study only simulated the effect of the location change when the diameter ratio is 0.9, it is not possible to obtain the modified expressions. Therefore, simulations at other diameter ratios are

recommended to be carried in a future study.

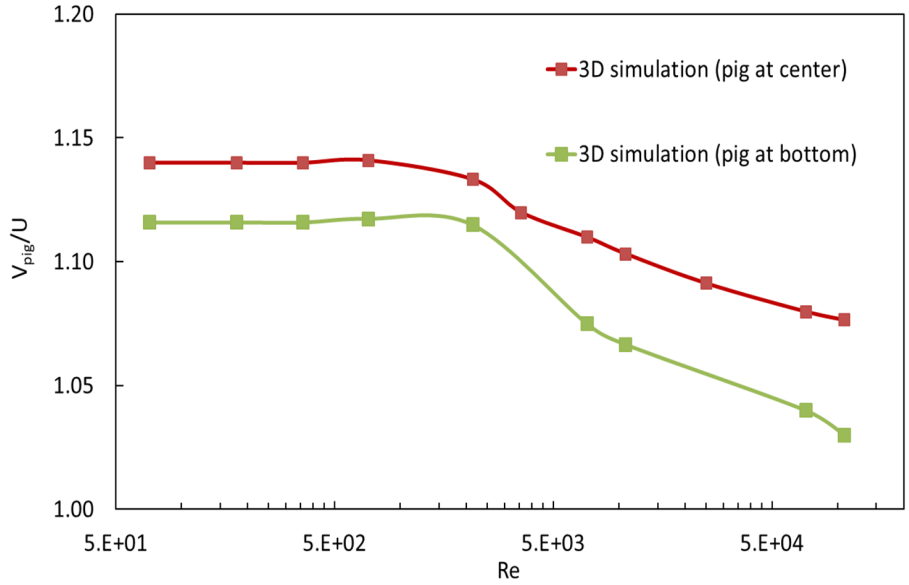

Figure 5.24: The drag coefficient profile when the pig moves along the bottom of the pipe at Re = 2136 with various pig velocities: A) $0.68m/s$; B) $0.67m/s$; C) $0.66m/s$

6

Possibilities to Simulate the Undersized Ball Pig under Multiphase Flow Conditions

The current study has only focused on the simulation the flow around an undersized ball pig under single-phase flow conditions. However, in actual field operations, often the undersized ball pig is used under multiphase flow conditions. This chapter will discuss some important aspects of numerical simulations for such multiphase flow conditions.

6.1. Simulation Domain

The considered multiphase flow system of liquid and gas in a horizontal pipe has stratified flow with the liquid phase flowing at the bottom of the pipe and the gas phase flowing at the top of the pipe. The motion of the liquid phase is driven by the drag force from the gas phase. This is because the gas phase moves with a velocity higher than the liquid phase. When an undersized ball pig is placed in the system, the motion of the undersized ball pig in this multiphase flow system will be balanced by the positive drag force from gas phase and the negative drag force from the liquid phase. This means that the terminal velocity of the undersized ball pig will be smaller than the gas phase and larger than the liquid phase.

Results from single-phase flow simulations show that the large diameter ratio is preferred in practical applications since it gives less leakage. This conclusion has been obtained from the single-phase flow simulations by considering the fluid velocity profile in the gap between the ball pig and the pipe wall. Since in a multiphase flow system, there is also only one phase by-passing the gap between the pig and pipe wall, this conclusion is also applicable to a multiphase flow system. Therefore, it is suggested to use large diameter ratios both in practical applications and in future simulations of the flow around an undersized ball pig in the multiphase flow system.

Transforming the frame of reference to the pig's frame of reference is again recommended for the multiphase flow simulation since generating a moving mesh poses too much complexity in the simulation. As has been stated above, the velocity of the undersized ball pig is lower than the velocity of the gas phase and higher than the one of the liquid phase. When the system is converted to the pig's frame of reference, the velocity of the gas phase is still positive but the velocity of the liquid phase will become negative. This means that the gas phase and the liquid phase will flow from two different sides of the pig. In Figure 6.1, the flow around the undersized ball pig in two different frames of reference are sketched. It can be seen that in the pipe's frame of reference, both the liquid and the gas phase are coming from the upstream direction of the pig and part of the fluid is accumulated behind the undersized ball pig, which is the slug generated by the ball pig. The liquid holdup gradually recovers

at the downstream side of the slug and the flow eventually exits the pipe at the outlet. However, if the flow is transformed to the pig's frame of reference, only the gas phase will be coming from the upstream direction of the pig since it has a positive velocity. The liquid phase will be approaching from the downstream side of the pig since its velocity in the pig's frame of reference is negative. For convenience, here the part at the left side of the pig is referred to as upstream of the pig. Apparently, it is not possible to prescribe the fully developed velocity profile at the inlet in this new frame of reference because there are two inlets at different sides of the pig. This means that the pipe length will need to be long enough to obtain the fully developed velocity profile. Therefore, the simulation domain of the multiphase flow simulation requires some further investigation. The pig diameter ratio of 0.9 is recommended since it has been used for the F-14 pipeline. The required pipe length upstream and downstream of the pipe can be determined by taking the entrance length from Equation 2.23 as a reference. In this multiphase flow system, the pipe lengths both upstream and downstream of the pig are important since the flows are approaching from both sides.

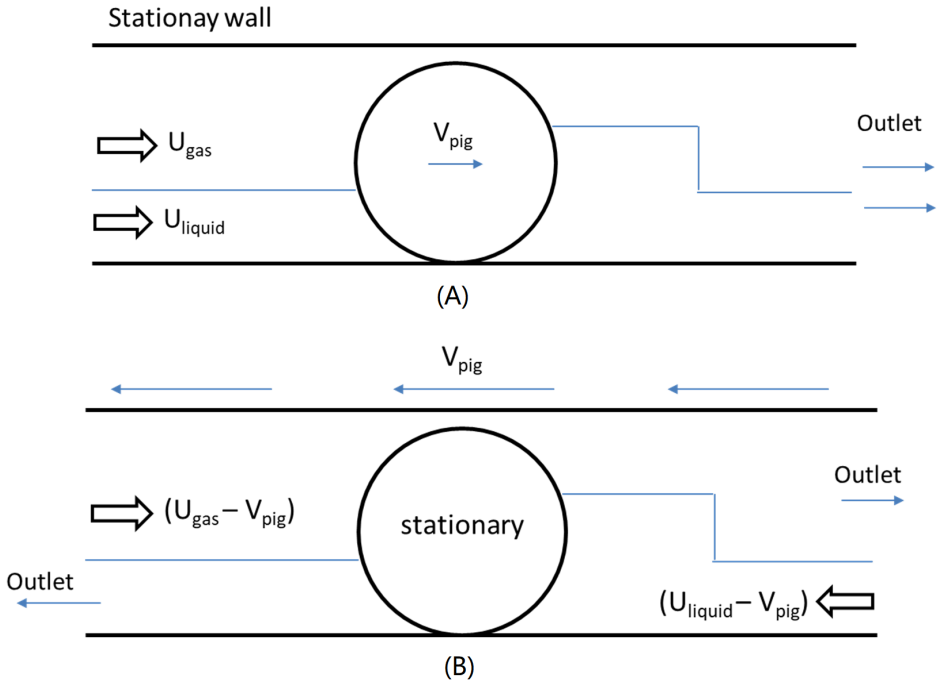

Figure 6.1: Sketch of the multiphase flow around an undersized ball pig in: A) the pipe's frame of reference; B) the pig's frame of reference

6.2. Boundary Condition and Numerical Setup

It can be seen from Figure 6.1 that the boundary conditions of this multiphase flow system are quite complex because there are two inlets and two outlets that need to be specified. In the pipe's frame of reference, the recovery level of the liquid holdup downstream of the slug is unknown. However, the boundary between the two inlets and the two outlets needs to be described in order to properly define the boundary conditions in the pig's frame of reference. Therefore, the assumption has to be made that the liquid holdup downstream of the slug eventually recovers to the same level as the incoming flow. With this assumption, the height of the boundaries (H) at the two faces will be the same and they can be calculated by using the liquid holdup (α):

$$\alpha\pi R^2 = R^2 arccos(\frac{R-H}{R}) - \frac{1}{2}(R-H)\sqrt{R^2-(R-H)^2} \tag{6.1}$$

The boundary conditions for the two inlet boundaries are obviously velocity inlet boundary conditions. But for the two outlets, the boundary conditions require some further investigation since the motion of the pipe wall makes the simulation difficult to converge. The single-phase simulations showed

that compared with the pressure outlet boundary condition, the outflow boundary condition helps to obtain converged results because it gives less restriction on the pressure field at the outlet. However, for the multiphase flow simulation, it is possible to define a backflow volume fraction for the pressure outlet boundary condition. It is therefore also possible to obtain well converged results with a proper definition of this parameter. A few preliminary multiphase simulations show that due to the moving wall and the two velocity inlets, convergence is most difficult for the continuity equation. Therefore, some extra analysis on the convergence of the continuity equation is suggested. Except for an appropriate selection of the boundary conditions, there are several other aspects which affect the convergence of the continuity equation. The accurate definition and selection of the corresponding numerical parameters could therefore help to improve the convergence. First, it is always suggested to decrease the under-relaxation factors and to check if a well converged solution can be obtained with these. Previous simulations, however, have showed that these factors have only a limited influence, but it is always good to check it first. Second, the convergence is largely dependent on the numerical discretization methods, especially on the pressure velocity coupling scheme. The use of the PISO scheme is strongly suggested since it includes additional loops which are meant to give a better convergence of the continuity and momentum equations.

Since the flow consists of two continuous fluids, the Euler-Euler approach should be used for the simulation of the multiphase flow system. Among the three methods in the Euler-Euler approach, the Volume of Fluid (VOF) model is suggested to be suitable for the simulation for stratified flow. Therefore, the VOF model is also suggested for the simulation of the multiphase flow around the undersized ball pig here. The VOF model assumes that the two phases are not interpenetrating with each other. For each phase in the system, the volume fraction of the phase in the computational cell is used to quantify the contribution of this phase. For any selected control volume, the sum of the volume fractions of all the phases should be 1. The value of the volume fraction of any phase should be in the range from 0 to 1. For any n^{th} phase involved in the system, the volume fraction equation is:

$$\frac{\partial \alpha_n}{\partial t} + u_i \cdot \nabla \alpha_n = \frac{S_{\alpha_n}}{\rho_n} \tag{6.2}$$

where α_n is the volume fraction of n^{th} phase and S is the source term, which is zero in the current case. For the simulation of two phase flow, Ansys Fluent only solves the volume fraction equation of the second phase and the one of the primary phase can be calculated from: $1 - \alpha_2$.

Compared with the single-phase flow simulation, a multiphase flow simulation is more complex and time consuming. This chapter gives only a brief discussion of the simulation of the multiphase flow around an undersized ball pig in the pipe. Since there are multiple reasons which could cause divergence problem, it is suggested to start the multiphase flow simulations with simple cases. For example, it is suggested to set the velocity of the pig and the pipe wall to zero and to simulate the multiphase flow around the undersized ball pig first. In this scenario, the simulation will not be affected by the moving wall and by the countercurrent flow from two sides of the pig. The correct simulation will only rely on a reasonable mesh generation and on the appropriate selection of numerical methods. Then the moving ball boundary condition can be added to find the most appropriate boundary condition for the outlet. Once a converged solution has been obtained with a moving wall boundary condition, the countercurrent flow can be added by using the the two inlets as shown in Figure 6.1.

7

Conclusions and Recommendations

Due to the successful application of an undersized ball pig prior to the by-pass pig in actual operations (the F14 pipeline in Sarawak), it is of great interest to investigate the detailed flow around an undersized ball pig in a horizontal pipe. This is meant to better understand the use of ball pigging in pipelines that transport single-phase or multiphase fluids. Ansys Fluent version 18.2 was used to study the flow around an undersized ball pig in a horizontal pipe numerically. This chapter provides the conclusions and recommendations for future work based on the current numerical study.

7.1. Conclusions

The simulation study started with model validation. For the flow around an undersized ball pig in a pipe, the successful simulation of the flow largely depends on the accurate prediction of the drag coefficient since it determines the zero drag point; note that the latter determines the velocity with which the ball pig is moving in the pipeline. Therefore, the experimental benchmark data from Schlichting [15] for the drag coefficient curve for the flow past a sphere in an open area was used to find the most appropriate numerical model. From the comparison of the simulation results with experimental data, the following conclusions can be obtained:

- The flow past a sphere is in steady state and axisymmetric when the Reynolds number is sufficiently low. The 2D laminar approach in Ansys Fluent is capable to accurately capture the flow and drag coefficient when Re < 300;
- 3D simulations show that the flow is unsteady and asymmetric when 300 < Re < 50000. However, by using the SST $k-\omega$ turbulence model with low-Reynolds number correlation, the computed drag coefficients from the 2D steady state simulation agree very well with experimental data in this range;
- Two-equation turbulence models are not capable of capturing the boundary layer transition and hence they cannot provide appropriate results when Re > 50000.

After finding the appropriate numerical models, these are used to study the (single-phase) flow around an undersized ball pig in a pipe. Since the numerical models are selected based on 2D simulations and there is a strong preference to do the simulations in 2D (to keep the computational time manageable), the undersized ball pig is manually moved to the centre of the pipe. Base on the 2D simulation results, the following conclusions can be drawn:

- The ball pig experiences a positive pressure force and a negative viscous shear force at its equilibrium state;
- The normalized pig terminal velocity profile at a given diameter ratio decreases when Re increases and experiences three stages when Re increases from 36 to 5E5. When the flow is in a small Re range, the viscous shear force plays the major role in determining the equilibrium motion of the pig. When Re increases, the effect of the inertia force starts to play a role and the influence of

the inertia force becomes more and more important when the Reynolds number increases. In this Reynolds number range, where the viscous shear force and the inertia force both affect the motion of pig, the normalized pig terminal velocity profile decreases rapidly when Re increases. When the Reynolds number is further increased, the motion of the pig is completely dominated by the inertia force and the normalized terminal velocity of the pig remains again in a stable range. The corresponding Reynolds number range in the three stages varies when the diameter ratio changes. But the overall change of the profile and the characteristics in the three regions is the same;

- The normalized pig terminal velocity decreases when the diameter ratio increases at a given Re. The normalized pig terminal velocity in the range Re < 300 is constant at a fixed diameter ratio. It is therefore only a function of the diameter ratio in this Re range and can be described by a second-order order polynomial with Equation 5.1. When Re > 10000, the normalized pig terminal velocity also stays in a very stable range for each diameter ratio. The profile of the normalized pig terminal velocity against the diameter ratio also lies on a second order polynomial at various Re values and can be expressed by Equation 5.2;

- The flow in the gap between the pig and the pipe at a large diameter ratio (0.9) has been proved to be locally behaving as a combined Couette and Poiseuille flow since the fluid velocity profile in the gap has the same shape as the one obtained from two parallel plates, with one plate moving and with a nonzero pressure gradient.

After having studied the details of the flow around an undersized ball pig which moves along the axis of the pipe, the pig with a diameter ratio of 0.9 has been moved to the bottom of the pipe and the influence of this position change is studied. When the pig is moved to the bottom of the pipe, it is not possible to do a 2D simulation anymore. Therefore, a 3D simulation needs to be performed. First a 3D simulation has been made for the flow around an undersized ball pig which moves along the axis of the pipe and the results are compared with the ones obtained from the 2D simulation. After this, the pig is moved to the bottom of the pipe and again a 3D simulation is performed. Based on the 3D simulations, the following conclusions are obtained:

- The flow past an undersized ball pig moving along the axis of the pipe is proven to be steady state and axisymmetric when Re < 365 since the 3D simulations produce the same results as found from the 2D approach in this range;

- The flow becomes unsteady and asymmetric when Re > 365 and the computed terminal pig velocities obtained from the 3D simulations are slightly higher than the ones obtained from the 2D simulations when Re varies from 4000 to 106796. The flow field comparison shows that a difference between the 2D and 3D simulations exists because the flow is essentially asymmetric. Therefore the 2D simulation apparently is not capable of capturing this asymmetry. This leads to a less accurate prediction for the pressure force exerted on the pig and thus gives a less accurate prediction of the terminal pig velocity. But it is worth noting that the difference between the 2D and 3D results is very small;

- The flow is found to be unsteady when the pig is moved to the bottom of the pipe for the entire studied Reynolds number range;

- Compared with the case when the pig moves along the axis of the pipe, the terminal velocity of the pig decreases when the pig moves along the bottom of the pipe.

7.2. Recommendations

To find the major factors which affect the motion of the ball pig, this study started from single-phase flow. The following recommendations are suggested for further research with simulation for ball pigging in single-phase or multiphase flows:

- It was found that the terminal velocity of the pig decreases when the pig is changed from the centre to the bottom of the pipe with a diameter ratio of 0.9. The same effects are expected for the flow past an undersized ball pig with other diameter ratios. With all the simulation results,

modified expressions of Equation 5.1 and 5.2 can be obtained and the modified equations will show a full picture of the relationship for all parameters involved in the problem for the single-phase flow system. Simulations at other diameter ratios were not yet performed and the modified expressions were thus not yet obtained. It is therefore suggested to perform more simulations for the flow around an undersized ball pig which moves along the bottom of the pipe at other diameter ratios and to obtain the modified expressions.

- Since the undersized ball pig is more often used for multiphase flow pipeline system, it is therefore recommended to further study the multiphase flow past an undersized ball pig in a pipe. In Chapter 6, detailed recommendations for such multiphase flow simulations are given.
- The flow loop in the lab of the Process & Energy Department is well established and ready to do ball pig experiments. It is recommended to do some experiments for the flow past an undersized ball pig under both single-phase and multiphase conditions and to compare the experimental results with the numerical results.
- Once correlations have been found for the pig movement (with their dependence on the diameter ratio and on the Reynold number for single-phase flow, and liquid and gas Reynolds numbers for two-phase flow), as based on the CFD simulations, these correlations should be implemented in the one-dimensional pipe flow models that are used in the industry. Thereafter ball pig simulations can be performed with the one-dimensional models, and the reliability of the results should be verified.

A

Appendix

A.1. Drag Coefficient Profiles Used for the Linear Interpolation in Table 5.3

In Chapter 5 when the simulation was moved to 3D, the flow became unsteady and the terminal velocity of the pig was found by linear interpolation of the average value of two drag coefficient profiles in which one fluctuates above zero and the other one fluctuates below zero. This section will show the drag coefficient profiles which were not described in Chapter 5 but which were used to do the interpolation for various Reynolds numbers as shown in Table 5.3.

A.1.1. Re = 10680

When the Reynolds number is 10680, the bulk fluid velocity in the pipe is $3m/s$ and the drag coefficient profiles at a pig velocity of $3.3m/s$ and $3.4m/s$ are used to find the terminal pig velocity. The corresponding drag coefficient profiles obtained at these two pig velocities are shown in Figure A.1.

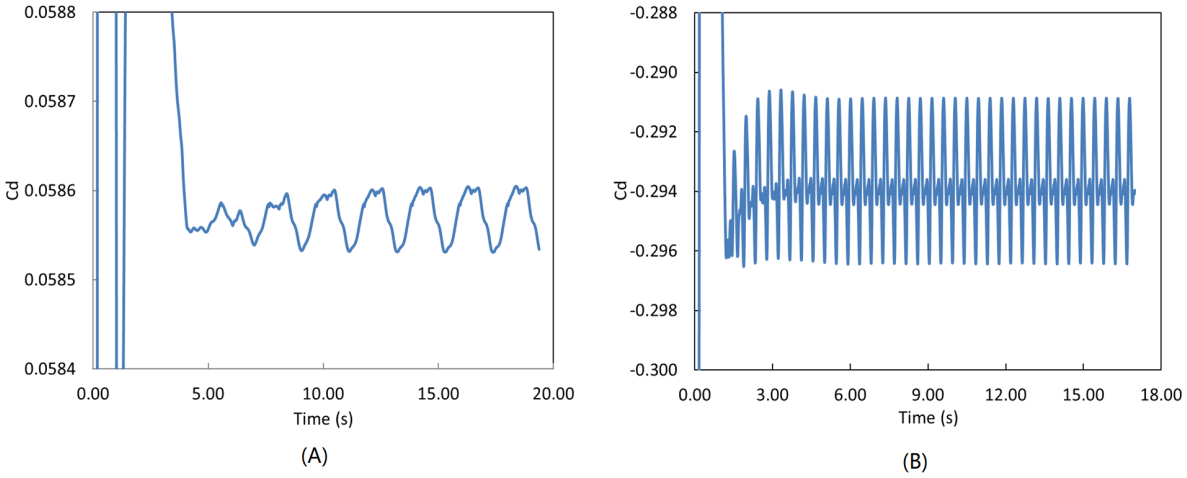

Figure A.1: Profiles of the computed drag coefficient at Re = 10680 when the pig velocity is: A) $3.3m/s$; B) $3.4m/s$

A.1.2. Re = 71197

When the Reynolds number is 71197, the bulk velocity of the fluid in the pipe is $20m/s$ and the drag coefficient profiles at a pig velocity of $21m/s$ and $22m/s$ are used to find the terminal pig velocity. The corresponding drag coefficient profiles obtained at these two pig velocities are shown in Figure A.2.

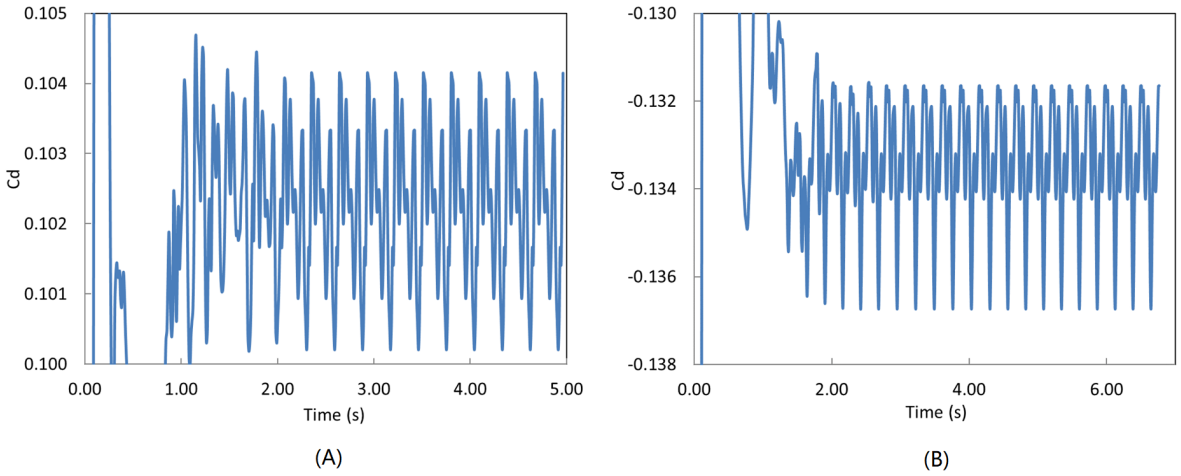

Figure A.2: Profiles of the computed drag coefficient at Re = 71197 when the pig velocity is: A) $21m/s$; B) $22m/s$

A.1.3. Re = 106796

When the Reynolds number is 106796, the bulk velocity of the fluid in the pipe is $30m/s$ and the drag coefficient profiles at pig velocity of $32m/s$ and $33m/s$ are used to find the terminal pig velocity. The corresponding drag coefficient profiles obtained at these two pig velocities are shown in Figure A.3.

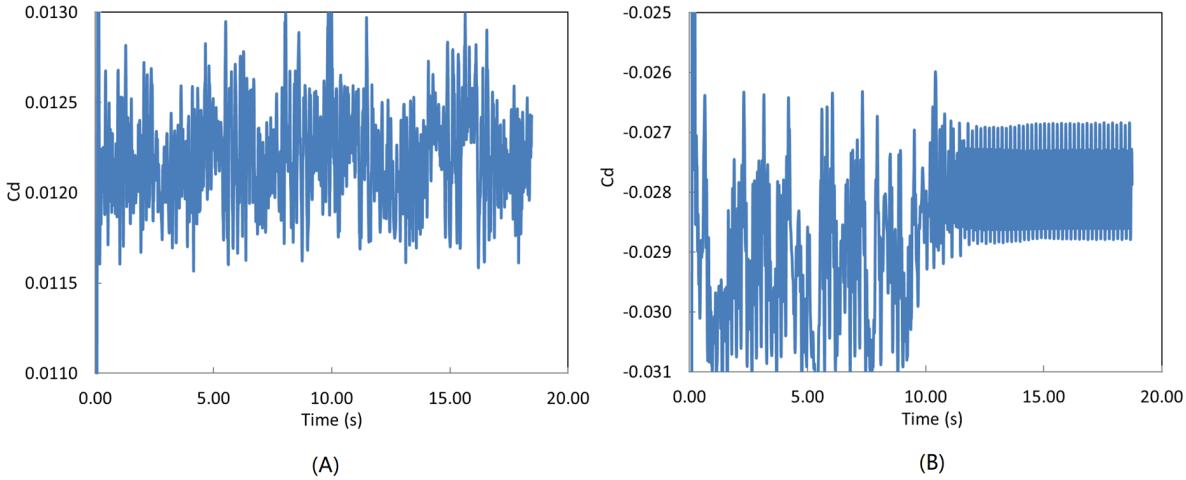

Figure A.3: Profiles of the computed drag coefficient at Re = 106796 when the pig velocity is: A) $32m/s$; B) $33m/s$

Bibliography

[1] A. Singh and R. A. W. M. Henkes, *CFD modelling of the flow around a by-pass pig,* Shell Global Solutions, SR.12.11283 (2012).

[2] A. Entaban, A. Ismail, M. Jambari, P. Ting, K. M. Amin, C. C. Ping, S. Zou, and G. van Spronsen, *By-pass pigging - a 'simple' technology with significant business impact,* in *IPTC 2013: International Petroleum Technology Conference* (International Petroleum Technology Conference, 2013) pp. 1–6.

[3] H. S. Lee, D. Agustiawan, K. I. Jati, M. Aulia, S. A. Thomas, S. P. Appleyard, *et al.*, *Bypass pigging operation experience and flow assurance study,* in *Offshore Technology Conference* (Offshore Technology Conference, 2012) pp. 1–10.

[4] P. Bhattacharjee, *Modelling undersized ball pigs using dynamic simulations,* Shell Global Solutions (Internal report, 2017) .

[5] A. E. McDonald and O. Baker, *A method of calculating multiphase flow in pipe lines using rubber spheres to control liquid holdup,* in *Drilling and Production Practice* (American Petroleum Institute, 1964) pp. 56–68.

[6] K. Kohda, Y. Suzukawa, and H. Furukawa, *Analysis of transient gas-liquid two-phase flow in pipelines,* Journal of energy resources technology **110**, 93 (1988).

[7] A. O. Nieckele, A. M. B. Braga, and L. F. A. Azevedo, *Transient pig motion through gas and liquid pipelines,* Journal of Energy Resources Technology **123**, 260 (2001).

[8] F. Esmaeilzadeh, D. Mowla, and M. Asemani, *Mathematical modeling and simulation of pigging operation in gas and liquid pipelines,* Journal of Petroleum Science and Engineering **69**, 100 (2009).

[9] B. Jamshidi and M. Sarkari, *Simulation of pigging dynamics in gas-liquid two-phase flow pipelines,* Journal of Natural Gas Science and Engineering **32**, 407 (2016).

[10] S. Barua, *An experimental verification and modification of the McDonald-Baker pigging model for horizontal flow*, Ph.D. thesis, University of Tulsa (1982).

[11] K. Minami, O. Shoham, *et al.*, *Pigging dynamics in two-phase flow pipelines: experiment and modeling,* SPE production & Facilities **10**, 225 (1995).

[12] *OLGA dynamic multophase flow simulator user manual*, Schlumberger (2016).

[13] B. Richa, *Undersized ball pig modelling,* Shell Global Solutions, SR.12.11283 (2016).

[14] A. C. Yunus and J. M. Cimbala, *Fluid mechanics fundamentals and applications,* International Edition, McGraw Hill Publication **185201** (2006).

[15] H. Schlichting, *Boundary layer theory,* McGarw-Hill Book Company , 135 (1979).

[16] K, S. Nidhul, M. Sunil, and Benphil, *Effect of domain size and grid spacing on flow past a circular cyliner at low reynolds number,* International journal of engineering reseach and technology **3**, 1365 (2014).

[17] D. A. Jones and D. B. Clarke, *Simulation of flow past a sphere using the fluent code*, Tech. Rep. (Defense Science and Technology Organization Victoria (Australia) Maritime Platforms Div, 2008).

[18] T. Maxworthy, *Experiments on the flow around a sphere at high reynolds numbers,* Journal of Applied Mechanics **36**, 598 (1969).

[19] S. Kraheberger, S. Hoyas, and M. Oberlack, *DNS of a turbulent couette flow at constant wall transpiration up to Re = 1000,* Journal of Fluid Mechanics **835**, 421 (2018).